Growth Control and Manipulation of Morphology, Crystallinity, and Physical Properties of Tin (IV) Oxide Nanostructures: Granular Nanocrystalline Films and One-Dimensional Nanostructures

by

Samad Bazargan

A thesis
presented to the University of Waterloo
in fulfillment of the
thesis requirement for the degree of
Doctor of Philosophy
in
Chemistry

Waterloo, Ontario, Canada, 2011

AUTHOR'S DECLARATION

I hereby declare that I am the sole author of this thesis. This is a true copy of the thesis, including any required final revisions, as accepted by my examiners.

I understand that my thesis may be made electronically available to the public.

Abstract

A variety of nanostructures of tin (IV) oxide (TO) are synthesized using two fabrication methods: a solution spin-coating method followed by post-annealing in an oxygen flow and a newly developed catalyst-assisted pulsed laser deposition (PLD) technique. The spin-coating method is used to fabricate granular TO films with monodisperse, stable, ultra-small nanocrystallites (4-5 nm in size), the size of which is found to increase exponentially with post-anneal at temperature (T_{Anneal}) above 500°C. These nanocrystalline films are conductive and highly transparent, and their bandgaps show broadening due to a high carrier concentration. Their resistivity behavior as a function of temperature in the 50-280 K range can be explained by a two-medium transport model, i.e. transport through the crystalline grains and across the grain boundaries, and through the charge-depletion layer, where a potential barrier is found for transport across the grain boundaries. Electronic transport in these films follows a 3D-variable range hopping model, which reveals an increase in the localization length of carriers with increasing the T_{Anneal} above the onset of exponential growth at T_{Anneal}= 500°C. By homogenously doping Eu^{3+} in these nanocrystalline films up to a high doping level of ~ 8%, optical luminescence and magnetic orderings can be introduced into these nanocrystalline TO films. Both characteristic Eu^{3+} emission and defect-related TO emissions are observed in the otherwise transparent TO films upon UV-excitation. In spite of the non-magnetic nature of Eu^{3+} ions, magnetic orderings appear in the highly doped TO films below 50 K upon the emergence of $Eu_2Sn_2O_7$ phase. In the second part of the present work, we employ a layer of gold nanoislands with controlled sizes (10-50 nm) as catalysts for pulsed laser deposition of TO nanostructures. Highly crystalline TO nanobricks, cuboid nanoparticles, nanowires and nanobelts are obtained for the first time through vapour-solid or vapour-liquid-solid (VLS) mechanism. Of particular interest are the micron long one-dimensional (1D) nanowires and nanobelts, with the smallest square and rectangular cross-sections, respectively, ever reported. These single-crystalline nanostructures are obtained at relatively low temperatures of 600°C, for nanowires, and 500°C, for nanobelts, and their cross-sectional sizes can be easily controlled by the size of the gold nanoislands. The nanobelts are found to grow along the [100] and [101] axes, while the nanowires appear to grow along the [100] axis. The growth evolution of the nanobelts are also investigated in detail revealing their VLS growth mode and their single-crystalline structure throughout the growth, which opens the prospect of controlling their growth axis and consequently their side-surface planes by pinning the base to the substrate at the desired crystalline orientation. Together, the two fabrication methods developed in the present work offer facile

approaches to growing two scientifically and technologically important classes of TO nanostructures, i.e., nanocrystalline film and 1D nanostructures. Thorough characterization of the resulted nanostructured materials using advanced microscopic, spectroscopic and other techniques, including Helium Ion Microscopy, has been provided. Modification of structure, morphology and physical properties of these functional nanostructured materials are also illustrated by controlling the growth parameters and by (Eu-)doping, which pave the way for introducing new properties for applications in chemical sensing, (opto)electronics and displays.

Acknowledgements

I would like to express my deepest gratitude to my PhD supervisor Prof. Kam Tong Leung for his invaluable support throughout this project. He provided me with the opportunity to learn and use all the key instruments required for this work. His advice and guidance along with his positive, kind, and friendly personality have always been motivating and made this work possible.

I would also like to thank my advisory committee members Dr. Eric Prouzet, Dr. Hany Aziz, and Dr. Dmitriy Sodatov for their insightful comments, suggestions and valuable feedback on the work.

I had the pleasure of working in WATLab, where not only did I have the opportunity to learn a lot and discuss different topics and ideas, but also to make friends whom I will never forget. I would like to thank all WATLab members especially Dr. Nina Heinig, Dr. Helia Jalili, Avisek Chatterjee, Dr. Liyan Zhao, Dr. Debabrata Pradhan, Dr. Maryam Ebrahimi, Nafiseh Moghimi, Dr. Lei Zhang, Farheen Kinoo, and Fernando Rios.

I am also very grateful to my dear friends Hamid Molavian Jazi, Azad Qazi Zade, Sattar Taheri Araghi and Farinaz Babaeipour, Bahador Biglari and Noushin Shiran, Iman Marvian Mashhad, Amir Jafari Salim, Kanwartej Singh Sra and Puneet Dhaliwal, and many others who have made my time in Waterloo memorable. I would also like to express my appreciation of the love, encouragement and support I have received in the hardest moments from my girlfriend Caitlin McQuaite and her loving parents Kim and Deborah.

And last but not least, I express my heartfelt gratitude to my parents Ali and Motahareh, my brothers Akbar, Morteza, and Mahdi, and their families for their love has always been with me and has given me the energy to reach for otherwise impossible goals of my life despite the long distance between us. I am proud of you and you have a big share in what I have achieved.

Dedication

To my supportive loving parents *Ali* and *Motahareh*, I dedicate this thesis.

Table of Contents

List of Figures

List of Tables

Chapter 1
Introduction

1.1 Transparent Conducting Oxides

Oxides are an important class of materials exhibiting numerous interesting chemical and physical properties in their pure and doped forms. Obtaining a perfect oxygen stoichiometry in the bulk and surface of the oxides is often found to be challenging. This oxygen imbalance is shown to be the origin of some of the most fascinating phenomena observed in the oxides, including the observed conductivity in transparent conducting oxides (TCO),[1] and the metal-to insulator transition in high T_c superconducting perovskites.[2] In addition to the variation in oxygen content, extrinsic ion doping in the oxides is also essential for further enhancement or development of their properties. Among the oxide materials that show a wide range of electrical properties including insulators, semiconductors, and superconductors, the wide-band gap semiconductors are of special scientific and technological interests due to the coexistence of the optical transparency and electrical conductivity in these materials. These oxides show a high optical transparency in the visible range because of their wide energy band-gaps. On the other hand, the presence of shallow carrier donor levels in the vicinity of their conduction band allows for generation of carriers that contribute to conductivity of these oxides. These oxides are often found to be n-type, and resistivities as low as 10^{-4} Ω·cm are achievable by appropriate doping.[3] The origin of this n-type carriers are shown through density functional calculations to be the intrinsic cation interstitials and oxygen vacancies,[1] and hydrogen doping.[4] A variety of binary and ternary TCO compounds, including the most commonly used SnO_2, ZnO, In_2O_3, and CdO oxides, have been reported.[3,5] These materials are widely used in their doped form in optoelectronic devices, where a transparent electrode is required as in flat-panel displays, solar cells, and organic light emitting diodes. Transparent electronics is another important research area, where doped TCO's are required in both n-type and p-type forms as active semiconductor layers. In spite of the successful combination of n-type TCO and p-type organic layers for fabricating transparent transistors,[6] many challenges remain in the fabrication of all-oxide transparent transistors due to the lack of appropriate p-type TCO compounds.[3] Moreover, most of the TCO materials are found to exhibit catalytic properties for oxidation reactions,[7] e.g. CO and NO oxidation, and gas sensing properties towards various gases, including CO[8] and H_2.[9] The catalysis and sensing mechanisms are based on the reaction of the surface oxygen of the oxides, where in the former leads to oxidation of the molecule and in the latter causes a change in the carrier concentration affecting the surface

conductivity and thereby inducing an electrical signal. The fabrication of different nanostructures of these TCO materials has also received much recent attention, partly because of the natural increase in the surface-to-volume ratio in the nanoscale, which is of great importance for catalytic and sensing applications, and also because of the new possibilities emerging in the manipulation of their properties in the nanoscale.

As one of the most important functional oxides among the TCO materials, tin oxide is the focus of the present study. In the following sections, the significance of this oxide among other TCO's and its basic properties in the bulk form will be briefly described. This will be followed by overview of the synthesis, properties, and applications of various nanostructures of SnO_2. The last section will discuss the motivation for the present study and the structure of the thesis.

1.2 Compounds of Tin Oxide

Tin has two main oxides in the normal conditions: stannic oxide, SnO_2, and stannous oxide, SnO, where tin shows 4+ and 2+ oxidation states, respectively. The phase diagram of Sn-O shows that stannous oxide is not thermodynamically stable, and upon heating to 450°C, it undergoes a disproportionation reaction to final products of Sn and SnO_2 in an inert atmosphere.[7,10] Stannous oxide has a tetragonal litharge crystal structure different than the tetragonal rutile structure of stannic oxide. Stannic oxide is the most stable form of tin oxide with a band-gap of 3.6 eV[11] and is a transparent conducting oxide. The source of the observed conductivity is related to the non-stoichiometry of the oxide. Moreover, it is shown experimentally that heat treatment in different gas environment leads to considerable variations in the resistivity of this oxide,[12,13] confirming the effect of stoichiometry of the lattice on its conductivity. Density functional calculations have suggested the source of intrinsic conductivity in SnO_2 to be shallow donor levels caused by oxygen deficiency, and more importantly Sn interstitials[1] or hydrogen doping,[4] which also account for their dependence on the annealing environment. To obtain a higher conductivity in the SnO_2 films, Sb and F dopants are commonly used, leading to resistivity values of 2×10^{-4} Ω·cm, comparable to those of the highly conductive indium-tin-oxide and doped ZnO films (Table 1.1).[3,5,7] As can be seen in Table 1.1, SnO_2 is among the most thermally stable and chemically and mechanically durable TCO's, and it also has the highest work function, lowest plasma frequency, least toxicity, and the lowest cost, which make it one of the most important TCO materials for various applications involving transparent conducting oxides.

Among all the oxides with gas-sensing properties, SnO_2 is the most widely used material due to its high sensitivity towards adsorbed gases. Surface conductivity of SnO_2 depends on the coverage of adsorbed charged oxygen species on the surface of the oxide, which consequently leads to a change in the depletion layer created on the surface.[7] It has also been shown that by using appropriate dopants, sensitivity towards gases can be increased significantly.[8] Furthermore, incorporation of appropriate dopants can also provide selective sensing towards specific gases,[14] e.g. Cu for sensing H_2S.[15] Doping SnO_2 has also shown promises in inducing other physical properties in SnO_2, including optical fluorescence,[16] and ferromagnetism with a high Curie temperature.[17] These are just some examples of the rich properties of pristine and doped stannic oxides, which make them an important functional material from both scientific and technological perspectives.

Table 1-1 Choice of Transparent Conductors.[5*]

Property	**Material**
Highest Transparency	ZnO:F, Cd_2SnO_4
Highest Conductivity	In_2O_3:Sn
Lowest plasma frequency	SnO_2:F, ZnO:F
Highest plasma frequency	Ag, TiN, In_2O_3:Sn
Highest work function, best contact to *p*-Si	SnO_2:F, $ZnSnO_3$
Lowest work function, best contact to *n*-Si	ZnO:F
Best thermal stability	SnO_2:F, TiN, Cd_2SnO_4
Best mechanical durability	TiN, SnO_2:F
Best chemical durability	SnO_2:F
Easiest to etch	ZnO:F, TiN
Best resistance to H plasmas	ZnO:F
Lowest deposition temperature	In_2O_3:Sn, ZnO:B, Ag
Least toxic	ZnO:F, SnO_2:F
Lowest cost	SnO_2:F

[*] Reproduced with permission [Roy G. Gordon (2000). Criteria for Choosing Transparent Conductors. MRS Bulletin, 25, pp 52-57 doi:10.1557/mrs2000.151]

1.3 Nanostructures of SnO_2

Fabricating nanostructures of SnO_2, TO for short, has attracted a lot of attention, and various fabrication methods have been developed to synthesize a variety of its nanostructures. These methods include sputtering,[15,18] sol-gel[9,19-21] and other solution-based methods,[22-24] electrodeposition,[25] thermal evaporation[26-28] and other vapor transport deposition techniques,[29] and they have been used to produce nanostructured films, nanoparticles, nanorods, nanobelts, and nanoribbons of TO. Synthesis of TO nanostructures is of great interest for two main reasons: First, some of the known properties of TO are found to change drastically from those in the bulk form upon formation of structures at the nanoscale. As a result of the decrease in size, the surface-to-volume ratio increases considerably, which in turn greatly affects the surface-related properties of TO. These properties include the catalytic activity and gas-sensing properties, and they have been shown to improve considerably[14,30] for nanoparticle assembly and nanostructured films of TO. As an example, sensitivity of different TO gas sensors, as one of the well-known applications of TO, with respect to the film thickness, crystallite size, and operating temperature for sensing H_2 gas are shown in Figure 1.1, which is a compilation of data from various reports with different synthesis methods.[9] It is clear that having control on the crystallite size, morphology, and thickness of the nanocrystalline TO films can lead to a great improvement in the gas sensing properties of TO. Second, new properties are found to emerge due to the specific characteristics introduced in the new nanostructures of TO. The one-dimensional nanostructures of TO have single-crystalline structures with faceted, low-index side surfaces. These nanostructures are observed to have excellent characteristics as components in field-effect transistors[31] and other fabricated devices, which exhibit conductivity change upon UV illumination. It has also been shown that these transistors can be used in combination with the sensing property of TO for measuring pH.[32] Furthermore, nanoribbons of TO have been used as waveguides for transmitting photons in the visible range, the flexibility of which allows for their manipulation in building photonic circuits and making optical linkage between the nanoribbons.[33]

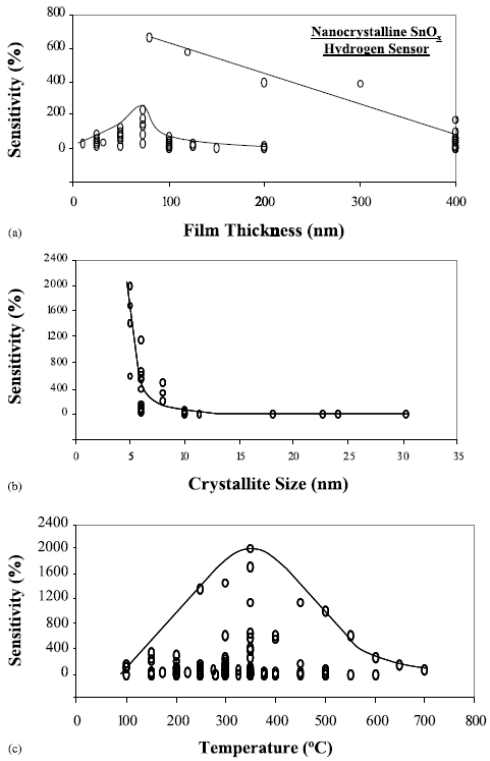

Figure 1.1 Graphs of H_2 gas sensitivity as a function of (a) nanocrystalline SnO_2 semiconductor thin film thickness, (b) SnO_2 nanocrystallite size, and (c) operating temperature.[34†]

1.3.1 Nanocrystalline films

Motivated by the observed improvements in the various properties of TO including catalytic and gas sensing, a great deal of attention has been directed towards synthesis of TO nanostructures. Various deposition method including sputtering[35] and spray pyrolysis[36] have been used for synthesizing nanostructured films. However, among all these methods, solution phase and sol-gel are the commonly used methods for this purpose. These methods generally involve formation of alkoxide solutions by dissolving various Sn salts in alcohol followed by controlled hydrolysis resulting in the gel formation, where some modifications in different steps of these processes are found for different reports. The resultant gel is then coated onto a substrate or transferred into a template[37] and then the dried gel is annealed in air in order to reach the final oxide product. Depending on the method of

† Reprinted from Sensors and Actuators B, 96, S Shukla, S. Patil, S.C. Kuiry, Z. Rahman, T. Du, L. Ludwig, C. Parish, and S. Seal, Synthesis and characterization of sol–gel derived nanocrystalline tin oxide thin film as hydrogen sensor, 343-353, Copyright (2003), with permission from Elsevier.

coating the gel on the substrate, various methods including spin-coating[21] and sol-gel dip coating,[38-40] are formed, while precipitation of the gel followed by drying has also been reported for producing TO nanoparticles.[19] The TO films obtained using these methods have nanocrystalline grain sizes that can be controlled by the annealing temperature. Morphology and thickness of the films can also be controlled with suitable parameters including the gel concentration and the number of coating cycles using the aforementioned methods. Further modification of the surface hydroxyl group before annealing the gel has also been shown to help control the size of the annealed crystallite size in the 2-5 nm size range by pinning the grain boundaries.[19] A typical example of nanocrystalline TO grains produced using a sol-gel method is shown in Figure 1.2, where hexamethyl-disilazane (HMDS), i.e. $[Si(CH_3)_3]_2$ NH, is used for capping the grain boundary in the gel.[19]

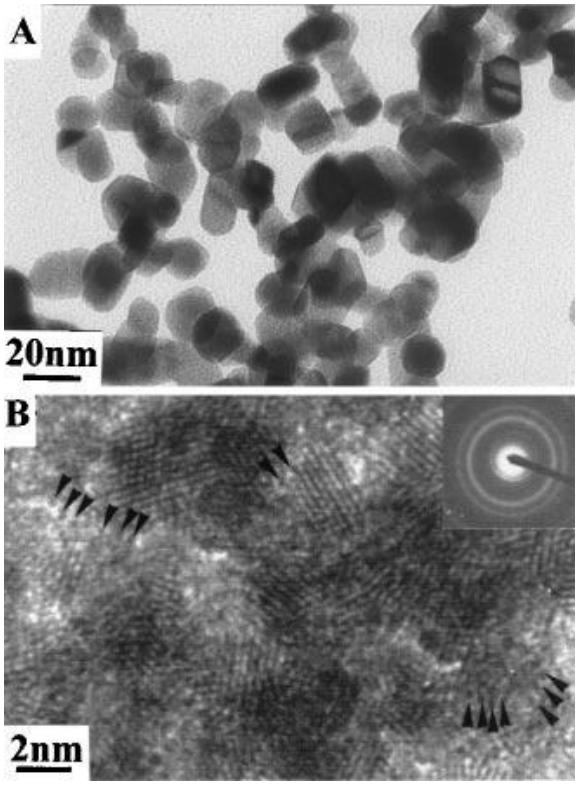

Figure 1.2 Transmission electron micrographs of (A) Untreated-SnO_2 and (B) HMDS treated-SnO_2 gels fired at 500°C for 1 hour in air. The inset in (B) shows the large-area electron diffraction pattern, and the arrows indicate possible "pinning" particles.[19‡]

‡ From [Inhibition of Crystallite Growth in the Sol-Gel Synthesis of Nanocrystalline Metal Oxides, N.-l. Wu, S.-Y. Wang, and I.A. Rusakova, Science **285**, 1375-1377 (1999)]. Reprinted with permission from AAAS.

Unlike ZnO, where a variety of morphologies and nanostructures are reported to form by using electrochemical deposition at different potentials in various electrolytes and concentrations,[41,42] there are very few reports on the electrochemical deposition of TO nanostructures.[25,43] A closer look at the Pourbaix diagram of Sn in Figure 1.3, as reported by Chang et al.,[43] for the typical concentration of 25 mM and at 70°C, shows that the ionic species of Sn exist only at extreme high and low pH values and there is a small range of potential, ca. 0.5 V, that can be applied to Sn^{2+} ion before it becomes oxidized to SnO_2. Due to the extreme pH conditions there are a rather limited number of substrates resistant to these harsh acidic and basic conditions that can be used for depositing SnO_2. On the other hand, the small potential interval that can be used for directing the growth would make the control on the growth of the nanocrystallites very limited. As can be observed for the reports on the electrodeposition of SnO_2, either the deposited layer is amorphous and needs further annealing similar to the sol-gel method in order to obtain crystalline SnO_2,[25] or a complex voltage pulsing sequence is required, which leads to the formation of Sn metal impurity in the crystalline SnO_2.[43]

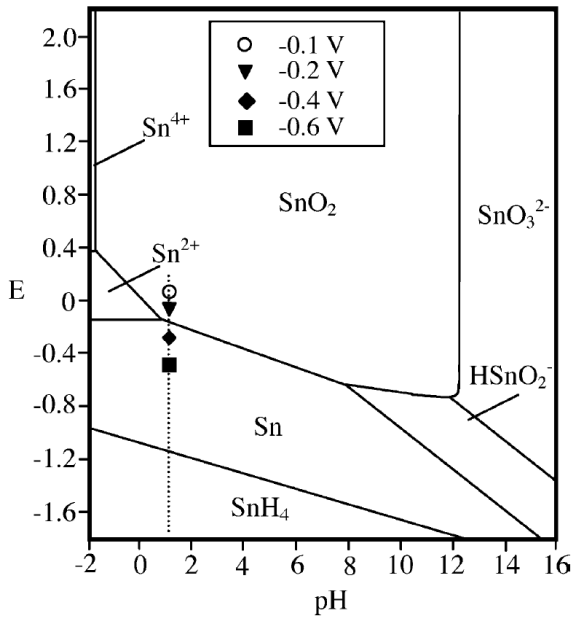

Figure 1.3 Atlas of electrochemical equilibrium of Sn at 70°C for a concentration of Sn species of 25 mM.[43§]

[§] Reprinted from Journal of Alloys and Compounds **403,** S. Chang, I. Leu, and M. Hon, Novel methods for preparing nanocrystalline SnO and Sn/SnO composite by electrodeposition, 335-340, Copyright (2005), with permission from Elsevier.

1.3.2 Single-crystalline faceted nanostructures

Nanocrystalline films of TO, which are prepared using different methods and often involve annealing steps for obtaining TO nanocrystallites, usually have granular structure with round, nearly spherical shapes, as crystallization often initiates by nucleation inside an amorphous phase. In addition to these granular nanostructured TO films, a variety of single-crystalline faceted nanostructures of TO have also been synthesized using different methods. Synthesizing these nanostructures have attracted a lot of attention due to the novel growth mechanisms involved in the formation and growth of these structures, and understanding these mechanisms is of great scientific and technological importance. One of the most widely used methods for synthesizing these "self-assembled" nanostructures with one or two dimensions in the nanoscale is the vapor transport method (thermal evaporation). A typical set-up for this deposition method is shown schematically in Figure 1.4. The system is first evacuated to the pressure of ~10^{-3} Torr and then the precursor material is evaporated inside a tube furnace with the vapor being transported through the tube by a carrier gas to where the final product is formed downstream in the tube and on the appropriate substrate.

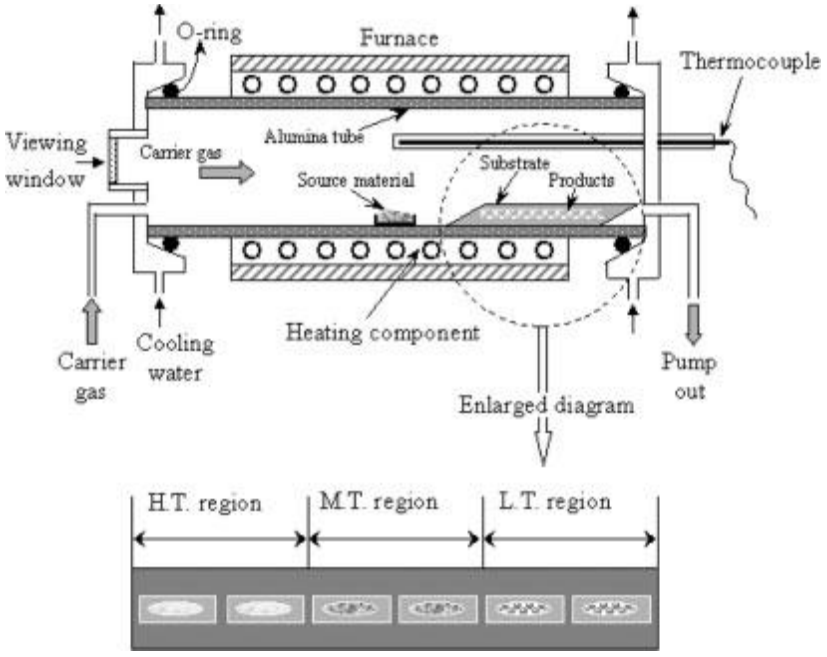

Figure 1.4 Schematics of the system used for vapor transport (thermal evaporation) deposition of nanostructures.[44**]

** Reprinted from [Novel Nanostructures of Functional Oxides Synthesized by Thermal Evaporation, Z.R. Dai, Z.W. Pan, and Z.L. Wang, Advanced Functional Materials **13**, 9-24] Copyright (2003) with permission from WILEY-VCH Verlag GmbH & Co. KGaA, Weinheim.

A variety of TO nanostructures have been reported to form using this general method, in which changing the precursor material, the position of the substrate in the tube, the temperature at which the substrate is kept, and the carrier gas composition all play important roles. Figure 1.5 shows a nanoribbon structure that was obtained by Dai et al.[26] using this method, which involved evaporating either SnO powders at 1000°C or SnO_2 powders at 1350°C in the centre of an alumina tube. The alumina plates were located at the temperature range of 900-950°C downstream, where the Ar gas carried the vapor with a flow rate of 50 sccm. The alumina plates were covered with these nanoribbon structures after deposition for 2h. These nanoribbons are reported to be several hundred micrometers in length with rather uniform width of 30-200 nm while the width-to-thickness ratios of 5-10 are observed. These single-crystalline nanoribbons are shown to have an axial growth direction of [101] with the wide-side surface close to the (1 0 -1) plane and narrow-side surface of (0 1 0). Dai et al. suggested that the observed (1 0 -1) plane for the wide surface is formed due to the low surface energy of these closest packing plane for Sn, while the (2 0 1) plane in the growth front has a higher surface energy leading to a faster growth rate and the observed large lengths.

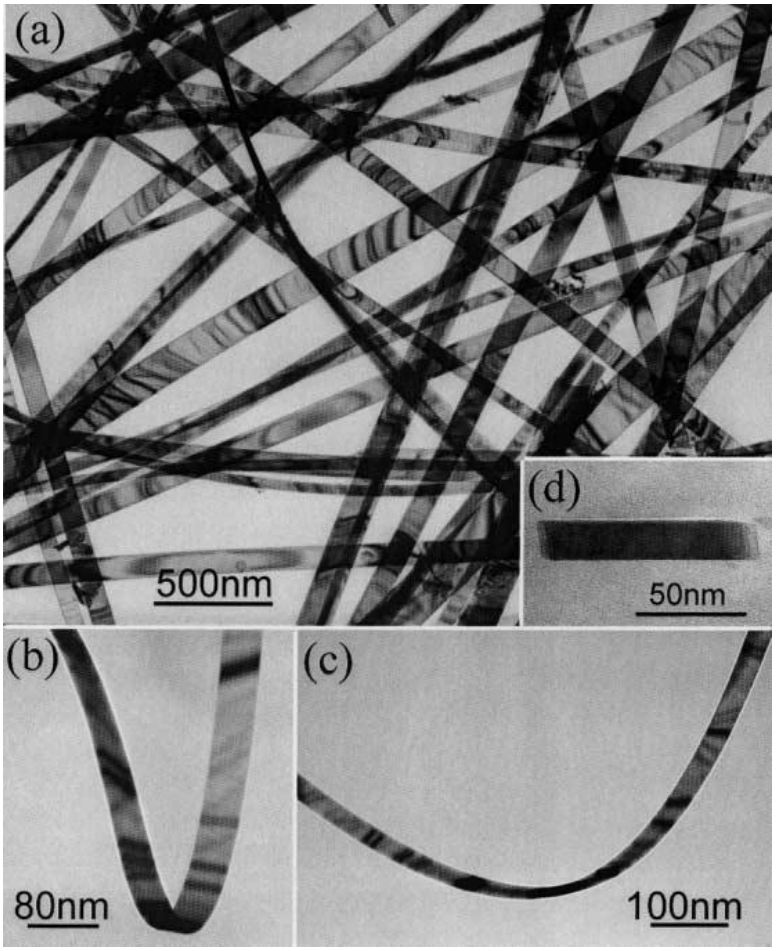

Figure 1.5 (a) TEM bright-field image of SnO_2 nanoribbons, showing strain contrast introduced by the bending of the nanoribbon. Each nanoribbon is singly crystalline without dislocation. (b) and (c) display the characteristic features of SnO_2 nanoribbons. (d) Cross-sectional TEM image of a nanoribbon embedded in epoxy and sliced with an ultramicrotome.[26††]

Using the same method of evaporating Sn/SnO and SnO mixtures at a temperature range of 1050°C to 1125°C with N_2 as the carrier gas at a flow rate of 100 sccm, various other morphologies have also been obtained by Dai et al.[28] and these include tetragonal TO nanowires, orthorhombic TO nanowires, and TO nanotubes. These products were either collected on the alumina tube wall, where the temperature was 450-500°C or deposited onto a cold plate (inserted into the tube) kept at 25-40°C by water cooling. In the case of TO nanowires, they were formed by evaporating Sn/SnO mixture and

†† Reprinted from Solid State Communications **118,** Z.R. Dai, Z.W. Pan, and Z.L. Wang, Novel methods for preparing nanocrystalline SnO and Sn/SnO composite by electrodeposition, 351-354, Copyright (2001), with permission from Elsevier.

collected on the tube walls. These straight nanowires with a single-crystalline structure (shown in Figure 1.6) exhibit a broad range of diameters from several tens of nanometers to micrometers, and for nanowires with the larger diameters defects and twin structures are observed. Interestingly, the side-surface planes and the growth direction of these nanowires are similar to those of the nanoribbons mentioned above. Not all of these synthesized nanowires have tetragonal structure. Dai et al.[28] have also reported nanowires with a super-structure as observed in the selected area electron diffraction (SAED) pattern of Figure 1.7 as weak reflections, and the authors assigned these super-structure to the orthorhombic phase of TO, which is known to form for the bulk TO at high pressures. These nanowires are obtained at a furnace temperature of 1050°C and a chamber pressure of 200 Torr, and the sample was collected from the cold plate kept at 25°C.

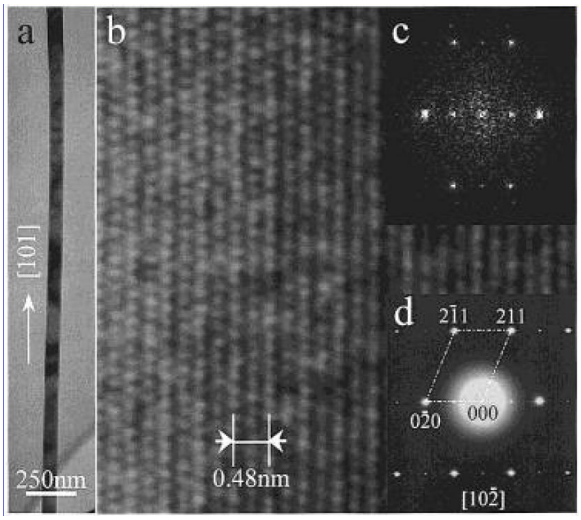

Figure 1.6 (a) Low magnification TEM image of a rutile structured TO nanowire. (b) High-resolution TEM image of the nanowire. (c) Corresponding FFT of the image, and (d) SAED pattern obtained from the nanowire.[28‡‡]

‡‡ Reprinted with permission from [Tin Oxide Nanowires, Nanoribbons, and Nanotubes, Z. R. Dai, J. L. Gole, J. D. Stout, and Z. L. Wang, The Journal of Physical Chemistry B **106**, 1274-1279]. Copyright (2002) American Chemical Society.

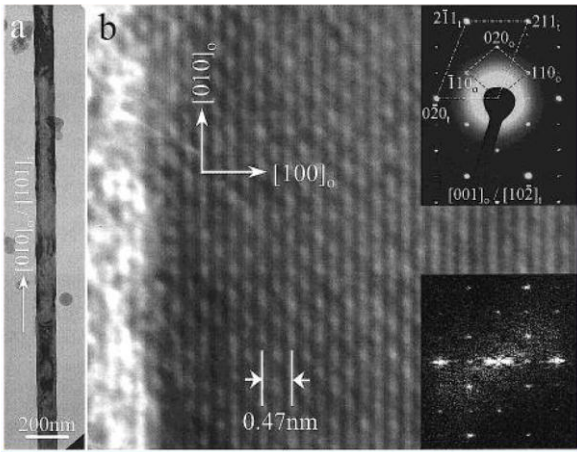

Figure 1.7 (a) Low magnification TEM image of an individual orthorhombic TO nanowire, and (b) the corresponding HRTEM image. The inset at the upper right-hand corner is a SAED pattern obtained for the nanowire shown in (a) and the inset at the bottom right-hand corner is a FFT of the HRTEM image.[28§§]

At a furnace temperature of 1100°C with a SnO powder source and a chamber pressure of 250 Torr, nanotubes of TO, shown in Figure 1.8, formed on the tube walls were reported by Dai et al.[28] The bright contrast at the centre of these structures has led the authors to conclude that these structures have hollow cores. These nanotubes have diameters in the 50 nm to 350 nm range and they also show a super-structure attributable to the orthorhombic phase similar to the nanowires described above.

[§§] Reprinted with permission from [Tin Oxide Nanowires, Nanoribbons, and Nanotubes, Z. R. Dai, J. L. Gole, J. D. Stout, and Z. L. Wang, The Journal of Physical Chemistry B **106**, 1274-1279]. Copyright (2002) American Chemical Society.

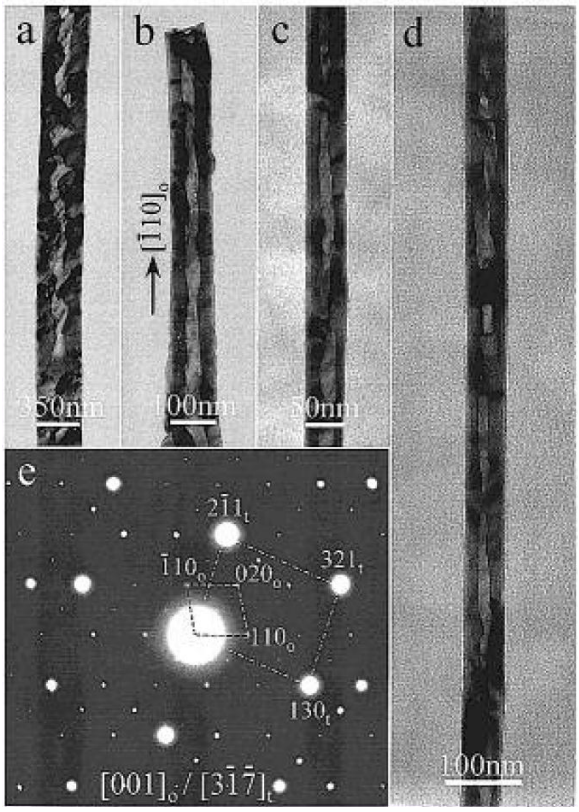

Figure 1.8 (a), (b), and (c) are TEM images of TO nanotubes, and (d) a SAED pattern taken for the TO nanotube shown in (b).[28***]

Another example of the nanostructures grown using this method is the SnO nanodiskettes reported by Dai et al.[45] As shown in Figure 1.9, these nanostructures were obtained on alumina plates located downstream at a temperature range of 200-400°C with 50 sccm of Ar at a pressure of 500-600 Torr, where SnO or SnO_2 source powders were used for evaporation at 1070°C and 1350°C, respectively. The typical diameter of the diskettes is 8-10 μm with the thickness in the several tens to several hundreds of nanometers, leading to a diameter-to-thickness ratio of ca. 15. These nanodiskettes were reported to be always growing together with nanobelts and often a mechanical shaking was required to separate these structures. These diskettes were also reported to have two different kinds, where type I as shown in Figure 1.9 has a flat surface while the type II diskettes have terraces and spiral steps on their surface. The authors have also reported the oxidation of these SnO diskettes to obtain

*** Reprinted with permission from [Tin Oxide Nanowires, Nanoribbons, and Nanotubes, Z. R. Dai, J. L. Gole, J. D. Stout, and Z. L. Wang, The Journal of Physical Chemistry B **106**, 1274-1279]. Copyright (2002) American Chemical Society.

TO, which was reported to occur through decomposition and oxidization processes. In addition to these diskettes, blocks of TO were also found to grow in the low temperature zone of the furnace as reported by Dai et al.[44] Moreover, nanodendrites were observed to grow also in the low temperature zone upon increasing the SnO source temperature to 1100°C and at high pressure of 500-600 Torr, as reported by Dai et al.[44] In addition, fishbone-like nanoribbons were reported by Hu et al.,[46] using the thermal evaporation method with a $Sn/Fe_3(NO_3)_3$ powder source.

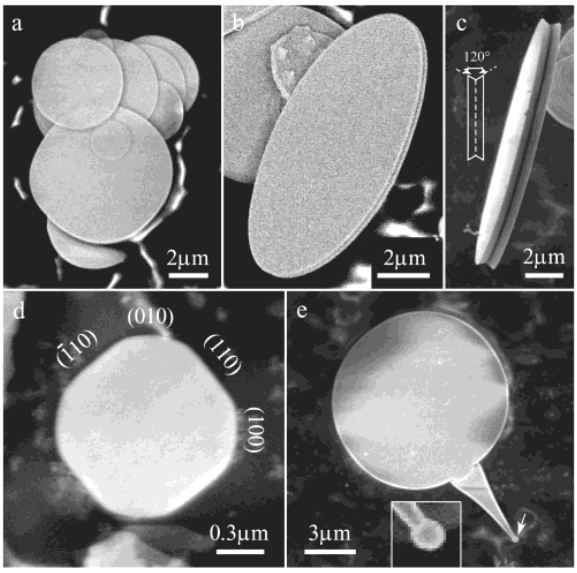

Figure 1.9 SEM images showing morphology of type I SnO diskettes. The inset in (c) shows a schematic of side view of the shape of these diskettes. The inset in (e) is an enlarged image of the tip marked by the arrow, which indicates that the tip is a spherical ball.[45†††]

Thermal evaporation however is not the only method used for growing TO nanostructures and a variety of other nanostructures obtained by using different techniques have also been reported. For example, Liu et al. [47] have grown "nano-box-beams" of TO using a combustion chemical vapor deposition technique, where tin (II)-2-ethylhexaonate dissolved in ethanol is mixed with high-purity oxygen in a nanomizer, producing a microscale mist in a flame. A quartz substrate positioned inside or near the flame acted as the substrate at growth temperatures of 950°C and 1150°C for 30 min and 60 min deposition time.[47] Figure 1.10 shows the outcome of this deposition as "nano-box-beams" of TO, 0.5-2.0 μm wide and up to 7 μm long. These nanostructures were found to be hollow with well-

††† Reprinted with permission from [Growth and structure evolution of novel tin oxide diskettes. Zu Rong Dai, Zheng Wei Pan, and Zhong L Wang, Journal of the American Chemical Society **124**, 8673-80]. Copyright (2002) American Chemical Society.

defined square or rectangular cross-sections with a wall thickness of ca. 50 nm. TEM studies performed on these nanostructures showed that all the four peripheral surfaces are {110} planes and the tubular growth is along the [001] direction.

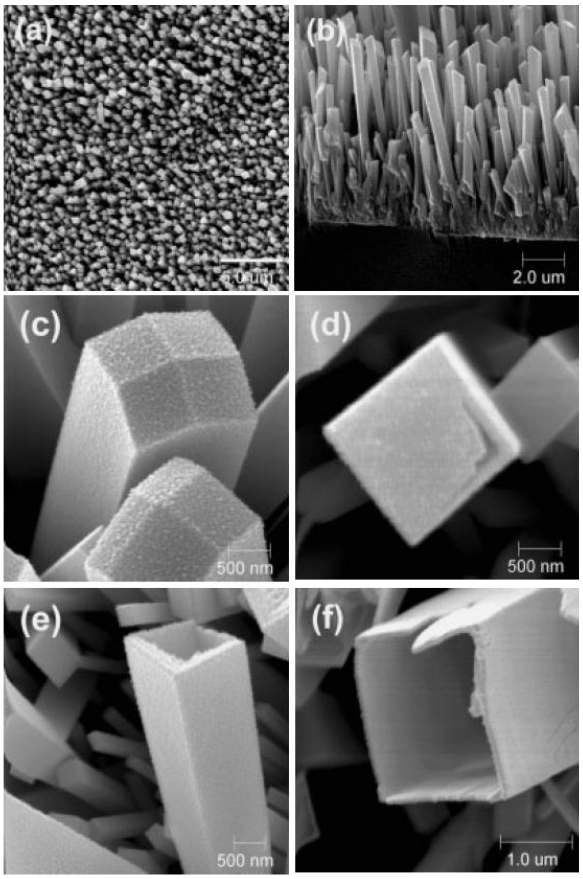

Figure 1.10 Typical microscopic features of TO box-beams synthesized at 1150°C for 30 min. (a) Top view of a box-beam array. (b) Cross-sectional view of a box-beam array. (c) TO box-beams with an end cap of multiple facets. (d) A TO box-beam with a partially broken end plate. (e,f) Broken TO box-beams showing the hollow structure and wall thickness.[47‡‡‡]

Growth of nanoneedles of TO obtained by using a glow discharge method was also reported by Wang et al.[48] The chemically produced SnH_4 gas was fed into a tube furnace, kept at 800°C. By applying an alternating high voltage to the copper pipes inserted in the tube, a stable glow discharge plasma was obtained and used to create TO nanoneedles on a gold-coated porous Si substrate. Huang

‡‡‡ Reprinted from [Well-Aligned"Nano-Box-Beams" of SnO_2, Y. Liu, J. Dong, and M. Liu, Advanced Materials **16**, 353-356] Copyright (2004) with permission from WILEY-VCH Verlag GmbH & Co. KGaA, Weinheim.

et al.[49] also reported the synthesis of TO nanorods by depositing TO thin films using a plasma-enhanced chemical vapour deposition method followed by the inductive coupled plasma treatment of the films. The authors proposed that a sputtering redeposition mechanism causes the formation of the nanorods, which emerged after treatment for 5 min and grew longer by increasing the plasma treatment time. These nanorods are needle-like with a diameter of 5-15 nm and a length of 200-300 nm with {110} side planes and a growth axis of [110].

1.3.3 One-dimensional (1D) Nanostructures

The great diversity of the morphologies that can be obtained for TO is one of the main factors that attracts more attention towards this material, because new morphologies can potentially offer new properties and new applications with this material. The observed room-temperature photoluminescence peak centered around 500 nm is one of these good examples that shows that the new (photoluminescence) property was associated with the fishbone-like structure of the nanoribbons as reported by Hu et al.[46] The observed increase in the gas sensing property of the single nanorod H_2 sensor at low concentration of 100 ppm and at a low temperature of 25°C, reported by Huang et al.,[50] is another example, which illustrates the enhanced property of TO due to its morphology.

Among all the observed single-crystalline TO nanostructures, 1D nanostructures are of great importance. They have a uniform cross-section over a long length and can be easily integrated into devices, e.g., as interconnectors and field-effect transistors. Some examples of the TO devicesbuilt using these 1D nanostructures have been reported in literature and the interdisciplinary research has led to an increased number of applications of these nanostructures in different fields. Comini et al.[51] showed that by using a TO nanoribbon in building a gas sensor, sensitivity of the sensor was remarkably improved for sensing ethanol and NO_2 gases. The TO nanoribbons used for these devices were grown using a thermal evaporation method and had wide-side surface planes of {101} and narrow-side surface planes of {010} with a growth axis of [101]. The width of these nanoribbons was ~ 200 nm with a width-to-thickness ratio of 5-10. The contacts were shown to be ohmic, and as can be seen in Figure 1.11, a sensitivity of 4160% was observed for 250 ppm of ethanol at aworking temperature of 400°C, and a sensitivity of -1550% is observed for 0.5 ppm of NO_2 at aworking temperature of 400°C. Moreover, TO nanobelts have also used for fabricating a field-effect transistor by Cheng et al.,[32] where the characteristic operation of the FET device is shown in Figure 1.12 along with the results of the pH sensing of this device. Cheng et al. have also functionalized the nanobelts

along with passivation of the other surfaces, which has led to an improved signal-to-noise performance. This result shows that further application of 1D TO nanostructures for other chemical and biological sensing purposes is also possible.

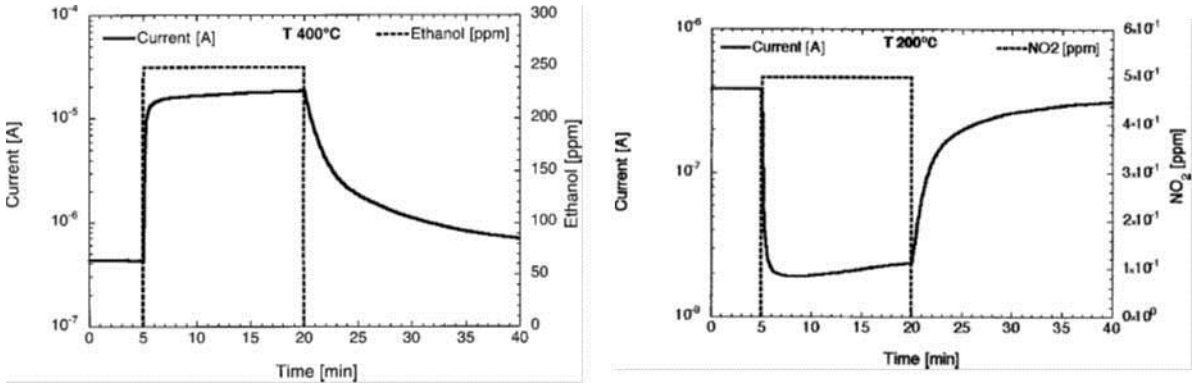

Figure 1.11 Response of the TO nanobelt sensor to ethanol (left) and to NO_2 (right) gases at the working temperature of 400°C.[51§§§]

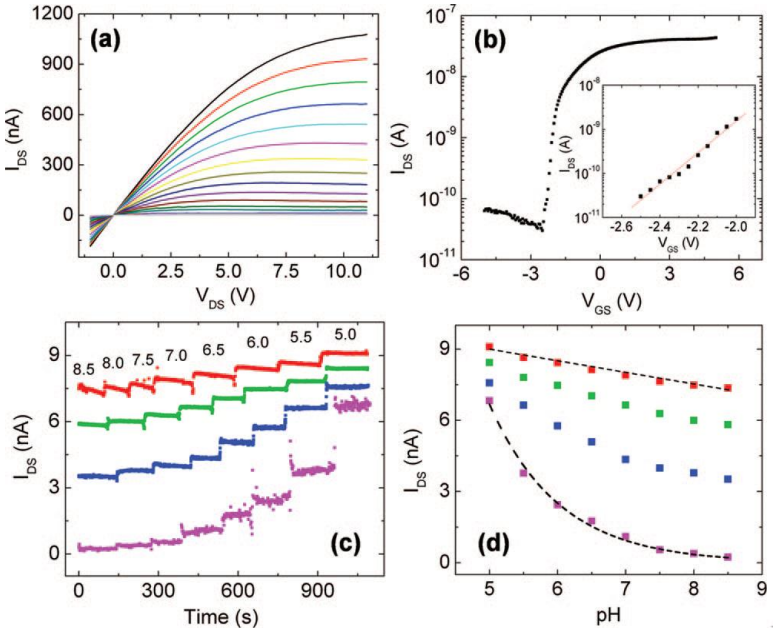

Figure 1.12 Characteristic and pH sensing of a TO nanobelt FET. (a) I_{DS} (drain-to-source current) versus V_{DS} (drain-to-source voltage) at V_{GS} (gate-to-source voltage) from 5 to -5 V (top to bottom) in steps of 0.5 V, exhibiting typical n-channel depletion mode behavior. (b) Transfer characteristics, I_{DS}

§§§ Reprinted with permission from [Stable and highly sensitive gas sensors based on semiconducting oxide nanobelts, E. Comini, G. Faglia, G. Sberveglieri, Zhengwei Pan, and Zhong L. Wang, Applied Physics Letters **81**, 1869]. Copyright [2002], American Institute of Physics.

versus V_{GS} at V_{DS}=0.2 V. Inset shows the sub-threshold regime with a subthreshold swing of 280 mV/dec. (c) Real-time I_{DS} response to eight 10 mM sodium phosphate solutions of different pH at V_{GS}=2.0, 0, -1.5, -2.5 V (from top to bottom). (d) I_{DS} versus pH at different gate voltage V_{GS}=2.0, 0, -1.5, -2.5 V (from top to bottom). The dashed line and curve represent linear and exponential fits to the data in the linear transport (V_{GS}=2.0 V) and sub-threshold (V_{GS}=-2.5 V) regimes, respectively.[32****]

Law et al.[33] have used TO nanoribbons as waveguides with a continuous-wave laser light (3.8 eV) focused on one end of the nanoribbon, and recorded the transported light at the other end of the nanoribbons with hundreds of micron in length. As can be seen in Figure 1.13, in spite of the long length and the presence of sharp turns in the structure of the nanoribbon, the light was strongly guided by the cavity similar to the performance of a optical fiber. They also showed that coupling between different nanoribbons or even between nanoribbons of TO and nanowires of ZnO were also possible where light was transmitted from one nanoribbon to the other. These results illustrate promising performance of these structures for photonics circuitry and nanophotonic applications.

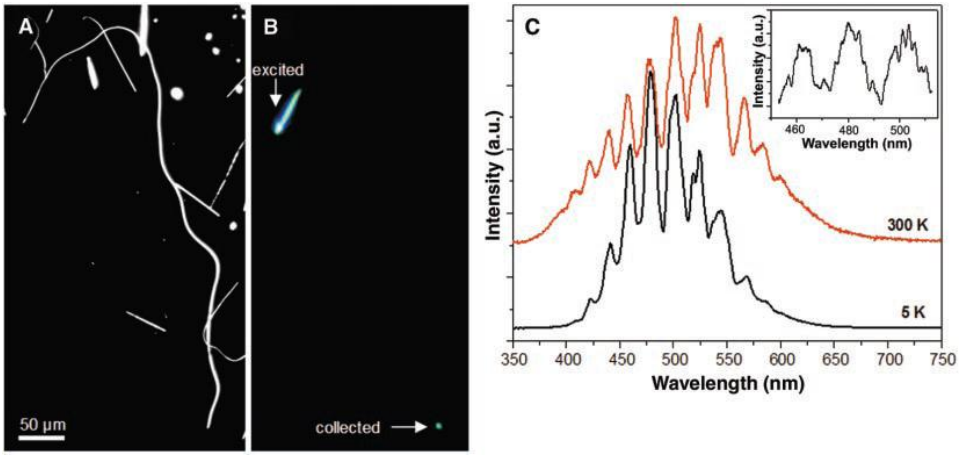

Figure 1.13 Optical waveguide performance of a 715 μm-long TO nanoribbon. (A) A dark-field image of the meandering ribbon (350 nm wide by 245 nm thick) and its surroundings. (B) The photoluminescence image of the nanoribbon waveguide under laser excitation. The laser was focused to a spot size of ~ 50 μm (30° incidence angle) at the top end of the ribbon. (C) Spectra of the emission from the bottom terminus of the waveguide, collected at room temperature and 5 K. The mode structure does not change substantially with temperature, suggesting minimal dependence on

**** Reprinted with permission from [Mechanism and optimization of pH sensing using SnO2 nanobelt field effect transistors, Yi Cheng, P Xiong, C Steven Yun, G F Strouse, J P Zheng, R S Yang, and Z L Wang, Nano Letters **8**, 4179-84]. Copyright (2008) American Chemical Society.

the variation in the index of refraction. A higher resolution emission profile (inset) shows the fine structures in three of the central peaks.[33††††]

Synthesis of 1D semiconducting oxides, both pristine and doped forms, is therefore of special interest because all the proven and potential applications of these structures depend on the control on their cross-sectional size and shape, growth axis, and side-surface planes. A variety of fabrication techniques have been attempted to synthesize 1D TO nanostructures, and they include the aforementioned thermal evaporation method,[28] laser-assisted evaporation,[29,31] spray pyrolysis method,[52]and solution-phase syntheses.[53,54] In the laser-assisted evaporation method, which has been used for synthesizing a variety of 1D nanostructures, including Si and Ge,[55] and a wide range of III-V and II-VI semiconductors such as GaAs and CdS,[56] a precursor material was first evaporated using a laser beam, and the vapor was then thermalized and transported downstream by a carrier gas to undergo further reactions or just to be deposited onto a substrate at a specified temperature. Hu et al.[29] have used an excimer laser to ablate a SnO_2 target inside a tube furnace evacuated to a base pressure of 10^{-2} Torr and kept at 900°C, but they have not used any carrier gas. The as-grown structures on the wall of the quartz tube, as can be seen in Figure 1.14, have a ribbon morphology with a typical width of 300-500 nm and a thickness of 30-50 nm. The corresponding XRD results showed the formation of just a single tetragonal phase of TO and the TEM results, as shown in Figure 1.15, indicated a growth axis of [100]. Although Hu et al. have not mentioned the side-surface planes of the nanoribbons, the indexing in the HRTEM image showed wide-side surface planes of {001} and narrow-side surface planes of {010} for these nanoribbons, Figure 1.15.

†††† From [Nanoribbon waveguides for subwavelength photonics integration' Matt Law, Donald J Sirbuly, Justin C Johnson, Josh Goldberger, Richard J Saykally, and Peidong Yang, Science (New York, N.Y.) **305**, 1269-1273 (2004)]. Reprinted with permission from AAAS.

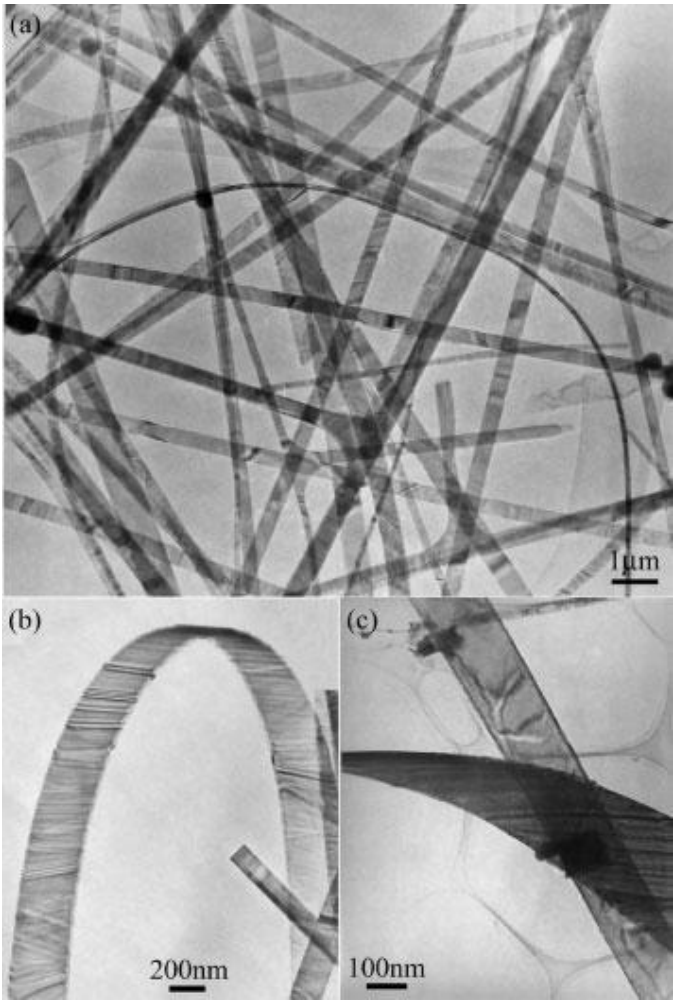

Figure 1.14 TEM images of (a) numerous TO ribbons, (b,c) individual twisted TO ribbons.[29‡‡‡‡]

‡‡‡‡ Reprinted from [Laser-Ablation Growth and Optical Properties of Wide and Long Single-Crystal SnO_2 Ribbons, J.Q. Hu, Y. Bando, Q.L. Liu, and D. Golberg, Advanced Functional Materials **13**, 493-496] Copyright (2003) with permission from WILEY-VCH Verlag GmbH & Co. KGaA, Weinheim.

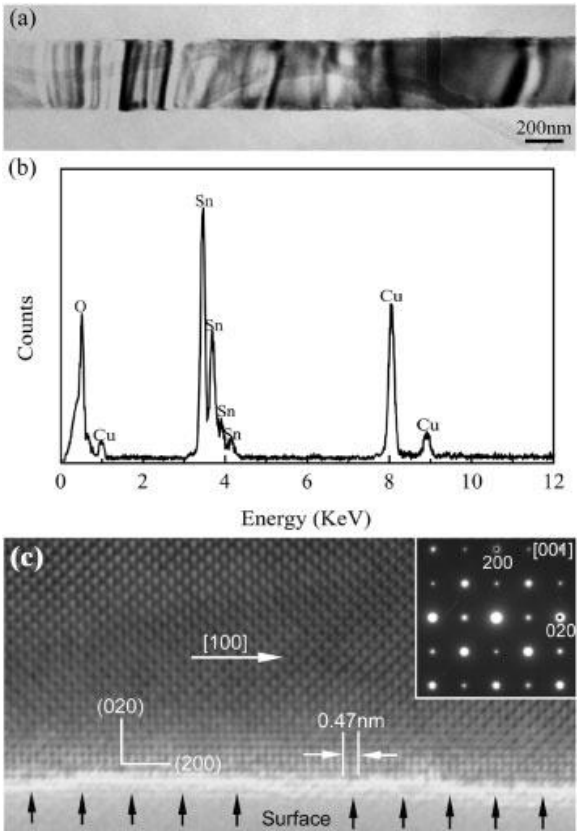

Figure 1.15 a) A straight TO ribbon. b) Energy dispersive X-ray spectrum and c) HRTEM image of the ribbon and its corresponding energy dispersive X-ray pattern (inset).[29§§§§]

Liu et al.[31] have also used the laser-assisted evaporation method for ablating a Sn target inside a tube furnace with a pulsed Nd:YAG laser. Sn vapor was then carried downstream by a 100 sccm flow of a dilute mixture of oxygen in the Ar gas towards a SiO_2-Si substrate, which was covered with Au nanoparticles. Reaction was carried out at 900°C for 10-30 min, while the pressure of the chamber was maintained at 400 Torr during the growth. The nanostructures so-obtained are TO nanowires with the tetragonal crystal structure of TO, as shown in Figure 1.16. There were Au/Sn particles at the tips of these nanowires, shown to be growing in the [100] direction in Figure 1.17. These nanowires have been reported to have diameters in the 15-25 nm range, but the cross-sectional shape of the nanowires has not reported. A FET device based on these nanostructures has also been

§§§§ Reprinted from [Laser-Ablation Growth and Optical Properties of Wide and Long Single-Crystal SnO_2 Ribbons, J.Q. Hu, Y. Bando, Q.L. Liu, and D. Golberg, Advanced Functional Materials **13**, 493-496] Copyright (2003) with permission from WILEY-VCH Verlag GmbH & Co. KGaA, Weinheim.

fabricated, which has been shown to exhibit excellent performance and used for measuring the UV response of the nanowires.

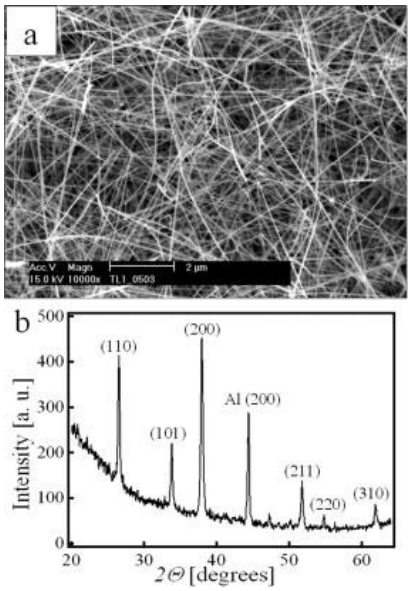

Figure 1.16 (a) SEM image of TO nanowires grown on a Si-SiO_2 substrate. (b) XRD pattern of these TO nanowires.[31*****]

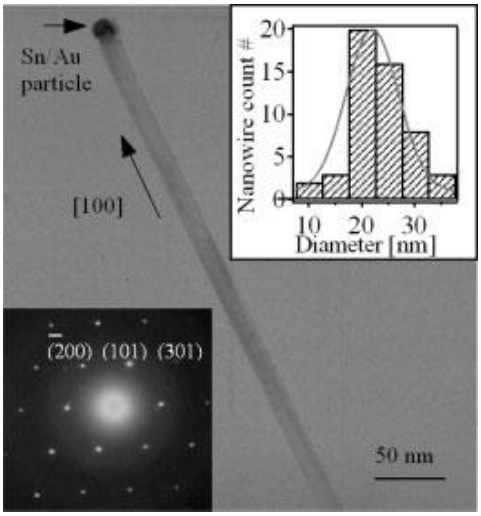

Figure 1.17 TEM image of a TO nanowire with a catalyst at the tip. Lower inset: SAED pattern taken perpendicular to the nanowire long axis. Upper inset: Histogram of the nanowire diameter distribution. The solid line is a Gaussian fit.[31†††††]

***** Reprinted from [Laser Ablation Synthesis and Electron Transport Studies of Tin Oxide Nanowires' Z. Liu, D. Zhang, S. Han, C. Li, T. Tang, W. Jin, X. Liu, B. Lei, and C. Zhou, Advanced Materials **15**, 1754-1757] Copyright (2003) with permission from WILEY-VCH Verlag GmbH & Co. KGaA, Weinheim.

Investigating the growth mechanism of these 1D nanostructures is also very important in determining the growth parameters, which can be used for controlling their morphology and crystal structure. Solution phase syntheses involve mechanisms specific to the reagents used and the reactions occurring in the solution phase, and each synthesis may involve a separate unique growth mechanism. In the case of deposition techniques that involve evaporating a precursor material and recrystallizing the vapor for formation and growth of a 1D nanostructure, two feasible growth mechanisms are often considered: vapor-solid (VS) growth, and vapor-liquid-solid (VLS) growth mechanism.

In the VS growth mechanism, which was first observed in the growth of whiskers on the metal surfaces, there is often no catalyst involved and the growth continues by deposition of vapor on the existing anisotropic growth sites. Frank's dislocation (screw dislocation) is one of the VS mechanisms that lead to the advancement of the growth front and formation of elongated nanostructures as vapor condenses on the existing dislocation with a high energy at the growth front as opposed to the side surfaces. Dai et al.[44] have proposed a mechanism for the growth of TO nanoribbons without catalyst, where the vaporized molecular species coordinate themselves into the low energy structure, creating the nucleation site (as is shown n Figure 1.18). Further growth of 1D nanostructures continues by rearrangement of molecules in a way that the low-energy surfaces form as side planes, while the high-energy growth front with steps and high-energy planes tend to grow faster. The high deposition temperature also helps the molecular species to have enough thermal energy to rearrange their positions on the surface of the growing nanostructure, which leads to the flat surface of the low-energy side surface planes. Although the possibility of formation of small metallic particles at top cannot be ruled out by ex-situ studies, exposure to air can oxidize the small metallic particles and remove the metallic signature.

VLS growth was first observed by Wagner and Ellis[57] for the growth of Si whiskers, where the melted droplet of the catalyst acts as an anisotropic point for the preferred absorption site of the vapor and for the directed growth of the nanostructure. The preferential absorption of the vapor into liquid catalytic droplet leads to the increase in the concentration of the vapor species in the droplet. Depending on the catalyst and the element, e.g. Si, involved in the growth, a binary phase diagram can help in understanding the growth mechanism and predict the required growth conditions.

However, in the case of oxides or other binary compounds like GaAs, the growh mechanisms in these systems will be more complicated. Duan et al.[56] propose that in the case of 1D growth of binary compounds, a pseudo-binary phase diagram could be used. As shown in Figure 1.19, the phase transition temperature and compositions can be treated as in a typical binary phase diagram. Above the eutectic line in the phase diagram (630°C in the case of Au-GaAs), the catalyst is in the liquid state. Upon absorbing the vapor, the composition of the droplet can be changed, causing a horizontal shift in the phase diagram. This then leads to precipitation of the compound of interest by super-saturating the catalyst at the phase boundary, i.e. L/L+GaAs(s) boundary in Figure 1.19.

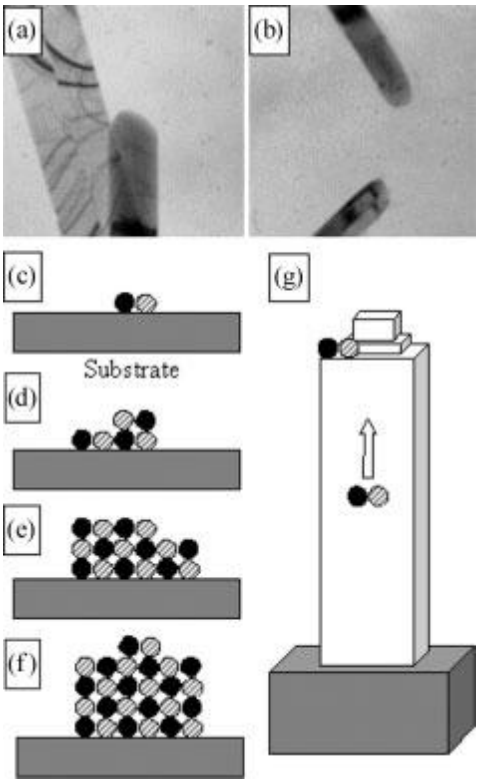

Figure 1.18 (a,b) The growth fronts/ends of ZnO nanobelts, showing no visible catalytic particles at the ends. (c-g) A possible growth process for the formation of the nanobelts.[44‡‡‡‡‡]

‡‡‡‡‡ Reprinted from [Novel Nanostructures of Functional Oxides Synthesized by Thermal Evaporation, Z.R. Dai, Z.W. Pan, and Z.L. Wang, Advanced Functional Materials **13**, 9-24] Copyright (2003) with permission from WILEY-VCH Verlag GmbH & Co. KGaA, Weinheim.

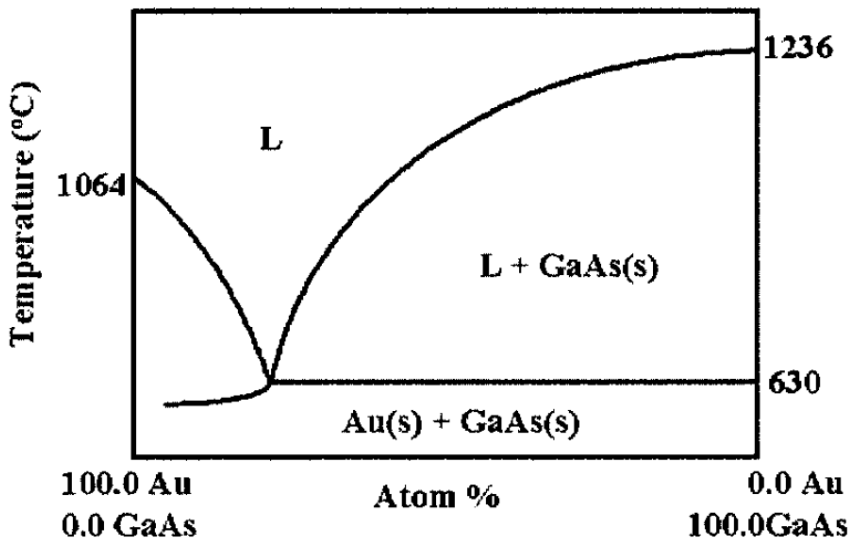

Figure 1.19 Pseudobinary phase diagram for Au and GaAs. The liquid Au-Ga-As component is represented as L.[56§§§§§]

1.4 Motivations and Scope of the Thesis

In the present work, a series of detailed studies are performed on the synthesis and growth mechanism of both the nanocrystalline TO films and faceted, highly crystalline TO nanostructures. A spin-coating method is used for the fabrication of nanostructured TO films, while a pulsed laser deposition method is employed for the growth of various nanostructures of TO with the emphasis on the growth of one-dimensional TO nanostructures. We have addressed some of the challenges in the growth and in the control on the size, shape and dimension of TO nanostructures using these two methods. Moreover, the basic physical properties of these TO nanostructures are studied, and the control on the properties of these nanostructured materials by manipulating the growth parameters is also explored.

The adsorption of charged oxygen species creates a charge-depleted layer on the surfaces of TO grains and therefore reduces the size of the conduction channels of the carriers. The size of this depletion layer depends on the Debye length of the material,[58] which is controlled by the carrier concentration. By decreasing the size of the TO grains to that comparable with the Debye length, the effects of the depletion layer in modifying the conduction channels become more pronounced.

§§§§§ Reprinted from [General Synthesis of Compound Semiconductor Nanowires, X. Duan and C. M. Lieber, Advanced Materials **12**, 298-302] Copyright (2000) with permission from WILEY-VCH Verlag GmbH & Co. KGaA, Weinheim.

Depending on the average size of the crystalline grains (D) relative to the Debye length (L_D), different conduction regimes are at work, including grain boundary-controlled ($D \gg 2L_D$), neck-controlled ($D \geq 2L_D$), and grain-controlled ($D < 2L_D$), as illustrated by Barsan et al.,[59] Yamazoe,[58] and Seal et al.[14] For TO nanostructures with grain sizes in the neck-controlled and grain-controlled regimes, the depletion layer completely blocks the conduction channel, causing a pronounced change in the resistivity of the sample. The nanocrystalline films of TO are therefore promising candidates for improving the sensitivity of the available solid-state gas sensors. However, there are some major challenges in using these nanocrystalline films for sensing applications.[14] Since the Debye length is ~3 nm for a pure nanostructured TO film,[60] crystallite sizes below 10 nm are required in order to observe the size enhancement effects on the sensitivity. Nanocrystallites in this size range (below 10 nm) are, however, not stable in the working conditions of the gas sensors, which usually require heating up to ~ 400°C causing these nanocrystallites to grow through an Ostwald ripening mechanism. This change in the size introduces instability in the response of the sensor and the sensitivity is reduced due to the increase in the crystallite size. In addition to the importance of the SnO_2 crystalline grain size for gas sensing applications, the conductivity of the film is also of great interest to their applications as transparent conducting electrodes or active semiconducting layers in organic electronics[39,61,62] and in transparent thin-film transistors.[6] There are several challenges in modifying or improving some of the properties of the SnO_2 layers for these applications. In particular, controlling the surface roughness and the uniformity of the SnO_2 film are crucial for minimizing current leakage problems in device applications, while improving the quality of the interface between the SnO_2 layer and other layers would improve the charge transport and functionality of the device. Understanding the structural, physical, and chemical properties of SnO_2 and the changes that can be induced in its structure and consequently its other properties can offer new routes to address the challenges associated with this material. Therefore in Chapter 3, nanocrystalline TO films are synthesized by using a spin-coating method and the growth mechanism of the crystalline grains in these thin TO films is investigated. Moreover, the effect of different parameters on the growth of these nanostructures is explored.

The charge transport in nanocrystalline TO structures is complex and is different from bulk charge transport in several aspects. In bulk semiconducting TO films, conduction originates from n-type carriers, which have been proposed to be due to oxygen deficiencies, Sn interstitials, crystalline defects,[1] or hydrogen doping.[4] Moreover, different charge trap levels with different activation energies are observed in these films, depending on their synthesis methods. In the case of

nanocrystalline films, the small size of the crystallites and their interconnections, as well as any gaseous species adsorbed on their large surface areas can further modify their charge transport properties. In particular, for nanocrystallites smaller than 10 nm, the radius of the nanocrystallite becomes comparable to the Debye length (calculated to be ~3 nm for SnO_2 at 250°C [60]), which corresponds to the approximate size of the charge-depletion layer created by an adsorbed species.[63] The comparable size of the charge depleted region to the size of the nanocrystallite and the significant surface-to-volume ratio in these films can result in drastic changes in the conduction channel and in the charge transport through the nanocrystallites and their interconnections upon exposure to different gas species.[7,14] Depending on the size of the conduction channels relative to the mean free path of the carriers, charge carrier scattering effects can also be induced.[63] In chapter 4, the band structure, and the carrier transport mechanism in nanocrystalline TO films obtained using the spin-coating method are studied. The optical transmission data is used to investigate the band structure and the absorption edge of the samples. Resistivity measurements are also performed to study the change in the electronic properties of samples upon structural evolution of the samples and upon changes in the nanocrystallite size in the 4-12 nm range. These nanocrystalline samples are composed of both amorphous and crystalline phases and these studies shed new light on the formation of conduction channels and electronic transport in these phases.

One of the common approaches in creating or modifying properties of TO, and functional oxide materials in general, is doping the structure with an appropriate dopant. For example, Sb and F are among the most common dopants used for increasing the conductivity of TO,[3] while magnetic dopants such as Fe and Co have been used for inducing magnetization.[17] Various metal dopants, e.g. Pd, Pt, Cu, and Ag, have been used to provide selective chemical sensing in TO.[7] TO and, in general, the wide band-gap semiconducting oxides exhibit photoluminescence due to the abundance of defects in their structure, which act as radiative recombination centers as well as carrier generators in these oxides.[1,64] However, the emission peaks generated by these intrinsic defects are very broad, and there is limited to no control on their emission wavelength. In order to obtain a sharp emission spectrum with control on the emission wavelength, different doping studies have been performed on incorporating rare earth ions, including Eu, Tb, Ce, Tm, Ho, and Nd, which have their characteristic electronic transitions ranging from UV to infra-red.[16,65] Moreover, doping for nanoparticles and other nanostructures is of special interest due to the enhanced luminescence that occurs because of the quantum size effects and/or the improved energy transfer in these nanostructures as reported for Mn-doped ZnS nanoparticles [66] and Eu-doped SnO_2/SiO_2 glasses.[67] Furthermore, monochromatic

emission of doped TO nanoparticles can lead to their potential applications as bio-labels/markers or as nanophosphors in displays and optoelectronic devices.

The Eu^{3+} ion is of particular interest due to two characteristic orange emissions at ~614 nm and 593 nm, which correspond to an electric dipole transition ($^5D_0$-$^7F_2$) and a magnetic dipole transition ($^5D_0$-$^7F_1$), respectively.[16] Depending on the symmetry of the occupancy site of Eu^{3+} ion in the lattice, only one of the two transitions can occur because of the different nature of these transitions. Since an electric dipole transition is only allowed in a non-symmetric crystal field, substitution in the symmetric sites will produce predominantly the 593 nm emission, while non-symmetric site occupancy will lead to a dominant 614 nm emission.[68] Different methods including sol-gel,[69,70] solid-state reaction[71] solvothermal,[23] and other solution-phase techniques [22,72,73] have been employed for doping rare earth ions (including Eu^{3+}) into the nanostructures of TO. Nanoparticles of TO with dopant concentrations of up to the solubility limit of the dopant, typically 5 mol. %, are produced by using these methods. Depending on the synthesis route and on the type and concentration of the dopant, high-symmetry cationic substitutional site or low-symmetry interstitial site and surface/interface of the nanoparticles are preferred. Moreover, the energy transfer from the host to the ion also varies with different fabrication methods and different site occupancies. The spin-coating method discussed in Chapter 3 provides an easy way of doping the TO nanostructures by homogenously dissolving the dopant of interest in the precursor solution. Moreover, annealing temperature of the films can be used to control the crystallite growth effectively, which can therefore allow us to study the effect of the grain size on the luminescence of the Eu^{3+} ions in the nanostructured TO film. In Chapter 5, we explore this opportunity and investigate the effects of doping these nanocrystalline TO films with Eu^{3+} ions. Unlike other synthetic methods including the colloidal chemistry methods, this spin-coating method allows us to incorporate high concentrations of Eu into TO structure, providing the possibility of investigating the structural transitions of these compounds at high Eu^{3+} concentrations and explore their optical and magnetic properties.

As discussed in the previous sections, there are many reports on using vapor transport techniques for the growth of one-dimensional nanostructures of TO.[26-29] In this type of thermal evaporation methods, the vapour is generated through evaporation of the source material and the resulting vapor is transferred by a carrier gas towards the substrate held at high temperature, 900-1000°C, in a tube furnace.[74] Pulsed laser deposition (PLD) is one of the main techniques and well-suited methods for depositing films of oxide materials with the capability of growing epitaxial oxide layers with the

appropriate choice of substrates. The PLD method offers several important advantages over the thermal evaporation and laser-assisted evaporation techniques:

- It is a high-vacuum deposition system, allowing for deposition of high quality materials without impurities and with a high degree of control on the growth conditions along with a precise control on the gas composition.
- The high energy of the laser can be used to evaporate oxides with high melting points that are not accessible to most furnaces.
- By adjusting the appropriate deposition conditions, the stoichiometry of the target material can be maintained and transferred over as the deposited material on the substrate, allowing deposition of complex oxides.
- Since the source target has the same stoichiometry as the final product, there is no need for further reactions in the gas phase (such as oxidization or reduction of the source material). Instead, combination of different gases can therefore be used as an important growth parameter to control the growth of the oxide.
- Using appropriate substrates and adjusting the substrate temperature during the deposition, epitaxial growth of the oxide in the desired crystalline orientation can be obtained.
- Using a multi target carousel assembly in the PLD chamber, multiple depositions using different targets can be performed, allowing fabrication of heterostructures and multilayer materials in a single chamber.

To date, this powerful deposition method has not been explored for synthesizing TO nanostructures. Only a few studies of growing 1D TCO nanostructures by using PLD method have been reported. In particular, Tien et al. reported PLD synthesis of SnO_2 thin films, and despite the vertically growing nanograins and irregular cross-sectional geometry, no discrete 1D nanostructures were observed.[75] Grundmann and coworkers have also succeeded in growing various 1D ZnO nanostructures[76,77] by a custom-made PLD at high pressure (25-200 mbar) and high temperature (820-950°C), all initiated on gold or other seed layers. In the high pressure and high temperature PLD approach used in these ZnO nanowire growth studies,[76,77] the high processing gas pressure reduces the mean energy of the plasma particles (i.e. closer to thermal equilibrium), while the seed layer is used to create nucleation points to initiate VS growth. For synthesizing nanostructures, a growth seed or a catalyst is required for inducing non-homogeneity in the growth process, as is often used in most of

the thermal evaporation synthesiss.[78] Gold is a common catalyst that has been used for the growth of various metal oxide nanostructures. Gold has to be kept close to its melting point of 1064°C in order to function as a catalyst to promote the VLS growth of 1D nanostructures. This temperature is difficult to achieve in typical PLD systems, unlike the high-temperature furnace used in the thermal evaporation methods. Moreover, the high deposition rate in the typical PLD systems favors the deposition of films, and modifying the target-to-substrate distance and the pressure in the deposition chamber are required in order to overcome the film formation and to effect nanostructure growth.

In Chapter 6, we report on a new catalyst-assisted PLD method, in which we use a predefined gold nanoisland template on the substrate to serve as a catalyst to promote VLS growth of various TO nanostructures. The effect of gold on the growth of TO nanostructures with different gold/substrate interfacings is presented. By modifying the deposition parameters, different growth mechanisms of VS or VLS dominate, producing different morphologies. The crystalline and morphological features of the resulting nanostructures are studied, and the effects of different deposition parameters on the growth of these nanostructures are investigated.

In Chapter 7, we focus on the growth evolution of the TO nanobelts obtained by the catalyst-assisted PLD method. These TO nanobelts not only have uniform rectangular cross-sections with the smallest dimensions ever reported to the best of our knowledge, but also grow over tens of micron making them particularly suitable candidates as (opto)-electronic components in various device applications, including field-effect transistors, optical waveguides, and chemical sensors. Studying the growth evolution of nanobelts using a mask-induced growth gradient gives us new insights into controlling the growth on different substrates and modifying their crystalline growth axis. Different gold nanoisland templates on different substrates are employed for this purpose and the effects of the crystal structure of the substrate on activating the gold catalysts and on the growth axis of the nanobelts are explored. Controlling the growth axis also gives us control of the resulting surface planes of the as-grown nanobelts, which can be used for surface science applications involving the different low-index planes of the TO and their corresponding distinct surface chemistries appropriate for chemical sensing.

In the last chapter (Chapter 8), we summarize the major results of the present study and propose some ideas for future work on TO nanostructures.

Chapter 2
Experimental Techniques

2.1 Fabrication Systems

There are two main fabrication methods that have been employed for the projects in this thesis. The first method involves spin-coating a substrate with an appropriate precursor solution, followed by post- annealing the spin-coated substrate in a tube furnace with an oxygen flow. Figure 2.1 shows the set-up that includes a Headway Research PWM32 spin-coater with programmable recipes and spinning speeds of up to 10000 rpm, and a 1200°C tube-furnace with a programmable proportional–integral–derivative (PID) temperature controller and four mass flow controllers for feeding different gases to the quartz tube in the tube furnace. Thin uniform TO films were prepared on glass and Si substrates by spin-coating an appropriate amount of a precursor solution [first in a low-speed (600 rpm) step followed by a high-speed (1800 rpm) step for even spreading] by using a programmable spinner (Headway Research PWM32). The precursor solution consisted of 0.5-2.0 M $SnCl_4 \cdot 5H_2O$ in isopropanol. Ethanol and water have also been used as the solvent, but they do not give better results than isopropanol for glass substrates. The 2×2 cm^2 glass (Corning #0211) substrates (0.2 mm thick) were cleaned by thorough washing and sonication in acetone and then isopropanol. To improve the adhesion of the coating to the glass substrate, the glass was roughened by etching in a 1 M NaOH solution for 10 minutes followed by thorough washing and sonication in isopropanol. In the case of Si substrates, the original RCA method[79] was used to produce a clean Si surface with a thin oxide layer. The spin-coated films were subsequently transferred into the quartz tube furnace and annealed for 1 h in a flowing oxygen atmosphere (with a flow rate $\geq$ 70 sccm) at 100-900°C, during which $SnCl_4$ underwent a single-replacement reaction (with O_2) to form tin oxide, SnO_x (x=1, 2). A gentle heating ramp of 10 °C min^{-1} was used in order to minimize the formation of cracks in the films.

For Eu-doping study, a clear precursor solution is prepared by dissolving $SnCl_4 \cdot 5H_2O$ salt (98% pure, Aldrich), mixed with an appropriate amount of $Eu(NO_3)_3.5H_2O$ salt (99.9% pure, Aldrich), in isopropanol alcohol by vigorous stirring for at least 2 h. The overall concentration of the salts in isopropanol is kept at 2 M, with $Eu(NO_3)_3 \cdot 5H_2O$ molar percentage of 0%, 2%, 5%, 10% and 20%, the resulting TO films of which will be referred to as SnO_2, Eu 2%, Eu 5%, Eu 10%, and Eu 20%, respectively, in the present work. The precursor solutions are then spin-coated on chemically oxidized Si(100) substrates followed by post-annealing for 90 min at 700°C in a flowing O_2

atmosphere (at a flow rate of ≥70 sccm). Two different Eu 10% films are also obtained with T_{Anneal}'s of 500°C and 900°C in order to study its effects on the photoluminescent emission by suppressing or promoting crystallization. The present procedure allows us to obtain TO films with uniform morphology and a film thickness of 150±25 nm.

The second method involves a commercial PLD system (PVD Products) used for depositing TO nanostructures. Figure 2.2 shows the PLD chamber with a base pressure better than 8×10^{-7} Torr, along with a pulsed KrF laser (248 nm) (Lambda Physik COMpex 205) operating with a pulse energy of 100-600 mJ and a repetition rate of 1-50 Hz. The laser is focused and aligned on the target by focusing lenses and reflection from a rastering mirror. The laser pulses pass through a fused silica window and enter the deposition chamber. The chamber is equipped with a multi-target carousel capable of spinning the target, which along with the rastering laser beam helps to provide uniform ablation on the surface of the target. A radiative heating assembly of infrared lamps is used to provide local heating of the substrate up to 800°C. The substrate is mounted facing down towards the target on the substrate holder with the heater assembly mounted at the backside. The substrate-to-target distance can also be varied by moving the substrate vertically with a manipulator. This system is also equipped with a four-channel mass flow controller, which in combination with a variable leak valve is used to control the pressure of the process gas. Tin (IV) oxide target is prepared by cold-pressing SnO_2 powders (Aldrich, 99.90 % purity) with a pressure of 20 MPa followed by sintering at 900°C for 24 h. Si(100) chips chemically oxidized by using a RCA cleaning method (ox-Si)[79] or H-terminated by HF etching after cleaning (H-Si), and Al_2O_3(0001)have been used as substrates for deposition To produce the catalytic seed layer, we first deposit a thin layer of gold (5-15 nm thick) on the substrate by magnetron sputtering, and gold nanoislands (GNI's), i.e. dome-shaped hemispherical gold particles, with an average size of 15-50 nm and a Gaussian size distribution are formed by post-annealing in O_2 for ox-Si and Al_2O_3(0001) substrates or in Ar for H-Si substrates, at 400-700°C, depending on the required mean size, for 1 h. To differentiate the importance of O_2 in the preparation of the GNI's and their effects on the subsequent PLD growth of TO nanostructures, we designate them as GNI/ox-Si and GNI/H-Si templates. The details of obtaining different average sizes of the GNI's (from 15-50 nm) have been discussed by Sohn et al..[80]

Using the GNI catalysts so prepared, TO nanostructures are deposited on the Si substrate, which is kept 50 mm from the target. Deposition is performed by operating the laser at a fluence of 350 mJ/pulse with a repetition rate of 5 Hz for a period of either 60 min or 90 min, while the substrate

temperature is maintained at 500, 600 or 700°C in a 400 mtorr atmosphere of Ar or O_2 (upon evacuating the chamber to the base pressure). During deposition, a natural (mask-induced) growth gradient is observed from the edge of the masked area towards the centre. Examining nanodeposits across this masked perimeter allows us to obtain information about the nanostructures at different stages of growth.

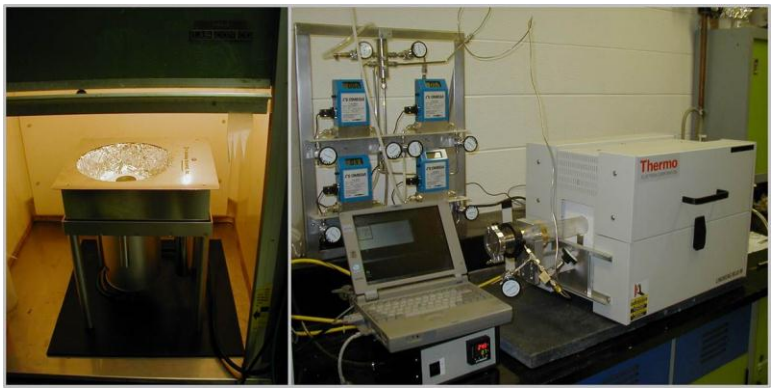

Figure 2.1 Experimental set up used for the simple spin-coating method: a Headway Research PWM32 spin-coater (left photograph) used for coating a homogeneous uniform layer of precursor solution, and a Thermo high-temperature tube-furnace equipped with a PID temperature controller and mass flow controllers used for post-annealing the film under appropriate gas flow.

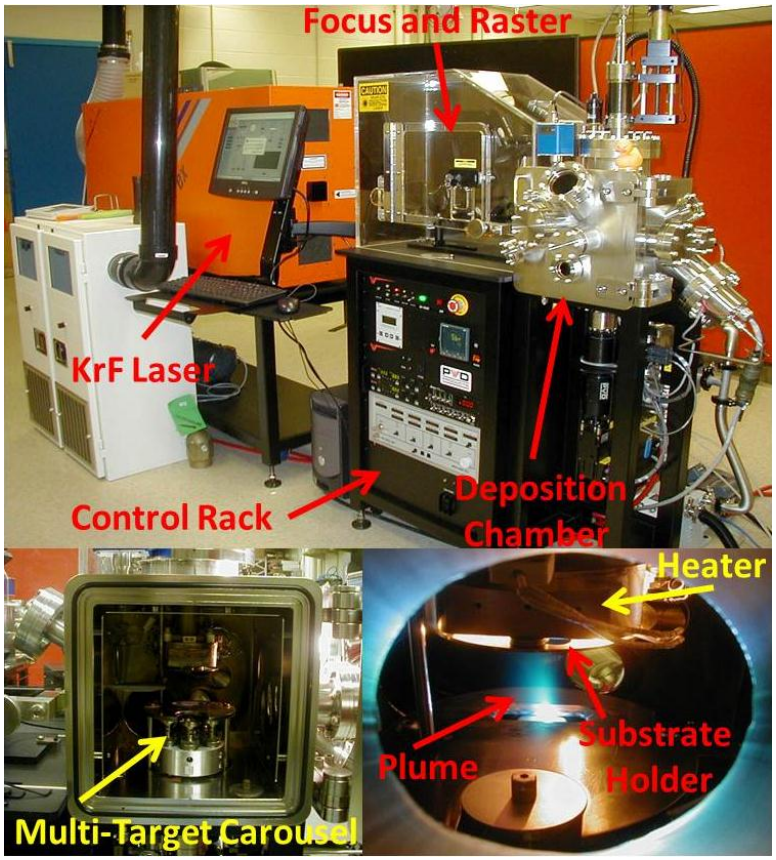

Figure 2.2 Pulsed laser deposition system (top photograph), including the laser; alignment, focus, and rastering optics; deposition chamber; and electronic control rack. The multi-target carousel and substrate mount assembly inside the chamber are shown in the bottom left photograph, and the system during the deposition depicting the ablation plume of the target is shown in the bottom right photograph.

2.2 Characterization by Scanning Electron Microscopy, Helium Ion Microscopy and Transmission Electron Microscopy

Studying the morphology and surface features is of great importance for investigating the growth mechanism, structure-property relation, and for extracting other information about the nanostructures. Scanning electron microscopy (SEM) is one of the main tools used for this purpose. An accelerated beam of electrons is focused on the sample with a typical spot size of 1 nm, and the image is obtained with an appropriate detector by scanning this fast electron beam on the sample. Images can be obtained from the low-energy scattered secondary electrons (secondary electron or SE image) or the higher-energy reflected backscattered electrons (backscattered electron image), where the former gives information on the electron density and morphology of the sample and the latter provides image

contrast based on differences in the atomic numbers of the elements in the sample. Figure 2.3 shows the LEO FESEM 1530 microscope, equipped with a field-emission source and an acceleration voltage up to 25 kV, used for the present work. This microscope has In-Lens and out-of-lens SE detectors for secondary electron imaging, and a Centaurus detector (manufactured by K.E. Developments Ltd.) for backscattered electron imaging. Moreover, it includes a EDAX energy-dispersive x-ray analysis system, which provides elemental identification based on detection of X-ray emission photon energies from the sample upon excitation by the highly energetic electron beam. The X-ray spectra so obtained can also be used for quantifying the composition of the sample through the intensities of their characteristic X-ray emission. The SEM system also contains various other detectors including a cathode-luminescence detector and a STEM detector, which have not been extensively used in the present work.

Helium ion microscope (HIM) is another microscopic tool that is used in the thesis. This new generation of microscopes is based on the use of a high-energy He ion beam instead of an electron beam to generate secondary electrons upon high-energy ion impact with the sample. The physics behind the operation and optics involved in this microscope are very similar to the SEM, where the negative charge of the electrons is replaced by the positive charge of the ionized Helium ions. There are some clear advantages of using He ions instead of electrons:[81]

1. He ions are heavier than electrons, and they will not be diffracted as much compared to electrons due to reduction in the de Broglie wavelength, making it possible to obtain a sub-nanometer probe size with smaller apertures.
2. The interaction volume of the He ions is also smaller and less diffused on the surface compared to electrons, giving rise to a better resolution in combination with a smaller probe size.
3. In addition to the increase in the resolution, the use of smaller apertures to obtain smaller probe sizes has another advantage because the depth-of-field obtained by HIM are much larger than that obtained by SEM. The increased depth-of-field is of great importance to imaging one-dimensional nanostructures with micron-sized height differences.

Figure 2.4 shows the Zeiss ORION Plus HIM used for this present work. Introduction of a He gas at very low flow rates (increasing the pressure from 10^{-9} to 10^{-7} Torr) leads to formation of an intense He^{+} ions upon field ionization at a high positive bias (~ 25 kV) of a cryogenically cooled atomically sharp tip. Upon appropriate in-situ construction of the emitter tip, a trimer of the tip material (W) is

obtained, and the He ions created at one of the three atoms in the trimer are accelerated and focused through the ion optics column. The focused He^+ beam is then directed and scanned across the sample, producing secondary electrons. These secondary electrons are detected using an Everhart-Thornley (ET) detector, while the Rutherford backscattered ions are detected using a microchannel plate (MCP) detector. Similar to the electron beam detectors in the SEM, the ET imaging provides both the morphology and the electron density information, while the backscattered ion imaging offers image contrast based on the atomic number of the elements.

Transmission Electron Microscopy (TEM) measurements are performed using a JOEL 2010F operated at 200 kV. It has been used for studying the crystal structure, phase determination, and identification of the surface planes of the individual nanostructures. Unlike the aforementioned microscopic studies that are carried out by myself, these measurements are done by the operator, Fred Pearson, at the Canadian Centre for Electron Microscopy located at McMaster University (Hamilton, Ontario). Samples are usually scraped off the substrates and dispersed in methanol, and the resulted solution is dispensed onto holey carbon grids after sonication for 10 min.

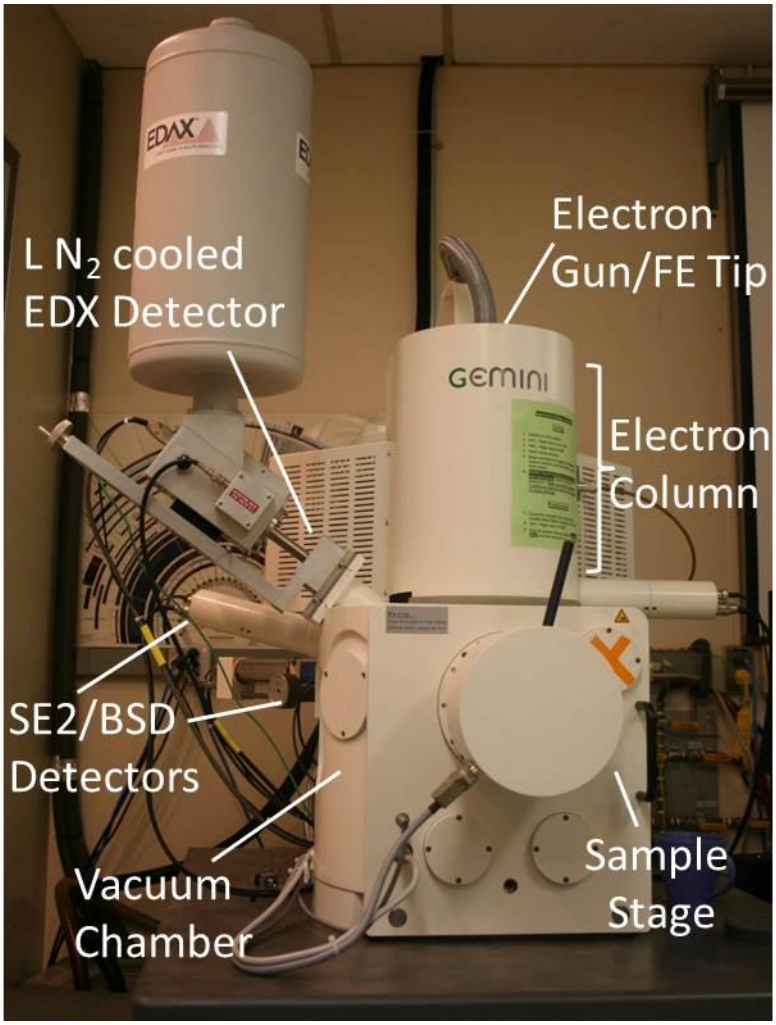

Figure 2.3 Photograph of the LEO FESEM 1530 field-emission scanning electron microscope (SEM), equipped with secondary electron In-Lens and out-of-lens (SE2) detectors, and backscattered electron detector (BSD) and an EDAX energy-dispersive X-ray analysis system.

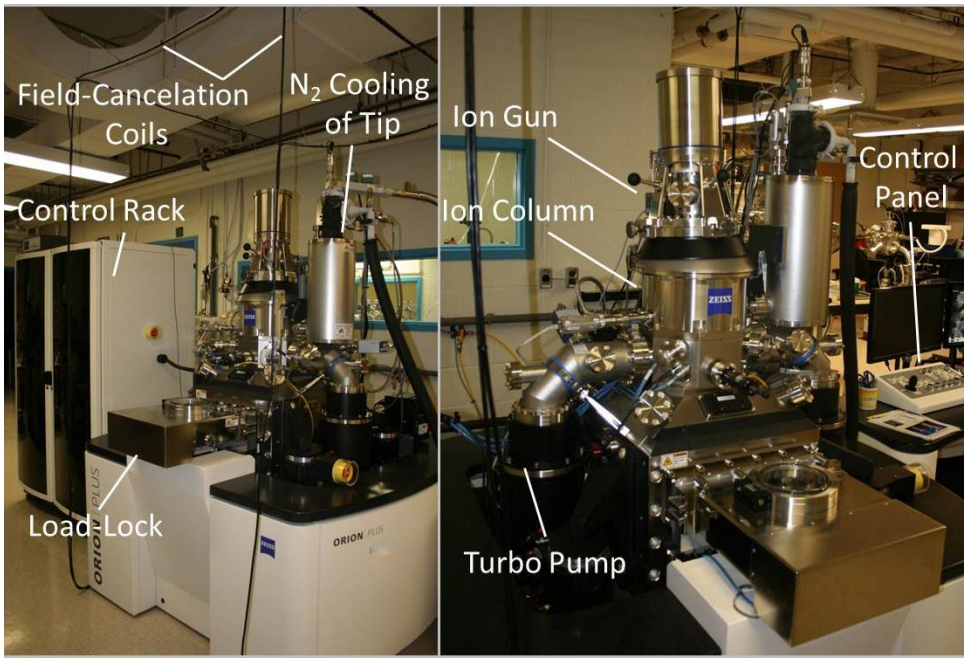

Figure 2.4 Photograph of the Zeiss Orion Plus helium ion microscope (HIM) Left: The control, data acquisition, and field-isolation electronics of the microscope, and Right: A closer look at the ion-column and the sample chamber equipped with secondary electron and backscattered ion detectors.

2.3 X-ray Diffraction

Figure 2.5 shows a Panalytical X'pert Pro MRD X-ray diffractometer used for determining the average crystalline structure of the TO nanostructures. There are different optics and diffraction geometries available for this system. Due to the very small amount of sample and the small sizes of the crystallites, the signal strength from these nanostructures is usually very weak and dominated by the signal from the substrate. In order to increase the signal, glancing incidence X-ray diffraction (GIXRD) technique is used for examining the crystal structure of the nanostructures. For all the TO nanostructures discussed in this thesis, GIXRD is used to identify the crystalline phase and crystallite sizes, and the preferred growth directions in the case of the one-dimensional TO nanostructures. In this GIXRD method, the incidence angle (ω) of the X-ray beam is kept at a very shallow angle (close to the critical angle of the sample) while the detector is swept over the 2θ angle. Since the incidence angle is below the critical angle, an evanescent wave is formed. This evanescent wave only penetrates into a thin layer (less than 100 nm) and travels on the surface of the sample, leading to an

increased interaction of the X-ray beam with the nanostructured layer on the surface of the substrate.[82,83] The intensity of the signal from the surface layer containing the nanostructures of interest therefore increases significantly. For this purpose, a parallel beam geometry with an X-ray mirror in the incident beam side and a parallel-plate collimator in the diffracted beam side is used. This configuration allows GIXRD measurements at a typical incidence angle of 0.3°, used for most samples. It should be noted that an instrumental broadening of 0.4° in the FWHM of peaks is observed and corrected for in the Scherrer analysis. This broadening is measured on the main peak of a stress-free W standard sample in the optics setup that is used later on for measuring the XRD pattern of nanocrystalline peaks. The Scherrer formula used for calculating the crystallite size is given by:

$$\text{Crystallite size (average value)} = \frac{K \times \lambda}{(B_{Observed} - B_{Instrument}) \times Cos(\theta)},$$

where K is the shape factor of the nanocrystallites, λ is the wavelength of the X-ray used for obtaining the diffraction pattern, θ is the peak position, $B_{Observed}$ is the broadening (FWHM) in the most intense XRD peak of the sample, and $B_{Instrument}$ is the peak broadening observed for the standard stress-free sample, which is due to the instrumental effects and for the X-ray optics used in our GIXRD system we observe $B_{Instrument}$=0.40° (= 0.0022 rad).[82]

For the highly crystalline, one-dimensional TO nanostructures, symmetric 2θ-ω scans are also conducted. This geometry provides information on the crystalline orientation of the entire TO nanostructures in the surface-normal direction, in contrast to just the surface layer sampled in GIXRD.

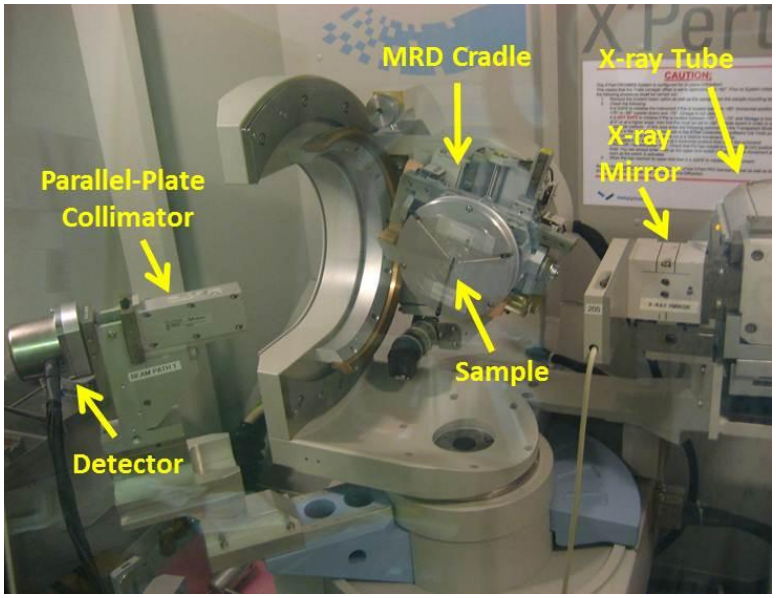

Figure 2.5 Photograph of the Panalytical X'pert Pro MRD X-ray diffractometer used for crystal structure characterization of the TO nanostructures, in the parallel beam geometry with an X-ray mirror and a parallel plate collimator used for the incident and diffracted beam optics, respectively.

2.4 X-ray Photoelectron Spectroscopy

X-ray photoelectron spectroscopy is also performed on pure and doped nanocrystalline TO films in order to examine their chemical states and corresponding compositions. Such information is particularly important to assure the completion of the reaction in the post-annealing step and to determine the oxidation state of the elements in the film. The instrument used for these measurements is a Thermo-VG Scientific ESCALab 250 Microprobe (shown in Figure 2.6), equipped with a monochromatic Al Kα X-ray source (1486.6 eV) operated at a typical energy resolution of 0.4-0.5 eV full-width-at-half-maximum. The photoejected electrons from the atomic core-levels or the valence band of the material as a result of monochromated X-ray illumination are produced from the very top surface layer of the sample (depth < 10 nm). The kinetic energy of these photoelectrons is analyzed by using a hemispherical analyzer, and can be used to determine the corresponding binding energy (given a known incident X-ray photon energy) using the Einstein equation.[84] When compared with the appropriate standards, the binding energy contains chemical shift information about the local chemical environments. This system is also equipped with an Ar sputtering system for depth-profiling experiments.

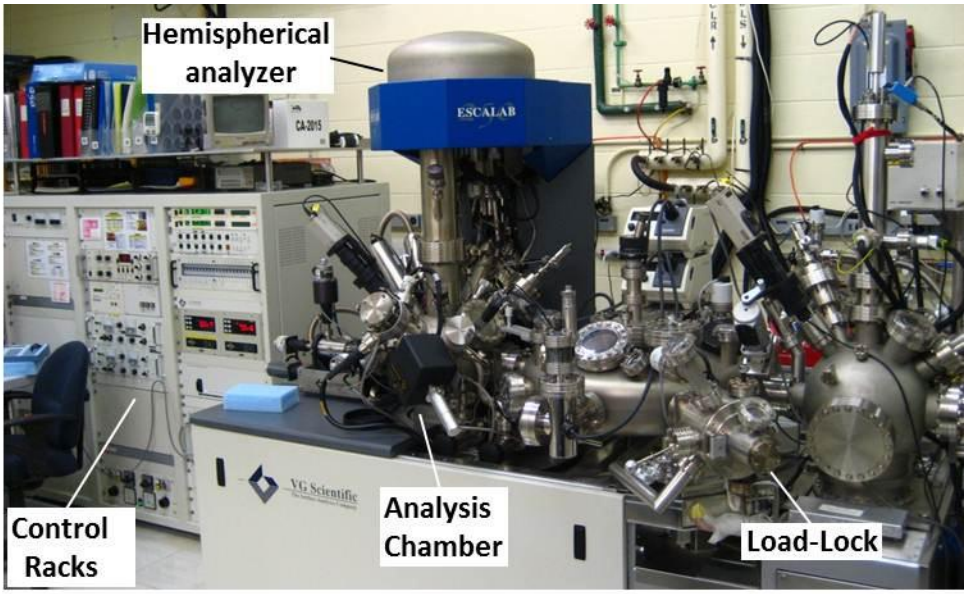

Figure 2.6 Photograph of the Thermo-VG Scientific ESCALab 250 Microprobe used chemical analysis of the TO nanostructures.

2.5 Electrical, Optical and Magnetic Property Measurements

Figure 2.7 shows a home-built system used for measuring the ac and dc resistivity of the TO films in the 30-300 K temperature range. A lock-in amplifier is used to generate a constant AC current of 100 nA by applying 1 V at 1 Hz on a 10 MΩ resistor, and to measure the output voltage signal. A He cryopump is used for cooling the cold head in a vacuum housing with a base pressure of 10^{-5} Torr. The sample is mounted on the cold head mechanically by two clamps, along with a thermally conductive gel to ensure good thermal contact. The temperature is measured by using a Si diode sensor buried in the cold head. A home-made constant current dc power supply capable of delivering currents in the 1 μA to 10 mA range is also used to confirm the ac measurement results. All the data is acquired by using an analogue-to-digital converter and is stored in a computer using a Visual Basics program developed in house (by Fernando Rios). The ac conductivity of the nanocrystalline films is measured as a function of temperature by a four-point probe method. With the TO film covering the entire substrate (20×20 mm^2), four gold strips (each 0.8 mm wide) are deposited as voltage/current contacts 2 mm apart on the TO film, and they are connected to the measurement wires using silver paste. After curing the silver paste by illumination under an incandescent light for 12 hours, the sample is then transferred to a cryopump station and evacuated to an initial vacuum of 1×10^{-5} mbar. To decrease the amount of adsorbed gases on the surface in order to reduce their effect

on the resistivity, as known to occur for TO films,[85] and to recover the conduction channels, all the samples are retained in vacuum for at least 24 h before measurement. The ac results are also compared with dc resistivity data taken at 1 μA with a monitored constant current source in order to assure the reproducibility of the observed temperature behavior of the ac resistivity.

In order to measure the optical transparency and band-gap of the TO films, UV-Visible transmission and reflectance spectra are collected for transparent and opaque substrates, respectively, by using a Perkin-Elmer Lambda 35 UV-Vis spectrometer equipped with a Labsphere integrating sphere. The photoluminescence properties of the Eu-doped samples are also investigated using a Perkin-Elmer LS-55 fluorescence spectrometer at room temperature.

The total magnetic moment of the Eu-doped samples are measured by using a Quantum Design Superconducting Quantum Interference Device (SQUID) magnetometer. The magnetic moments of the samples are measured as a function of temperature in the 4-300 K range with the sensitivity of 2×10^{-6} emu. These measurements are performed by Dr. Mangala Singh in Professor Fereidoon Razavi's laboratory in the Physics Department, Brock University.

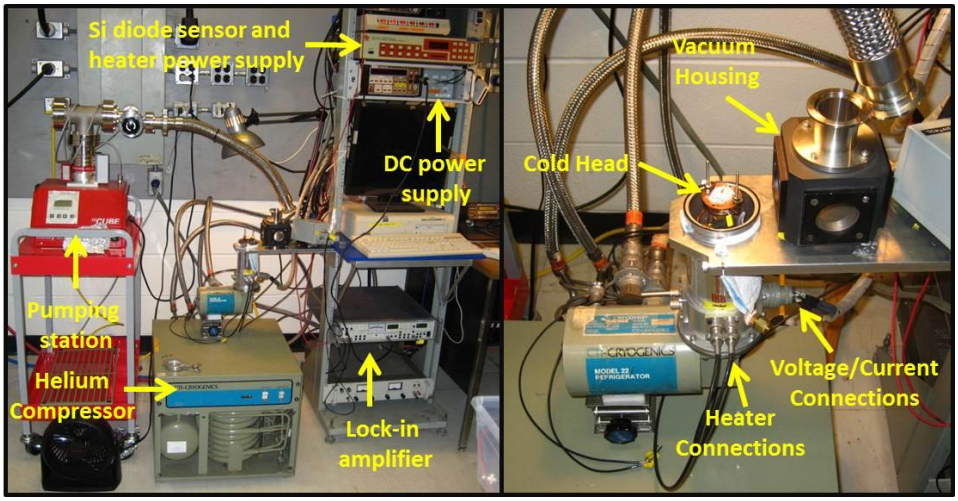

Figure 2.7 Left image: Photograph of the home-built resistivity set-up used for measuring ac and dc resistivity of the TO films with a lock-in amplifier and Keithley digital multimeters, in the temperature range of 30-300 K facilitated by a He cryopump. Right image: Photograph of the cold head and the vacuum housing with a Quick Flange as connection to a turbopump station.

Chapter 3
Controlled Growth of Monodisperse Nanocrystallites in SnO_2 films[******]

In this chapter, preparation of continuous, smooth, granular TO films on glass and Si substrates is demonstrated using a simple, easily scalable spin-coating procedure followed by annealing in oxygen, the details of which are described in Chapter 2 in the fabrication systems section. Extensive characterization is also performed in order to explore the relationship of the morphology, crystallinity, and nanocrystallite size and distribution to the chemical composition and defects of the films. [It should be noted that the experimental measurements, data analysis, and preparation of the manuscript, from which this chapter is extracted, are all performed by the author of this thesis. I would like to acknowledge the role of co-authors, Nina F. Heinig, Debabrata Pradhan and Kam Tong Leung, in the training of the use and operation of the different instruments and in the valuable discussions that we had on analyzing the data and in revising the manuscript. It is with their permission that I have included this article in my thesis.]

3.1 Surface Morphology and Roughness

SEM studies have been performed on all the films, of which minor charging was observed for those prepared with a post-anneal temperature below 350°C, reflecting their non-conducting nature. Subsequent EDX studies on these non-conducting films (obtained with a post-annealing temperature of 120-300°C) revealed no detectable chlorine signal in the samples, which indicates the completion of the oxygen replacement reaction. It is important to note that the oxygen flow plays an essential role in this replacement reaction, because it drives the reaction toward completion even at a post-anneal temperature as low as 120°C. If the annealing was performed without oxygen flow, evaporation of the solvent would occur, causing recrystallization of stannic chloride salt appearing as a white powder on the glass surface. For the spin-coated film obtained with a 2 M [$SnCl_4$] solution and post-annealing at 450°C, continuous uniform deposition on the glass substrate was observed (Figure 3.1a). As is commonly found in a spin-coating process, a minor material build-up was noted near the edges of the substrate due to surface tension. The crack formation that has often been

[******] Reproduced with permission from [Cryst. Growth Des., 2011, 11 (1), pp 247–255 DOI: 10.1021/cg1011814, http://dx.doi.org/10.1021/cg1011814] Copyright @ 2010 American Chemical Society.

reported in sol-gel coated films[19,34] can be minimized by optimizing the initial annealing rate. Close examination at a higher magnification of the sample post-annealed at 400°C reveals the granular morphology of the film with grain sizes below 50 nm (Figure 3.1b). Similar morphologies have also been obtained for films post-annealed at 350°C, 450°C, and 500°C (not shown). As shown in the cross-sectional SEM image (inset of Figure 3.1b, and further confirmed by low resolution TEM images in Figure 3.3 below), grains are also found throughout the thickness of the film, similar to that observed for the surface. For a spin speed of 1000-1800 rpm and duration of 5-10 minutes, the concentration of the precursor solution, [$SnCl_4$], used in the spin-coating process is found to play an important role in controlling the thickness of the resulting TO films (after post-annealing). The film thickness can be varied from 130 nm using a 0.5 M solution to 218 nm using a 2.0 M solution, the latter of which is illustrated in the cross-sectional SEM image of the sample post-annealed at 400°C (inset of Figure 3.1b). Repeating the spin-coating and post-annealing cycle in successive steps can be used to create thicker films, with the film thickness reproducible to within 30 nm.

Figure 3.1 also shows AFM images of the glass substrate with (Figure 3.1c) and without etching (Figure 3.1c, inset), and of the TO films as-deposited and upon post-annealing at different temperatures on the etched glass substrates (Figures 3.1d-i). Table 3.1 summarizes the corresponding root-mean-square (rms) surface roughness of these samples over a fixed scan area of 1 μm^2. As expected, the surface roughness of the etched glass (Figure 3.1c), with a rms value of 0.4 nm, is considerably larger than that of the non-etched glass (Figure 3.1c, inset), with a rms value of 0.2 nm. The rms roughness of the deposited films is found to increase with increasing post-anneal temperature, from 0.9 nm over 1 μm^2 at 250°C to 2.2 nm over 1 μm^2 at 500°C on the etched glass substrate, and to 6.6 nm over 1 μm^2 at 600°C on Si substrate (Table 3.1). Small round grains are found to emerge on the surface of the film prepared with a post-anneal at 350°C (Figure 3.1f), suggesting the onset of a structural evolution at this temperature. Raising the post-anneal temperature to 400, 450 and 500°C increases the granularity of the film, with a concomitant increase in the size of these grains (Figures 3.1g-i) and in the rms roughness (Table 3.1). It should be noted that the rms roughness values of the films synthesized below 500°C by the present method are among the smallest when compared to those of films prepared by other methods, e.g. electron beam evaporation[86] and spray pyrolysis,[62,87] making the present procedure not only a facile and cost-effective but also a superior method for device fabrication. Furthermore, the apparent granular structure appears homogenous over the entire sample. This granularity along with the pores observed in the cross-

sectional SEM image (inset of Figure 3.1b, and further shown in low-resolution TEM images in Figure 3.4 below) helps to increase the surface area of the film.

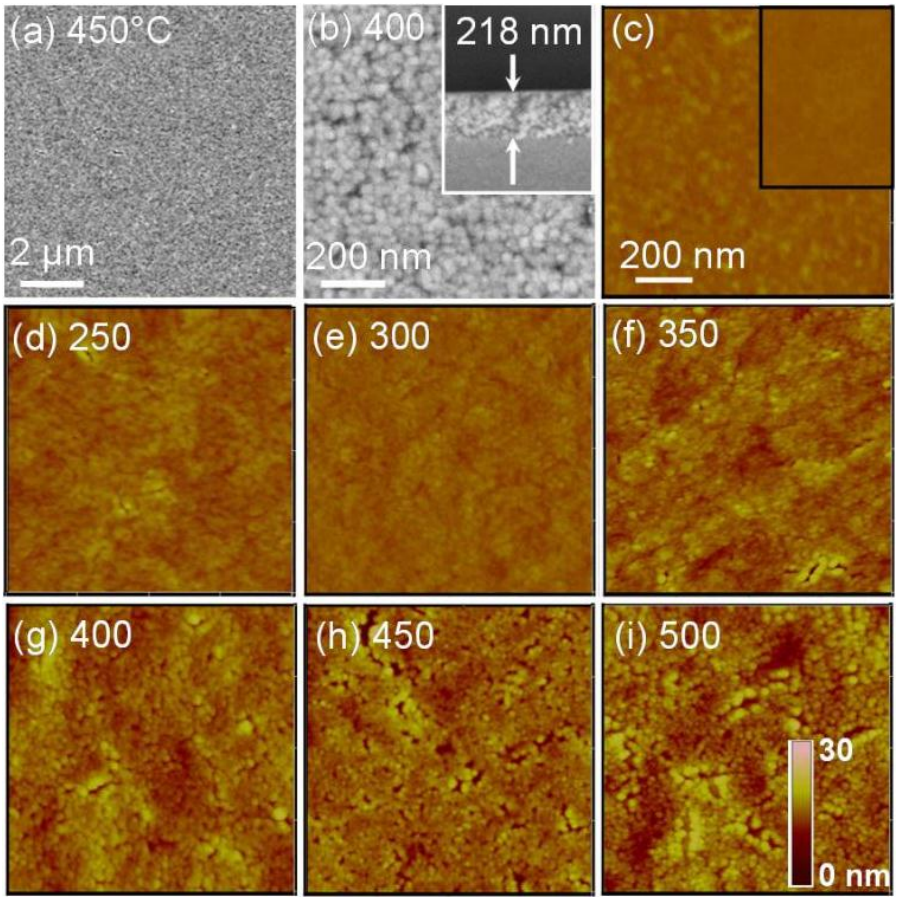

Figure 3.1 SEM images of tin oxide films prepared with a post-oxygen-anneal at (a) 450°C and (b) 400°C (with a cross-sectional image of the film shown in inset). AFM images of (c) glass substrate with and without etching (inset) and (d-i) tin oxide films prepared with post-oxygen-annealing at different temperatures. Roughness (height) scale and scale bar are the same for all the AFM images.

3.2 Crystal Structure

Figure 3.2 compares the GIXRD patterns of the deposited films (spin-coated with a 2 M [$SnCl_4$] solution) post-annealed for 1 hour at different temperatures. For the films obtained with a post-anneal temperature below 350°C, diffraction patterns with broad features are observed, indicating an amorphous film structure (Figure 3.2). On the other hand, the films obtained with a post-anneal temperature at or above 350°C exhibit prominent diffraction peaks, the peak positions and relative

intensities of which are in excellent accord with the reference tetragonal SnO_2 profile (ICDD PDF# 00-041-1445). This indicates that the onset of crystallization occurs near 350°C. The peak observed at 2θ=56.12° for the sample post-annealed at 600°C and the weak shoulder at 2θ=51.12° correspond to diffraction features of the Si(100) substrate. The peak intensities of the TO film obtained at 400°C are found to be considerably higher than those at 350°C, while a post-anneal temperature in the range of 400-500°C does not significantly increase the respective intensities. Applying the Scherrer analysis to the strongest, (110), diffraction peak of the films by applying the instrument broadening of 0.40° and a spherical k factor of 0.9 as SEM results suggest a spherical shape, enables us to estimate the corresponding average crystalline grain sizes. As shown in Table 3.1, the average crystalline grain size is found to increase from 3.8 nm at 350°C to 4.8 nm at 500°C on the glass substrates. The growth trend has also been studied at higher temperatures by preparing TO films on Si substrates with post-annealing at 600, 700 and 900°C. It should be noted that deposition below 600°C has also been performed on Si substrate and the resulting films are found to exhibit similar morphology and properties to those prepared on glass substrates. This similarity is likely due to the existing native oxide layer (~10nm thick) on the Si substrates (as a result of the RCA cleaning method). The corresponding XRD patterns (Figure 3.2) show an increase in the peak intensities along with a notable decrease in the peak width. Scherrer analysis further indicates a considerable increase in the average nanocrystallite size to 7.6, 11.3 and 25.5 nm with the respective increasing post-anneal temperature (Table 3.1).

The observed trends in the intensities of the diffraction peaks and the average nanocrystallite sizes with increasing post-anneal temperature suggest a two-step growth mechanism with onsets at 350°C and 500°C. Depending on the synthesis methods, there are different reports about the onset temperature of crystallization for SnO_2. In particular, Shukla et al.[34] annealed a dip-coated film at 600°C to create nanocrystallites in the layer (as shown in their TEM images), while Jin et al.[20] obtained crystalline samples upon annealing a spin-coated tin oxide gel at 400°C. Chang et al.[25] reported the formation of a crystalline phase in electrodeposited films, which they subsequently annealed at 400°C for 4 h in order to increase the crystallinity of the samples. The presently observed crystallization onset at 350°C is therefore in good accord with these earlier studies. Above the onset of nanocrystallite formation at 350°C, a minor increase in the post-anneal temperature, e.g. 400°C, dramatically increases the amount of crystalline material. Further increase of the post-anneal temperature to 450°C and 500°C, however, does not significantly change the amount of crystalline

material. In order to determine whether the conversion of amorphous to crystalline TO is complete, we compare the XRD patterns of a TO film prepared on a Si substrate, in a separate experiment, with post-annealing at 400°C before and after a second post-anneal at 900°C (Figure 3.3a). The apparent increase in the peak area of the (110) diffraction peak after the second anneal at a higher temperature (900°C) indicates that a substantial amount of amorphous phase remains in the TO films obtained with a post-anneal at 400-500°C (Figure 3.3a). However, further annealing a sample obtained by post-annealing at 400°C (for 1 h) for extended time periods (24 and 96 h) at the same post-anneal temperature (400°C) produces essentially unchanged XRD patterns, i.e. without any discernible changes in the peak intensity and width (Appendix A.1). These experiments show that although the amorphous-to-crystalline conversion in this temperature range (400-500°C) is incomplete, no further detectable nucleation and nanocrystallite growth occur with prolonged annealing at the same temperature. This indicates the heterogeneous nature of nucleation within the amorphous TO phase and that the resulting nanocrystallites in the amorphous matrix are restrained from further growth. The nanocrystallite size also exhibits a very slow increase with increasing post-anneal temperature from 3.8 nm at 350°C to 4.4-4.8 nm at 400-500°C (inset of Figure 3.2). However, increasing the post-anneal temperature to 600, 700, and 900°C leads to an exponential increase in the nanocrystallite size, along with a concomitant decrease in the amount of amorphous phase, indicating a new growth mechanism above 500°C. We hypothesize that the change in density near the nucleation sites during the conversion of amorphous phase to crystalline phase creates strain, which in turn limits the nanocrystallite growth to less than 5 nm in size below the second onset temperature (500°C). Above 500°C, sufficient energy is available to overcome the barrier in this "strain-limited" growth step, and the subsequent growth step follows the Arrhenius-like (exponential) trend.

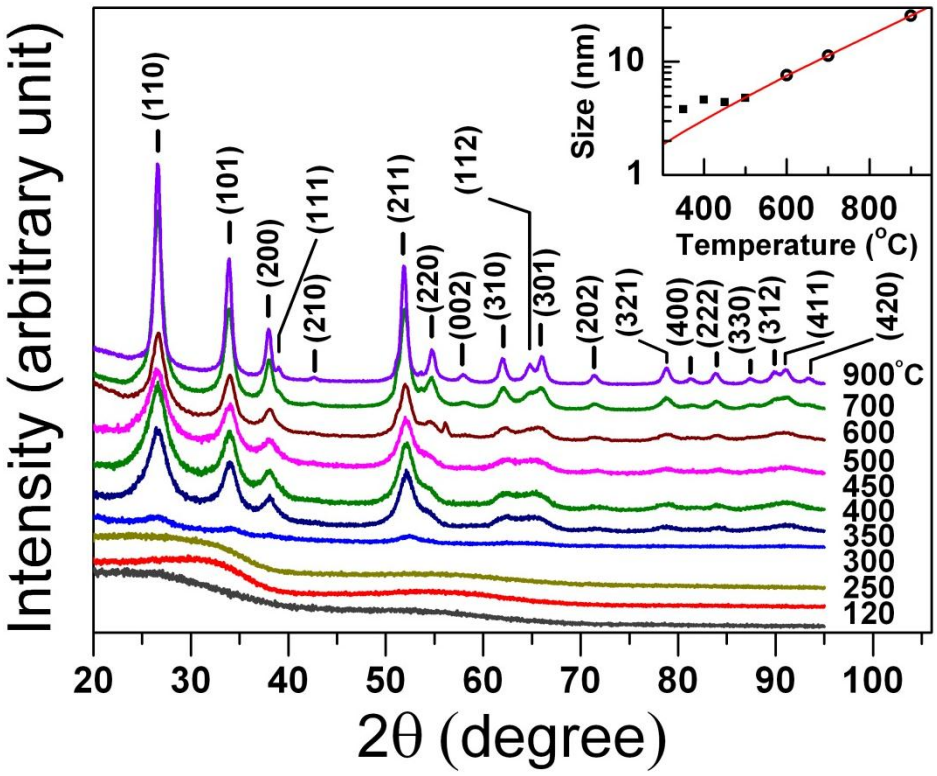

Figure 3.2 Glancing-incidence XRD patterns of tin oxide films prepared with different post-oxygen-anneal temperatures with peak assignments in accord with the SnO2 reference pattern (ICDD PDF# 00-041-1445). The patterns are shown on a linear scale and have been offset for clarity. Inset shows the change in the nanocrystallite size, deduced by Scherrer analysis based on the (110) peak width, with increasing post-anneal temperature. The straight line in the inset corresponds to an exponential fit to the data on the high temperature side (500-900°C). The films obtained at 600, 700 and 900°C are prepared on Si substrates while the rest obtained at a lower post-anneal temperature are prepared on glass substrates.

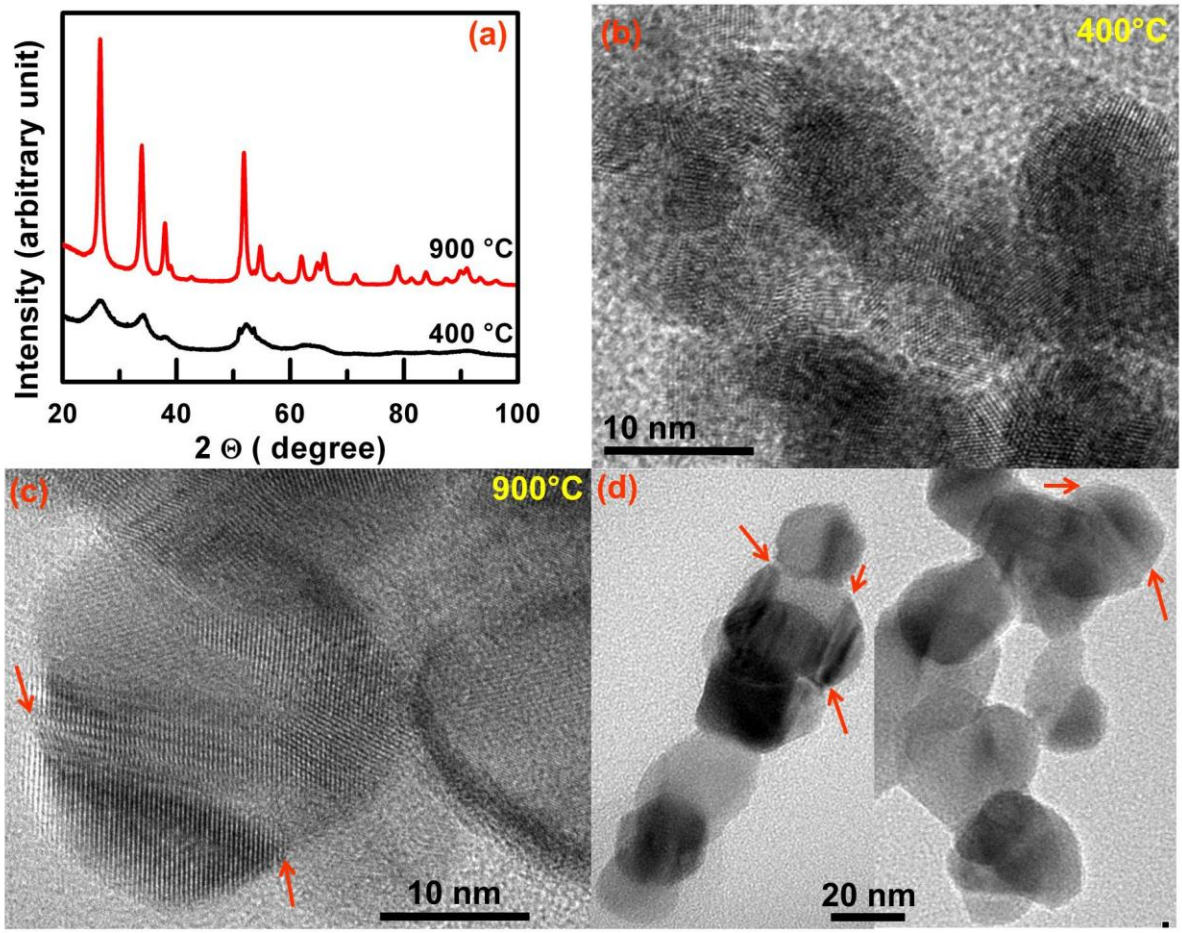

Figure 3.3 (a) Glancing incidence XRD profiles and (b, c, d) TEM images of a tin oxide film prepared on a Si substrate with post-oxygen anneal at 400°C (a, b), followed by a second anneal of the same film at 900°C (a, c, d).

Figure 3.4 shows the bright-field TEM images of the TO films obtained on the glass substrates with different post-anneal temperatures. The TEM images have been obtained from different parts of the film to assure a general sampling of the entire film. Evidently, the size distributions of the nanocrystallites obtained over the post-anneal temperature range (350-500°C) for the present TEM study appear to be quite narrow (typically ±1.5 nm). The as-grown grains are generally found to be spherical, with a diameter smaller than 10 nm. This granular structure also leads to formation of pores throughout the film thickness. This is consistent with the observed spherical grain morphology and the increasing trend in the surface roughness of the films with increasing post-anneal temperature, as observed in the respective SEM and AFM images (Figure 3.1). The average sizes of these crystalline grains are estimated from the high-resolution TEM images (Figure 3.4, right) by fitting

circles or ellipses around the crystallites, and they are summarized in Table 3.1. The average grain size is found to increase from 6.6 nm at 350°C to 8.7-9.7 nm in the 400-500°C range. The present TEM analysis gives a similar trend of increasing crystallite size with increasing post-anneal temperature, but with larger nanocrystallite sizes than those given by the XRD Scherrer analysis. Given that peak broadening in XRD is due to both crystallite size and local defects and strain in the nanocrystallites, Scherrer analysis will give smaller grain sizes for nanocrystalline films with more crystalline defects. The discernibly larger grain sizes extracted from the TEM images than those obtained from the XRD patterns therefore suggest the presence of a considerable amount of defects in the nanocrystallites.

The lattice spacings are also measured from the high-resolution TEM images shown for the samples obtained with post-anneal temperatures of 350°C and 450°C (insets of Figure 3.4b and 3.4f). The corresponding lattice spacings of 2.64 Å and 3.37 Å are well matched to the respective lattice spacings of the (101) plane (2.6427 Å) and (110) plane (3.347 Å) of the reference bulk tetragonal SnO_2 (ICDD PDF# 00-041-1445). These two lattice spacings are the largest found in the SnO_2 structure, making them the easiest to identify in the TEM images. Careful inspection of the lattice spacings indicates that within a single grain, the lattice spacings may vary around an average value, indicating the presence of crystalline defects, such as vacancies, dislocations, and local strains. The high-resolution images therefore support our conclusion that the observed larger average crystalline grain size than those deduced by Scherrer XRD analysis is largely due to the presence of crystalline defects. Closer examination of the high-resolution images reveals the presence of a large density of point and line defects in the observed crystallites, which is particularly evident in the sample post-annealed at 350°C (Figure 3.4b). The observed crystallites for the samples prepared at temperatures below 500°C have less distinct boundaries, and in spite of the large number of defects, appear to exhibit a single crystalline orientation individually (Figures 3.3, 3.4). However, for the sample post-annealed at 900°C, there are individual crystallites with different crystalline orientations (Figure 3.3c,d). Evidently, the regions with different orientations are separated by contrasting fringes (marked by arrows), which show the change in the crystal orientation and the stress and defect lines in their boundary. Moreover, the distorted shape of the crystallite, together with the observed different crystal orientations at which distortions are observed, clearly show that fusion of crystallites with different initial crystalline orientations could be a plausible mechanism for grain growth at a higher temperature.

For the samples obtained with post-anneal temperatures of 350°C (Figure 3.4a) and 450°C (Figure 3.4e), distinct diffraction rings originating from different planes found in the respective selected area electron diffraction patterns further indicate the polycrystalline nature of the SnO_2 phase in the sample. The bright rings at the center of the respective patterns correspond to the (110) and (101) planes, while the (211) ring is also visible in both patterns. Similar diffraction patterns exhibiting the (110), (101), and (211) planes have also been reported by Chang et al.[25] and Chen et al.[88] Additional weak (310) and (112) rings are also observed for the samples post-annealed at 350°C and 450°C, respectively. The observed diffraction rings indicate the presence of only polycrystalline phase of SnO_2, without a discernible amount of crystalline SnO or metallic Sn, in good accord with the GIXRD results.

Table 3-1 Root-mean-square (RMS) surface roughness over 1 μm^2 area measured by AFM, full width at half maximum (FWHM) of the (110) peak and the corresponding crystallite sizes estimated by the Scherrer analysis, and compared to those obtained from TEM data, for the pristine and etched glass substrate and for tin oxide samples prepared with different post-oxygen-anneal temperatures on etched glass substrates (250-500°C) and Si substrates (600, 700, 900°C).

Samples	RMS Roughness (nm)	FWHM of the (110) Peak (°)	Crystallite Size from XRD (nm)	Crystallite Size from TEM (nm)
Glass Substrate	0.2 ± 0.1	NA	NA	NA
Etched Glass Substrate	0.4 ± 0.1	NA	NA	NA
250°C	0.9 ± 0.1	NA	NA	NA
300°C	0.7 ± 0.1	NA	NA	NA
350°C	1.6 ± 0.3	2.55 ± 0.01	3.8	6.6 ± 1.0
400°C	1.7 ± 0.3	2.14 ± 0.01	4.6	8.7 ± 1.6
450°C	2.2 ± 0.3	2.24 ± 0.01	4.4	9.4 ± 1.4
500°C	2.2 ± 0.3	2.08 ± 0.01	4.8	9.7 ± 1.5
600°C	6.6 ± 2.0	1.47 ± 0.01	7.6	NA
700°C	NA	1.12 ± 0.01	11.3	NA
900°C	NA	0.72 ± 0.01	25.5	30 ± 9.9

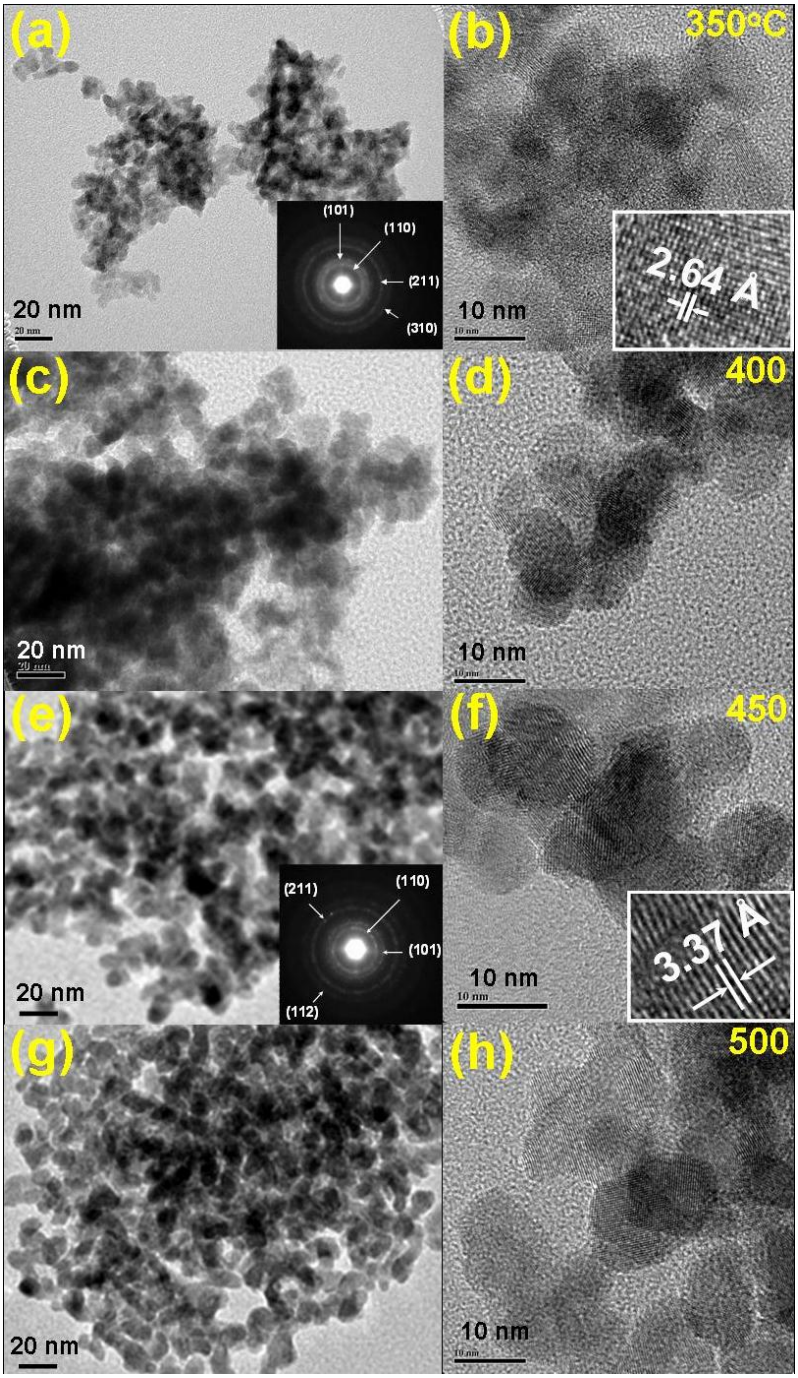

Figure 3.4 TEM images of the tin oxide films prepared on glass substrates with post-oxygen-annealing at (a, b) 350°C , (c, d) 400°C, (e, f) 450°C and (g, h) 500°C. Insets show the respective magnified areas of the images, with the lattice planes and their spacings (b, f), and selected area electron diffraction patterns, with the crystalline planes identified for individual rings (a, e) for samples prepared with post-annealing at 350°C and 450°C.

3.3 Composition and Chemical State

Our X-ray diffraction data indicates that there are significant amounts of both crystalline and amorphous phases present in the TO film obtained with post-annealing at 400°C (on a glass substrate). Unlike the films obtained at a higher post-anneal temperature of 600-900°C (on a Si substrate), this granular film contains monodisperse nanocrystallites with sizes below 10 nm, which are of potential interest to new applications and are especially desirable for gas-sensing applications. This film also represents the type of stable TO films with similar structural and composition characteristics that can be obtained on a transparent, low-heat resistant substrate like glass in this temperature range (400-500°C). We therefore conduct further composition analysis of this film by depth-profiling XPS. The survey spectrum of the film (Appendix A.2) shows prominent Sn and O features, with no discernible intensity for Cl features, confirming the completion of the replacement reaction.

Figure 3.5a shows the XPS spectra of the Sn $3d_{5/2}$ and O 1s regions at different sputtering times for the TO film obtained with post-annealing at 400°C (Figures 3.1b, 3.1g). The Sn $3d_{5/2}$ peak at 487.4 eV for the as-prepared film starts to shift to a lower binding energy after 60 s of sputtering, and settles at 487.0 eV for longer sputtering times (>120 s). This minor shift towards a lower binding energy is also observed for the O 1s peak, from 531.3 eV for the as-prepared film to 530.8 eV upon sputtering for >120 s. These binding energy shifts in the Sn $3d_{5/2}$ and O 1s peaks may be due to surface charging caused by the presence of a carbonaceous layer as a result of sample handling in air. A closer examination of the spectra (Figure 3.5a) reveals the presence of a high-energy tail of the O 1s peak, which has been attributed to "chemisorbed oxygen" on the surface by Szuber et al.[89] in their XPS study of the surface treatment of SnO_2. To assign the Sn $3d_{5/2}$ features, we have measured the XPS spectra of SnO_2 and SnO powders (Aldrich, 99.9% and 99% purity, respectively) as reference, which, after sputtering for 200 s to remove the carbonaceous layers, exhibit Sn $3d_{5/2}$ binding energies of 487.0 eV and 486.6 eV respectively. In accord with these reference spectra (Appendix A.3), we assign the observed Sn $3d_{5/2}$ peak at 487.0 eV to Sn^{4+} (in SnO_2). This assignment is also consistent with the reported binding energy values for tin oxide synthesized by different procedures,[90-92] all found with an energy difference of less than 1 eV between the Sn^{4+} and Sn^{2+} states.

In Figure 3.5, we also plot, as a function of sputtering time, the relative peak intensities of Sn $3d_{5/2}$ (at 487.0 eV) and O 1s (at 530.8 eV), as well as the corresponding O-to-Sn ratio obtained after appropriate correction by the respective sensitivity factors (4.725 for Sn $3d_{5/2}$ and 0.711 for O 1s[84]).

The presence of chemisorbed oxygen could account for the slightly higher stoichiometric ratio (2.1) found for the as-prepared sample. After sputtering for 60 s, a considerable reduction in the O 1s peak intensity is observed primarily due to the removal of the high binding energy tail, which also supports the presence of chemisorbed oxygen on the surface of the as-prepared film. On the other hand, sputtering for 60 s has markedly increased the Sn $3d_{5/2}$ peak intensity by 20%, which then slowly decreases with increasing sputtering (Figure 3.5b). These intensity changes reduce the stoichoimetric ratio to ~1.6 (Figure 3.5c). Further sputtering to 120 and 210 s causes minor changes to the O 1s and Sn $3d_{5/2}$ intensities, and reduces the ratio further to 1.4. The observed O-to-Sn ratio of 1.4-1.6 is in accord with those reported for TO films prepared by different methods.[89,93,94] Continued sputtering to greater than 400 s reduces the ratio to 1.3-1.2, which remains essentially unchanged even upon sputtering to 3470 s. It should be noted that our reference SnO_2 powder sample had a similar O-to-Sn ratio after long sputtering (1.3 after 400 s). Furthermore, like the reference SnO_2 powder sample, the positions of the Sn $3d_{5/2}$ and O 1s peaks for our TO sample remain effectively unchanged with continued sputtering.

The smaller than expected stoichiometric ratio has been discussed in the literature and is attributed to preferential sputtering of O compared to Sn atoms in SnO_2 films.[93-95] In addition, it has been reported that sputtering of SnO powder causes reduction of Sn^{2+} (at 485.6 eV binding energy) to metallic Sn^0 with a lower binding energy (483.8 eV),[90] which has also been observed in the spectrum of our reference SnO powder with a shift to the binding energy of 485.0 eV. Evidently, SnO_2 is very stable and reduction to lower oxidation states at our sputtering energy of 3 kV was not observed. The absence of a metallic Sn^0 peak in the TO film even after sputtering for 3470 s therefore further supports the conclusion that SnO_2 is the predominant composition throughout the film.

In order to determine the distribution of nanocrystallites as a function of depth, we collected GIXRD profiles at selected sputtering times, all of which resemble the profile for the sample obtained with post-annealing at 400°C (shown in Figure 3.2). Figure 3.5c compares the relative intensity of the (110) XRD peak with the respective O-to-Sn ratio (determined from our XPS experiment) as a function of sputtering depth. In a separate experiment, we estimated the sputtering rate to be ~1 nm/min by completely sputtering away a test TO thin film post-annealed at 400°C on a glass substrate. Evidently, the crystalline phase persists after removal of ~20 % of the film, which suggests that the formation of nanocrystallites occurs throughout the thickness of the layer. However, the intensity reduction of the (110) diffraction peak is found to be more pronounced for the first 670 s of

sputtering (Figure 3.5c), suggesting the presence of a higher density of nanocrystallites in the near-surface region compared to the bulk of the film (or ion-sputtering induced damage to the nanocrystallites at the near-surface).

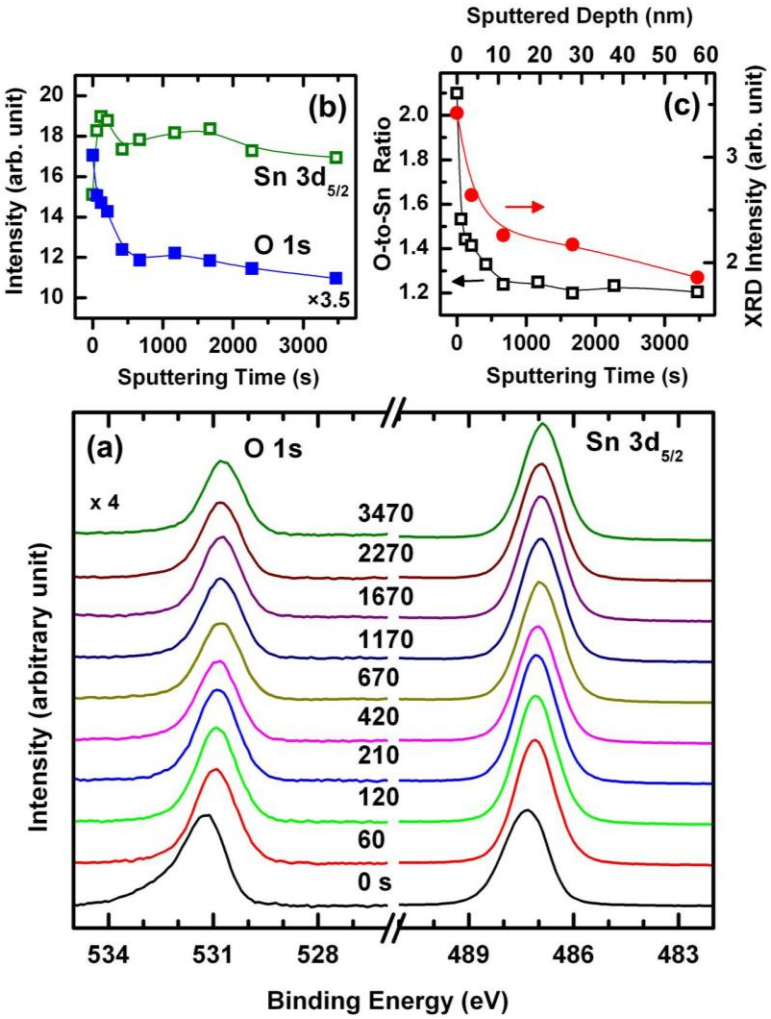

Figure 3.5 (a) XPS spectra of the O 1s and Sn $3d_{3/2}$ regions for the as-deposited tin oxide film prepared with post-oxygen-annealing at 400°C as a function of sputtering time, (b) relative intensities for O 1s and Sn $3d_{5/2}$ peaks, and (c) comparison of the corresponding O-to-Sn ratio (after appropriate correction of the relative sensitivity factors) to the relative area intensity of the (110) XRD peak as a function of sputtering time (with the corresponding sputtering depth shown at top).

In order to further elucidate the role of defects and the amorphous phase in the SnO_2 nanocrystalline film formation, we perform Raman spectroscopy on the samples prepared with post-annealing at 350, 400, 450, and 500°C on glass substrates and at 700 and 900°C on oxidized Si

substrates. The TO films were scraped off from the glass/Si substrates and transferred to a sapphire support in order to avoid the large background scattering from the substrate and to provide more reflection from the collected film material than the as-deposited transparent TO film. Figure 3.6 compares the Raman spectra of the TO films with the reference spectra of SnO_2 powders and of the sapphire support. Evidently, an intense broad band in the 400-800 cm^{-1} region is observed in the spectra for the TO films obtained with the post-anneal temperature between 350 and 700°C. For the TO film prepared with post-annealing at 350°C, the observed broad band appears to center near 560 cm^{-1}, and there is no discernible peak associated with crystalline SnO_2 observed in this range (positions of these SnO_2 characteristic peaks are marked by bars in Figure 3.6). For the TO films prepared with post-annealing at 400-900°C, new peaks are found to emerge on top of the observed broad band. Evidently, the well-resolved peak at 634 cm^{-1} is in good accord with the intense characteristic A_{1g} peak at 631 cm^{-1} of SnO_2 powder. The relative intensity of this peak is found to increase with the post-anneal temperature. In spite of the considerably lower intensities, the other two characteristic SnO_2 peaks at 473 and 772 cm^{-1}, corresponding respectively to E_g and B_{2g} modes, are also observed, with the latter near a prominent sapphire feature at 750 cm^{-1}. Our characteristic SnO_2 Raman peaks and the observed broad band are in good agreement with the results for the SnO_2 nanoparticles calcinated at different temperatures reported by Dieguez et al.[96] The Raman spectrum of the sample prepared at 350°C does not show any of the characteristic peaks of the crystalline SnO_2 phase. This is consistent with our XRD result (Figure 3.2), which shows that the TO film prepared at the crystallization onset (350°C) contains a very small amount of crystalline material with small nanocrystallite size of 3.8 nm. The observed broad band at 400-800 cm^{-1} and the features at 1040, 1300 and 1440 cm^{-1} (open circles, Figure 3.6) are therefore signatures of defects and the amorphous phase, which constitutes a significant proportion of the TO films prepared at 350-500°C. For the films post-annealed at 400-500°C, an additional Raman feature is observed at 1055 cm^{-1} (solid circles, Figure 3.6), and this new feature could be attributed to a nanocrystalline surface mode or to an interaction between the nanocrystalline and amorphous regions. These amorphous-phase-related features are not observed in the reference spectrum of SnO_2 powders. For TO films prepared at 700 and 900°C, the intensities of these amorphous-phase-related features have evidently diminished substantially, which is consistent with the onset of the exponential nanocrystallite growth step above 500°C and the corresponding decrease in proportion to the amount of the amorphous phase in the TO films. Dieguez et al. have attributed the broad Raman band that they observed in the 400-800 cm^{-1} for SnO_2 nanoparticles to overlapping disorder-activated surface modes. [96] While the nature of the

other Raman features observed at 1040, 1055, 1300, and 1440 cm^{-1} remains unknown, it appears likely that they are due to inter-grain or interfacial defect/disorder activated modes resulting from the nanocrystallite growth in an amorphous matrix or from the amorphous phase itself. More detailed investigations would be of interest to further elucidate these spectroscopic phenomena.

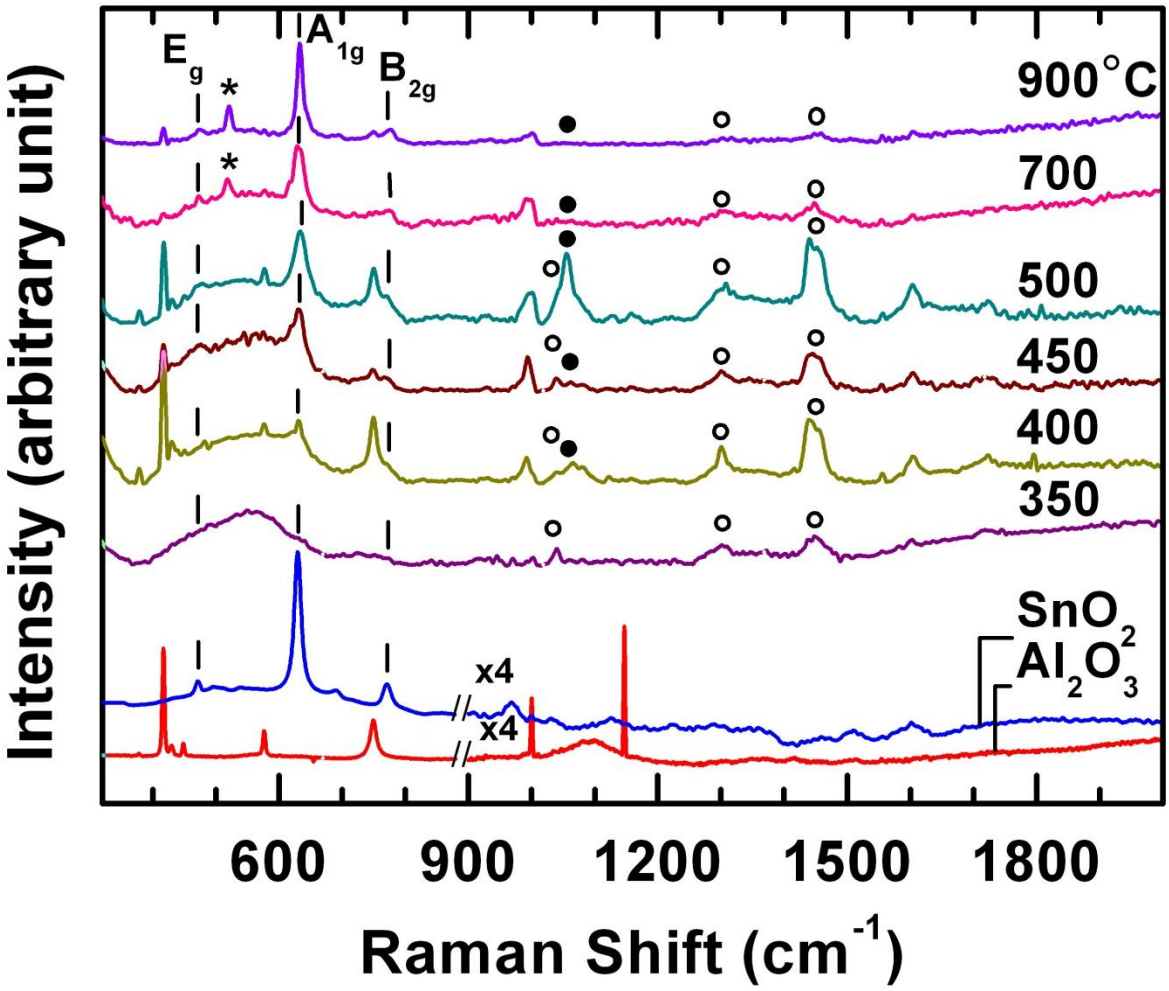

Figure 3.6 Comparison of Raman spectra of the tin oxide films prepared with post-oxygen-annealing at 350, 400, 450, 500, 700, and 900°C with reference spectra of SnO_2 powders and sapphire support (scales for the 900-2000 cm^{-1} region for the reference sapphire support and SnO_2 powders have been changed for clarity). Open and solid circles mark the observed additional sample peaks not found in the reference spectra while the star symbol identifies the peak position of crystalline Si. Spectra are offset for clarity.

3.4 Summary

A simple facile method, involving spin-coating a $SnCl_4$ solution followed by post-oxygen-annealing at 350-500°C, has been developed for synthesizing uniform granular TO films with monodisperse

nanocrystallites of 7-10 nm in size (dia.) on glass substrates (Figure 3.7). The present method is easily scalable for any large-area thin-film deposition and can be used for other substrates including silicon. The resulting films are found to be granular throughout the thickness of the films, with the RMS surface roughness (1.6-2.2 nm) among the smallest of the reported TO films. The XRD data shows the formation of SnO_2 nanocrystallites in an amorphous matrix with increasing post-anneal temperature above the onset at 350°C. Furthermore, the nanocrystallite size is found to increase slowly from 7 nm at 350°C to 10 nm at 500°C, likely due to a strain-limited growth mechanism, and exponentially above a second onset at 500°C. The corresponding TEM measurements give a similar trend in the nanocrystallite size with increasing post-anneal temperature, while the generally larger sizes determined from TEM than those by XRD Scherrer analysis indicate the presence of defects in the nanocrystallites. The TEM result also confirms the remarkably narrow size distribution of nanocrystallites obtained in the strain-limited growth regime (350-500°C). Depth-profiling XPS study supports the single-replacement reaction as the synthesis mechanism, and the complete conversion of the precursor $SnCl_4$ to SnO_2 throughout the entire film. The companion XRD data obtained at different sputtering depths shows a relatively uniform density with increasing depth (i.e. throughout the film) except near the surface where a higher density of nanocrystallites is found. The intensity increase in the characteristic Raman features for SnO_2 below 900 cm^{-1} with increasing post-anneal temperature is consistent with the observed nanocrystallite growth. The presence of defects and the disordered amorphous phase could give rise to the broad band at 400-800 cm^{-1} and the other Raman peaks observed above 1000 cm^{-1}, which begin to diminish with increasing post-anneal temperature at 500°C. Simple control of nanocrystallite growth with post-anneal temperature in the 7-10 nm average size range with a narrow size distribution and a relatively uniform bulk density makes the present method of synthesizing SnO_2 nanocrystalline film particularly useful for gas-sensing applications. Further increase in the nanocrystallite size to 25 nm and greater crystallinity in the film can also be of potential interest to solar cell and nanoelectronic applications.

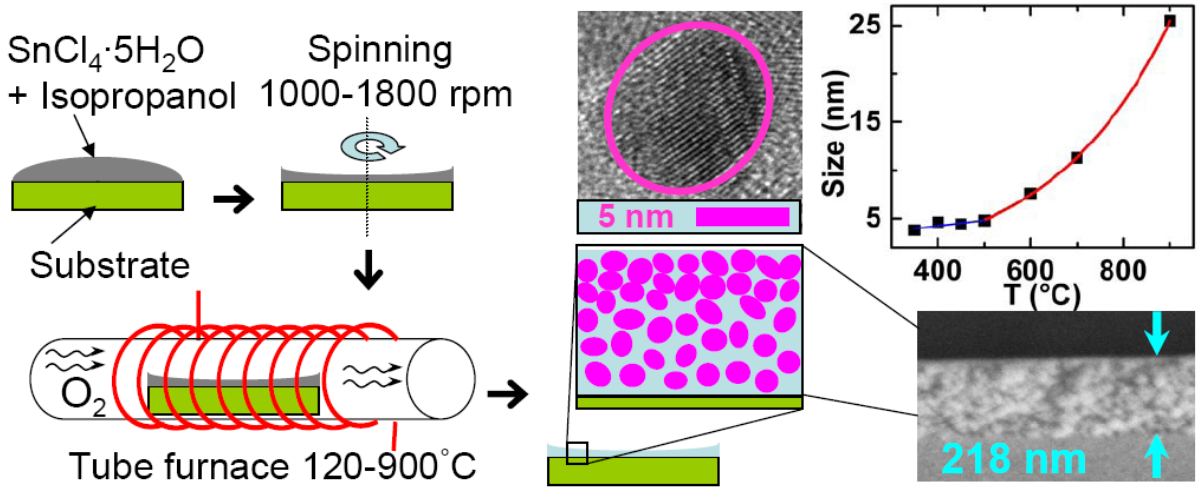

Figure 3.7 Schematic summary of the spin-cast-post-annealing method for synthesizing tin oxide film, and the resulting distribution and size-vs-temperature relation of nanocrystallites in the amorphous matrix.

Chapter 4
Optical and Electronic Transport Properties of Nanocrystalline Tin (IV) Oxide Films with Controllable Nanocrystallite Size in 4-12 nm Range

In the present work, we investigate the electronic structure and transport properties of nanocrystalline TO films with crystallites in the 4-12 nm size range prepared using the method described in the previous chapter. In this chapter, we perform optical and electronic transport measurements on these films, which in conjunction with the extensive structural and compositional characterization shown in the previous chapter can provide a better understanding of their electronic properties. In particular, the optical transmittance of TO films with different nanocrystallite sizes and crystalline-to-amorphous phase ratios are measured in order to determine the effect of the amorphous phase and nanocrystallite size on the corresponding band-gap energies and electronic structures. Furthermore, the effects of the nanocrystallite size and the presence of amorphous phase on the electrical conductivity are studied by measuring the ac resistivity of the films in the temperature range of 50-280 K, which can be understood using the thermal activation and variable range hopping models. Carrying out the electronic transport measurements at low temperature and in high vacuum helps to recover the conduction channels and reduces the adsorption/desorption rate of gases and their effects on the electronic transport. These measurements elucidate the nature of the charge carrier activation and transport through the different possible conduction channels.

4.1 Morphology and Crystal Structure Characterization

In our previous chapter, we demonstrated that the size of the nanocrystallites in a thin spin-coated TO film (270±50 nm thick) can be easily controlled over the 4-25 nm size range by manipulating T_{Anneal}.[97] In particular, X-ray diffraction (XRD) studies of TO films obtained at different T_{Anneal}'s show an onset of crystallization at 350°C (Figure 4.2). The corresponding crystallite sizes are estimated by applying the Debye-Scherrer analysis to the broadening of the (110) peak, and are found to be in good agreement with the average nanocrystallite sizes estimated from TEM measurement (shown in Figure 4.2, inset a-c). Both the XRD and TEM results also confirm the presence of a single SnO_2 phase in

these TO films. As shown in Figure 4.2 inset d, the nanocrystallite size remains in the 4-5 nm range for T_{Anneal} = 350-500°C, which is likely due to a strain-limited growth mechanism.[97] For T_{Anneal} > 500°C, the resulting exponential increase in nanocrystallite size with increasing temperature suggests an Arrhenius-like growth mechanism.

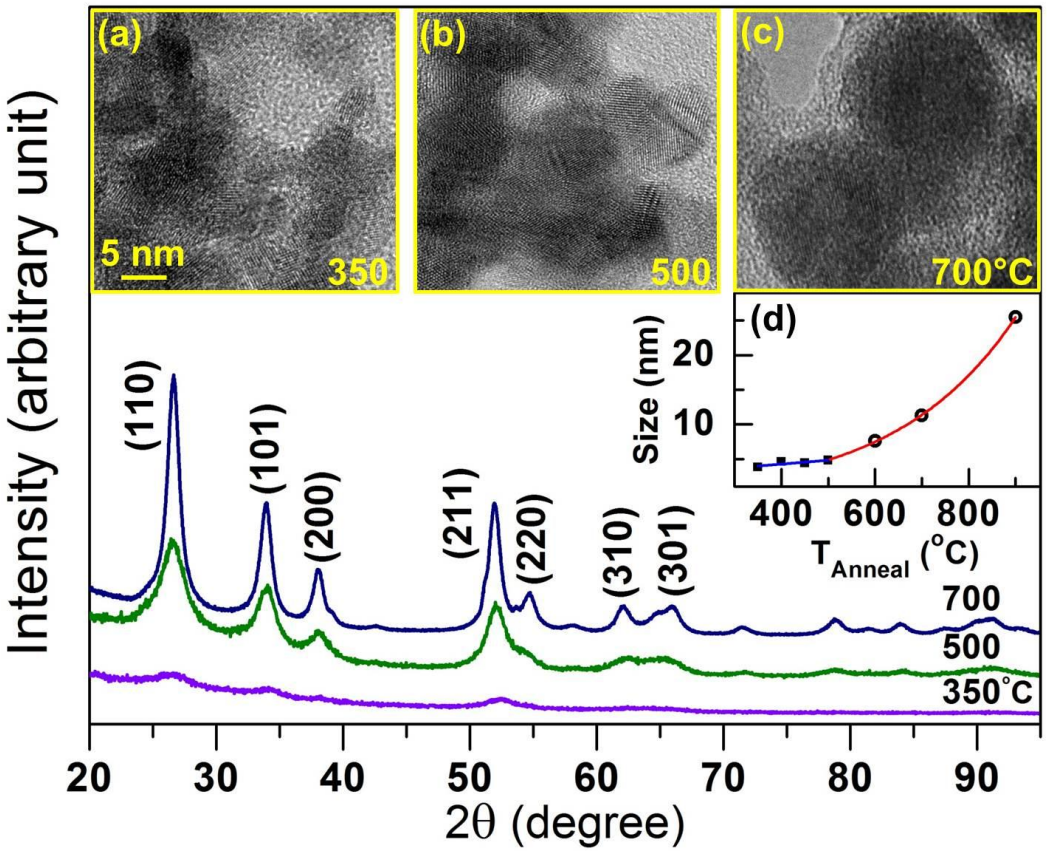

Figure 4.1 Typical glancing-incidence X-ray diffraction patterns of SnO_2 films prepared with post-annealing temperatures (T_{Anneal}) of 350 and 500°C on glass substrates and of 700°C on a quartz substrate, where glass and quartz substrates are used for films obtained with T_{Anneal} = 350, 400, 450 and 500°C and of 600, 700, and 900°C, respectively. Typical TEM images for the samples obtained with T_{Anneal} = (inset a) 350°C, (inset b) 500°C, and (inset c) 700°C are shown with the same scale. Inset (d) shows the change in the crystallite size with increasing T_{Anneal}, with the data points in the 350-500°C range fitted by a straight line while those in the 500-900°C range fitted by an exponential curve.

4.2 Optical Properties

Figure 4.3 shows the UV-Visible transmission spectra of the TO films obtained with T_{Anneal} = 350-500°C on glass and with T_{Anneal} = 550-700°C on quartz substrates. Evidently, these films all exhibit a

high optical transparency of 90-100% in the visible region (1.2-3.5 eV). The absorption edges for films obtained with T_{Anneal} at and below 500°C are found to be very close to that of the glass substrate (Figure 4.3a), while those obtained with T_{Anneal} above 500°C show a distinctly different absorption edge from the quartz substrate (Figure 4.3b). From the absorption coefficient given by the Beer-Lambert law, $\alpha = -\frac{\ln(I)}{d}$, where I is the transmittance and d is the optical path length, we calculate the band-gap E_g using the Tauc equation for absorption in a direct-band-gap material: $\alpha h\nu = A(h\nu - E_g)^{1/2}$, where A is a constant and hν is the incident photon energy.[41,98,99] Insets of Figure 4.3 show the corresponding plots of $(\alpha \cdot h\nu)^2$ versus hν for the TO films obtained on the glass and quartz substrates, in which the zero-crossing of the tangent to the curve provides an estimate of the band-gap of the respective sample. The band-gap values so determined for all the TO films on glass are clearly different than the estimated band-gap value of 4.07 eV for the glass substrate. This difference is not due to scattering from the additional TO films, because the samples exhibit essentially the same high transmittance in the visible region as the pristine glass substrate. The estimated band-gap values for the TO films obtained with T_{Anneal} = 350-500°C are found to be 3.83-3.87 eV, indicating that these crystalline samples obtained with T_{Anneal} = 350-500°C (Figure 4.2, inset) have similar energy band structures. Crystallization of the samples at 350-500°C therefore has not led to any detectable change in the band structure. The band-gap values estimated for samples obtained on quartz with higher T_{Anneal} of 550, 600, and 700°C are 3.90, 3.78, and 3.71 eV, respectively. It should be noted that band-gap value for TO film obtained with T_{Anneal} = 550 °C on quartz (Figure 4.3b) is essentially the same as those obtained with $T_{Anneal} \leq 500$°C on glass (Figure 4.3a). For the TO films deposited on quartz, their band-gap values follow a discernible decreasing trend with increasing T_{Anneal} above 550°C (Figure 4.3b, inset). Furthermore, the estimated band-gap values for all the TO films (obtained with T_{Anneal} = 350-700°C) are found to be higher than the reported value for single-crystalline SnO_2 (3.6 eV).[7,100] The conduction band in the electronic structure of TO is composed of the 5s orbitals of Sn and has a strongly dispersive s-type shape.[7,101] The observed blue shift in the band-gap can therefore be explained by the Moss-Burstein effect, where increased n-doping due to a large number of defects in the crystal fills more conduction band states, leading to an increase in the measured optical band gap. Similar blue shifts have also been found for In_2O_3, ZnO, CdO, and other transparent conducting oxides.[7,102] Our optical transmission measurement therefore indicates that even the nanocrystalline films obtained with a high T_{Anneal} (550-700°C) that show a high degree of crystallinity still have a high carrier density.

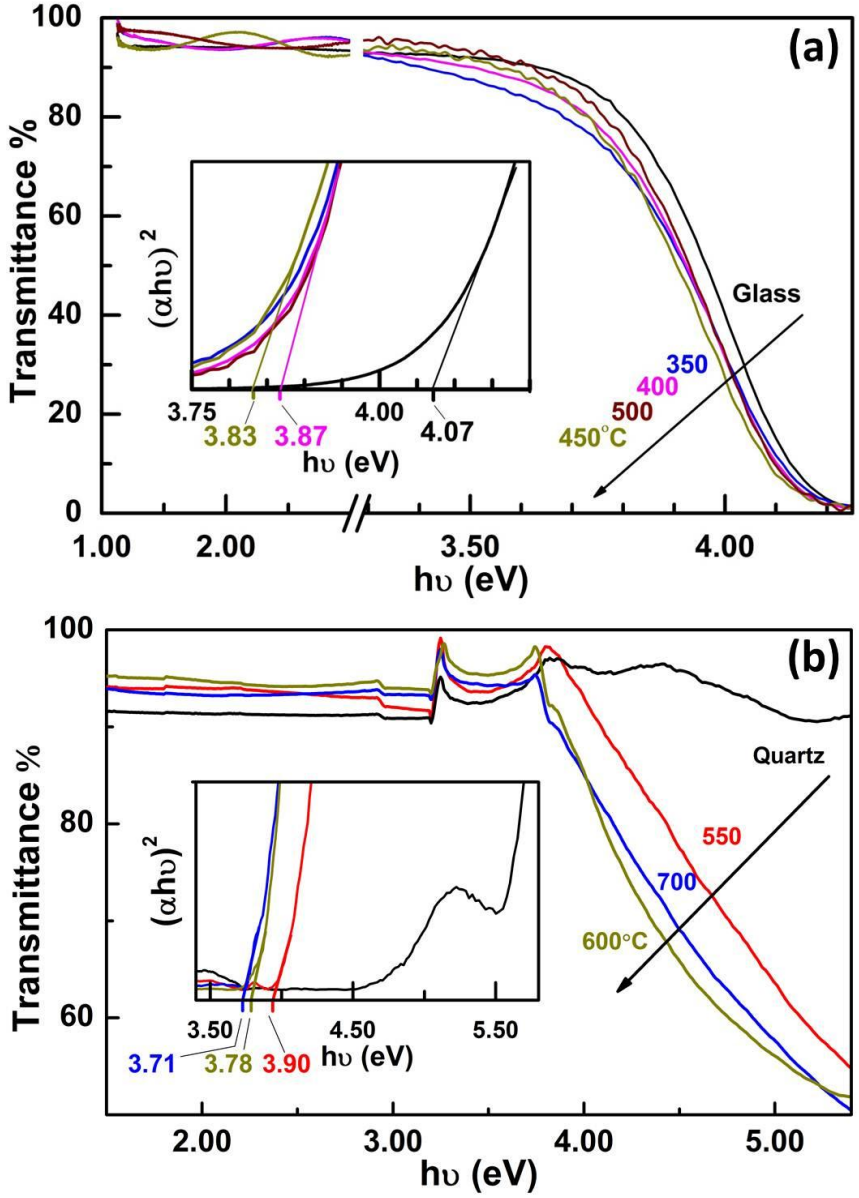

Figure 4.2 UV-Visible spectra of the SnO_2 films prepared with different post-annealing temperatures (a) of 350-500°C on glass and (b) of 550-700 °C on quartz substrates. Insets show the $(\alpha \cdot h\nu)^2$ versus hν plot illustrating the method of estimating the band-gap.

4.3 Electrical Properties

The ac resistivity results for TO films obtained with T_{Anneal} = 350-700°C in the temperature range of 50-280 K are shown in Figure 4.4. In order to check the reproducibility of the observed resistivity

behavior with temperature, dc measurement is also performed on the films obtained with T_{Anneal} = 400, 450, and 600°C. The similar dc resistivity behavior so observed confirms the ac resistivity result. In spite of our best effort to decrease the gas exchange rates on the surface of the samples by keeping the samples in vacuum for at least 24 h before the measurement, the repeated cooling and heating cycles in between our resistivity measurements could still cause a general variation of 40 Ω·cm in the room-temperature resistivity values. This behavior is due to the small size of the crystalline grains and the high sensitivity of the highly resistive film to the amount of adsorbed gases, which lead to the exceptional gas sensing properties of SnO_2. Similar variation in resistivity due to gas adsorption has also been reported to occur for TO films.[85,103,104] In order to better present the changes in the resistivity behavior for all the samples, the resistivity curves plotted in Figure 4.4 are normalized to the resistivity value at 280 K of the sample obtained with T_{Anneal} = 350°C (8.5 Ω·cm). All the analysis is done with the raw data and not with the normalized data shown in Figure 4.4. The films obtained with T_{Anneal} < 350°C are found to be amorphous and not conductive. The amorphous phase that is present with particularly high volumetric percentage in the samples obtained with low T_{Anneal} of 350-500°C will therefore not contribute to the conductivity of these samples. Evidently, for the films obtained with $T_{Anneal} \geq 350$°C (shown in Figure 4.4), nearly linear semiconductor-like trends over 120-280 K (denoted as high-temperature or HT region) and below 90 K (denoted as low-temperature or LT region) are observed, along with an intermediate region with complex behavior at 90-120 K (marked as a gray area in Figure 4.4). Moreover, for all the films, there is a decrease in the tangential slope of the curve in going from the HT region to the LT region.

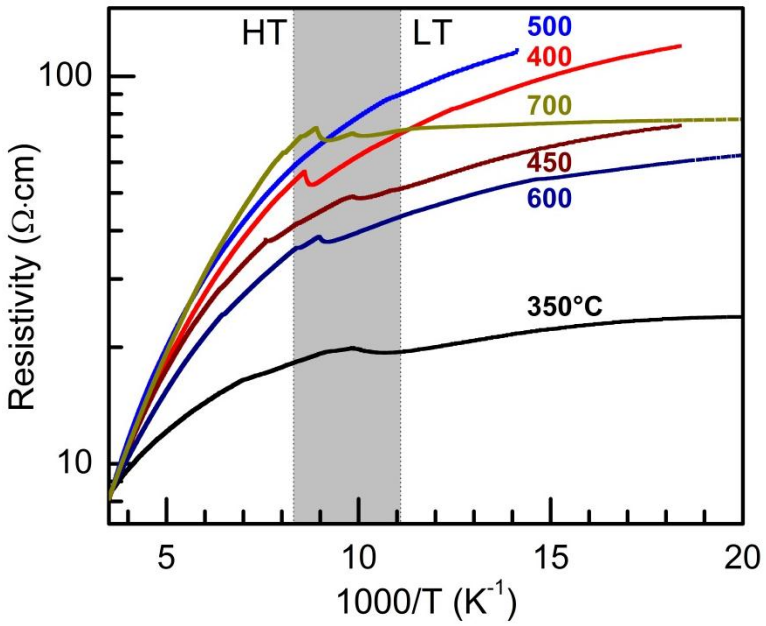

Figure 4.3 Resistivity of the SnO2 films prepared with post-annealing at 350-700°C in the 50-280 K range. To better illustrate the change in their behavior, the resistivity curves are normalized to the resistivity value at 280 K of the sample obtained with post-annealing at 350°C, only for presentation purpose. Gray area marks the intermediate region (90-120 K) between the HT (120-280 K) and LT (50-90 K) regions.

In order to examine the underlying conduction mechanism, we fit the resistivity data to different electronic transport models involving the thermal activation and variable-range hopping (VRH) mechanisms, both of which have been extensively used to describe the transport in semiconducting nanostructures including CdSe nanocrystals,[105] belt-shaped monocrystals[106] and nanowires[107] of SnO_2, and thin films of In_2O_3.[108] In the thermal activation model, the resistivity, ρ, is given as a function of temperature, T, by:

$$\rho(T) = \rho_0 \exp\left(\frac{E_a}{k_B T}\right), \qquad \text{[Equation 1]}$$

where E_a is the activation energy of carriers, k_B is the Boltzmann constant, and ρ_0 is the pre-exponential factor. The corresponding relation used for the VRH mechanisms is:

$$\rho(T) = \rho_0 \exp\left[\left(\frac{T_0}{T}\right)^{\frac{1}{n+1}}\right], \qquad \text{[Equation 2]}$$

where n = 1, 2, and 3 for the Efros-Shklovskii or Coulomb Gap (CG), two-dimensional (2D), and three-dimensional (3D) transport models, respectively, and ρ_0 is the pre-exponential factor. The T_0 parameter is related to the density of states at the Fermi level, g_f, and the carrier localization length, a, by: $T_0 = \frac{\beta_{CG} e^2}{k_B \kappa a}$, $\frac{\beta_{2D}}{k_B g_f a^2}$, and $\frac{\beta_{3D}}{k_B g_f a^3}$, for the CG, 2D, and 3D VRH models, respectively, where κ is the dielectric constant and β is obtained from Monte Carlo simulation (with β_{CG}=2.8, β_{2D}=13.8, and β_{3D}=21.2).[109,110] The results for E_a and T_0 obtained by fitting the resistivity data in the LT and HT regions for the samples obtained with different T_{Anneal}'s are presented in Table 4.1. The near-unity values for the coefficient of determination, R^2, obtained for these models indicate that the experimental data can be interpreted satisfactorily in both the thermal activation and VRH models. However, the 3D-VRH model gives the best fit to the data, suggesting that the electronic transport in these films is best described in terms of three-dimensional carrier hopping. This therefore shows that conduction is not restricted to lower dimensions, in contrast to that reported for films less than 100 nm thick,[111112] because of the three-dimensional conduction network of nanocrystallites distributed in the entire thickness of the thicker (270±50 nm) TO film (Figure 4.1d).[97]

The observed decrease in the tangential slope of the resistivity curve in going from the HT to LT region and the complex behavior in the intermediate region (90-120 K) can be explained by considering a two-medium resistance network model schematically shown in Figure 4.5a. Due to the presence of chemisorbed oxygen, a charge-depletion layer forms around the surfaces of and in the grain boundaries between the nanocrystallites. This layer also extends over the interconnecting neck when the nanocrystalline grain size is comparable to twice the Debye length,[113] resulting in a potential barrier (ϕ_b) for electronic transport through the grains (i.e. across the grain boundaries). Although the carrier concentration in the charge-depletion layer is lowered than that in the grain by an exponential factor of $\exp(-\frac{\phi_b}{k_B T})$, charge transport through this layer could still contribute to the conductivity of these highly resistive nanocrystalline TO films especially for T < 100 K, i.e. in the LT region (Figure 4.4). In the thermal activation model, two E_a values are found for the films obtained with T_{Anneal} = 350-700°C, by fitting their corresponding resistivity data in the LT and HT regions. The values so obtained for the LT region (0.4-7.7 meV) are considerably lower than those obtained in the HT region (14.6-41.6 meV) (Table 4.1). The difference in the E_a values observed in the HT and LT regions supports the presence of a potential barrier for transport across the grain boundaries, which becomes

apparent in the HT region but not in the LT region. In order to demonstrate that the two-medium model can account for the observed resistivity behavior of the TO films, we adopt a parallel resistor model as equivalent circuit for this two-medium structure, where the predominant resistivity in the HT region associated with transport through the grains and across the grain boundaries is represented by ρ_{HT} and the predominant resistivity in the LT region related to transport through the charge-depletion layer is denoted by ρ_{LT}. The total resistivity of two parallel resistors (ρ_{LT} and ρ_{HT}) is given by:

$$\rho_{Total} = \frac{\rho_{HT} \times \rho_{LT}}{\rho_{HT} + \rho_{LT}} \qquad \text{[Equation 3]}$$

As an example, we compare in Figure 4.5b two calculated resistivity curves to the experimental resistivity curve for the sample obtained with T_{Anneal} = 700°C, which is chosen because it exhibits a more dramatic difference in the E_a values and is therefore easier to discern the quality of fit (Table 4.1). By using the resistivity values obtained by fitting the data in the LT (ρ_{LT}^{0}) and HT regions (ρ_{HT}^{0}) independently, we calculate the corresponding ρ_{Total}^{0} according to Equation 3. Although this "independent" parallel resistor model gives qualitative agreement in the higher HT and lower LT regions and in providing a parallel trend with the experimental curve, there is obvious discrepancy. To correct for the discrepancy, which clearly originates from assuming the independent resistivity behaviors in the LT and HT regions, we recalculate the total resistivity ρ_{Total}^{SE} by fitting the data over the entire temperature range (280-50 K) iteratively with Equation 3 to generate new ρ_{LT}^{SE} and ρ_{HT}^{SE} with their corresponding E_a values as semi-empirical (SE) fitting parameters. Evidently, excellent agreement between the calculated ρ_{Total}^{SE} curves with the experimental data is obtained, despite the deviations introduced by the complex resistivity behavior in the intermediate region in the fitting process (Figure 4.5b). These calculations validate our hypothesis of two-medium electronic transport in the TO films.

The optimized E_a values obtained for the calculated ρ_{Total}^{SE} curves for all the TO films are given in Table 4.1 and plotted as a function of T_{Anneal} in Figure 4.5c. The E_a^{SE} values for the electronic transport dominant in the HT and LT regions are found to be 48.1-61.0 meV and 0.1-6.1 meV, respectively. The difference between the E_a^{SE} value for transport through the grains and across the grain boundaries, ρ_{HT}, and that through the charge-depletion layer, ρ_{LT}, for each sample corresponds to the potential barrier. The small variations in the E_a^{SE} difference (48.0 -60.5 meV) suggest a potential barrier of similar magnitude for all the TO films regardless of the different T_{Anneal}'s

employed. Such a potential barrier could be due to similar gas adsorption densities in the neck regions in all the TO films, which suggests that the neck sizes remain smaller than twice the Debye length in spite of the increase in the nanocrystallite size from 4 nm to 12 nm. The variation in the resistivity in the intermediate temperature region (90-120 K) can be explained by the presence of potential barriers with different heights due to the statistical distribution in the neck size. The statistical variation in the potential barrier height would lead to different onset temperatures for "blocking" the conduction channels at various grain boundaries, and electronic transport would continue through the remaining active conduction routes as long as the low percolation limit has not reached. These changes in the conduction routes could lead to the observed resistivity variation in the intermediate temperature region, where electronic transport through the crystalline grains is nearly comparable to that through the depletion layer.

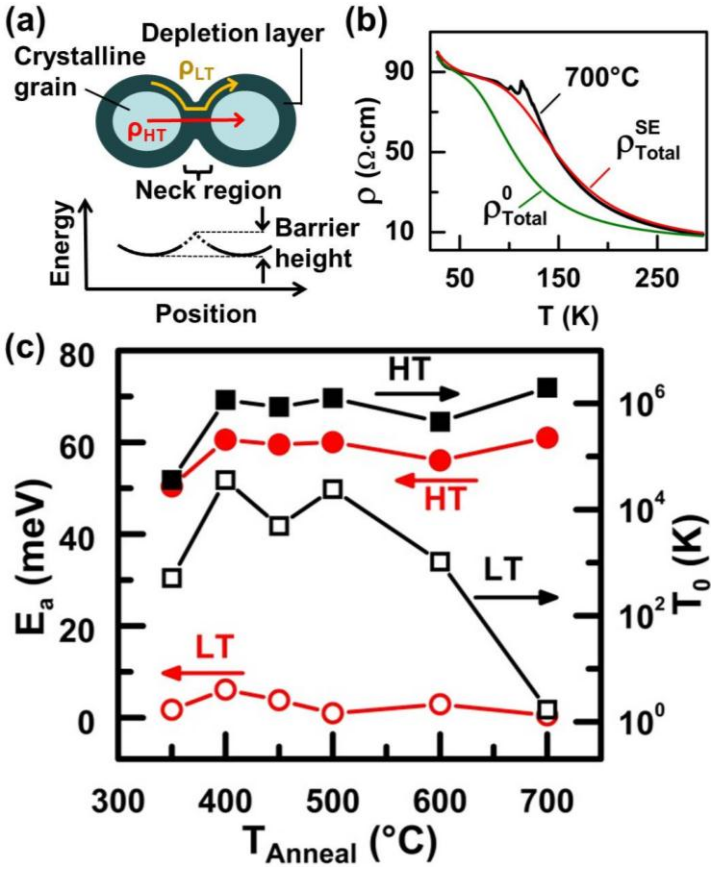

Figure 4.4 (a) Schematic representation of the two-medium model for electronic transport through the neck region of two adjoining crystalline grains (medium one), with a potential barrier, and through the depletion layer (medium two). (b) Comparison of the resistivity data of the sample obtained with post-annealing at 700°C with the ρ_{Total}^{0} curve calculated by treating the independently

obtained low-temperature (LT) resistivity ρ_{LT}^{0} and high-temperature (HT) resistivity ρ_{HT}^{0} in parallel, and with the ρ_{Total}^{SE} curve obtained by fitting iteratively to the parallel resistor model with ρ_{LT}^{0} and ρ_{HT}^{0} as the initial values. (c) T_0 parameter, obtained from fitting the 3D-variable-range hopping model to the resistivity data in the HT and LT regions, and the E_a^{SE} values, obtained for the HT and LT regions by fitting the resistivity data over the entire temperature range using the parallel resistor model, plotted as a function of the post-annealing temperature, T_{Anneal}, as indicated in Table 4.1.

The fitted results (Table 4.1) show that electronic transport in each medium follows the 3D-VRH mechanism. Figure 4.5c shows the corresponding T_0 parameters obtained by fitting the resistivity data in the HT and LT regions (representing transport through the grains and through the depletion layer, respectively) for the TO films prepared with different T_{Anneal}'s. The T_0 value of 3.6×10^4 K for the sample obtained with T_{Anneal} = 350°C rises sharply to 1.2×10^6 K when T_{Anneal} is increased to 400°C and stays almost unchanged with increasing T_{Anneal} above 400°C (Figure 4.5c). As T_0 is inversely proportional to the density of states at the Fermi edge (g_f) and the carrier localization length (a), it is not surprising that its value has been reported to vary significantly for different materials, including 1.1×10^9 K for belt-shape monocrystals of SnO_2,[106] 4.3×10^7 K for CdSe quantum dots,[109] and 7.7×10^3 K for F-doped thin films of SnO_2.[114] In accord with our TEM and XRD results (Figure 4.2) that show improved crystallinity with increasing T_{Anneal}, the carrier localization length does not decrease with increasing T_{Anneal}. It can therefore be concluded that the observed increase of nearly two orders of magnitude in T_0 with increasing T_{Anneal} from 350 to 400°C in the HT region is due to a sharp decrease in the carrier density at the Fermi edge. This is also in agreement with the results reported by Li et al.,[101] which correlate the carrier density at the Fermi edge with the density of oxygen vacancies as one of the common point defects in the crystal structure of TO. The nearly unchanged T_0 value with further increasing T_{Anneal} to 700°C suggests that the density of states at the Fermi energy is almost constant for samples prepared with post-annealing above 400°C. Moreover, in the LT region, we observe a rise in T_0 value with increasing T_{Anneal} from 350 to 400°C, which can be explained by the high carrier density of the sample obtained with T_{Anneal} = 350°C (similar to that for the HT region). The T_0 value stays fairly stable for samples obtained with T_{Anneal} = 400-500°C and then starts to drop for the sample obtained with T_{Anneal} = 600°C. For the sample obtained with T_{Anneal} = 700°C, this decreasing trend reaches a dramatic reduction of almost four-orders of magnitude in T_0, compared to that obtained for samples with T_{Anneal} = 400-500°C. Since the density of states at the Fermi edge is not increasing, as suggested by the observed red shift in the band-gap of the samples obtained with T_{Anneal} = 600 and 700°C according to the optical measurement, and also by the

TEM and XRD results, this sharp drop in T_0 indicates a correspondingly steep increase in the localization length for the samples obtained with T_{Anneal} = 600 and 700°C. This increase in the localization length suggests that in the Arrhenius growth region, overcoming the crystalline growth barrier improves the crystallinity of these films and the interconnections among the nanocrystallites, and also drastically reduces the grain boundary scattering effects.

Table 4-1 Room-temperature resistivity (ρ at 280 K) for TO films obtained with different post-annealing temperatures (T_{Anneal}); activation energies in the thermal activation model: E_a^0 obtained by fitting the data in the high-temperature (HT) and low-temperature (LT) regions separately, and E_a^{SE} obtained by fitting the data over the full temperature range using the parallel resistor model (Equation 3); and T_0 values in the variable-range hopping models obtained by fitting the resistivity data in the specified HT and LT regions. The adjusted coefficients of determination, adj. R^2, are given in square parentheses.

T_{Anneal} (°C)	ρ at 280 K (Ω·cm)	HT/LT Regions (K)	Thermal Activation		Variable-Range Hopping		
					CG	2D	3D
			E_a^0 (meV) [adj. R^2]	E_a^{SE} (meV) [adj. R^2]	T_0 (K) [adj. R^2]	T_0 (K) [adj. R^2]	T_0 (K) [adj. R^2]
			HT/LT	HT/LT	HT/LT	HT/LT	HT/LT
350	8.5	296-114/ 92-51	14.6 [0.9591]/ 2.4 [0.9693]	50.4/ 1.7 [0.9972]	643 [0.9799]/ 47 [0.9803]	4.1×10^3 [0.9852]/ 131 [0.9833]	3.6×10^4 [0.9876]/ 514 [0.9847]
400	4.0	297-116/ 113-54	35.0 [0.9804]/ 7.7 [0.9713]	60.6/ 6.1 [0.9983]	3.6×10^3 [0.9936]/ 419 [0.9851]	5.5×10^4 [0.9964]/ 3.3×10^3 [0.9887]	1.2×10^6 [0.9975]/ 3.6×10^4 [0.9903]
450	51.6	296-131/ 94-49	34.2 [0.9767]/ 4.2 [0.9626]	59.5/ 3.8 [0.9990]	3.3×10^3 [0.9902]/ 144 [0.9767]	4.5×10^4 [0.9934]/ 711 [0.9807]	8.6×10^5 [0.9947]/ 4.9×10^3 [0.9825]
500	28.9	288-111/ 89-70	34.5 [0.9685]/ 7.1 [0.9956]	48.1/ 0.1 [0.9922]	3.7×10^3 [0.9863]/ 346 [0.9972]	5.8×10^4 [0.9907]/ 2.4×10^3 [0.9977]	1.3×10^6 [0.9926]/ 2.4×10^4 [0.9979]
600	2.6	299-121/ 84-31	28.4 [0.9802]/ 2.2 [0.9794]	56.1/ 4.2 [0.9985]	2.3×10^3 [0.9934]/ 56.5 [0.9910]	2.7×10^4 [0.9962]/ 205 [0.9935]	4.5×10^5 [0.9973]/ 1.0×10^3 [0.9945]
700	9.9	296-124/ 88-28	41.6 [0.9898]/ 0.4 [0.9892]	61.0/ 0.5 [0.9937]	4.9×10^3 [0.9980]/ 2.2 [0.9885]	8.3×10^4 [0.9993]/ 1.7 [0.9868]	2.0×10^6 [0.9996]/ 1.7 [0.9856]

4.4 Concluding Remarks

In summary, we study the optical and electronic transport properties of tin (IV) oxide nanocrystalline films prepared by a simple spin-coating/post-annealing method. These TO films are found to consist of nanocrystallites in the 4-12 nm size range in an amorphous-phase matrix. These TO films are highly transparent in the visible region with discernibly larger band-gaps of 3.71-3.87 eV than bulk SnO_2, likely due to Moss-Burstein effect, indicative of the high carrier densities in these TO films. The formation of the nanocrystalline phase above T_{Anneal} = 350°C leads to a semiconducting film, with two distinct resistivity behaviors between 50-90 K (LT), and 120-280 K (HT). The 3D variable-range hopping model provides the best fit to the measured resistivity in the HT and LT regions. The different resistivity behaviors observed in the LT and HT regions can be explained by the two-medium model that takes into account electronic transport through the grains and across the grain boundaries with high carrier densities and through the depletion layer with very low carrier densities. This transport picture is supported by the excellent fit of our experimental data by the parallel resistor model. The energy corresponding to the potential barrier heights so obtained for transport through the grain boundaries for samples with T_{Anneal} = 350-700°C is found to be 48.0-60.5 meV. Moreover, the variation in the resistivity in the intermediate temperature region (90-120 K) can be explained by the change in the aforementioned conduction routes due to existing distribution in the neck sizes between the grains. According to the 3D-VRH model, the observed trend in the T_0 value in the HT region shows that the carrier density in the crystalline grains for the TO film obtained with T_{Anneal} = 350°C is reduced upon increasing T_{Anneal} to 400°C and becomes nearly constant above 400°C. The decreasing T_0 trend for the LT region shows that increasing T_{Anneal} above 500°C leads to an increase in the localization length of the carriers, indicating a pronounced improvement in the crystallinity, interconnections, and the conduction channels in the exponential-growth regime. These results provide insights to the energy band structure and further elucidate the carrier transport in this network of TO nanocrystallites. These electronic transport properties depend on the nanocrystallite size, which can be effectively controlled by manipulating the post-annealing temperature. In addition to the fundamental scientific interest, this information is crucial to potential applications of these nanocrystalline TO films in different areas including gas sensing, catalysis, and transparent conductive oxide materials.

Chapter 5
Structural Transition, Photoluminescence and Magnetic Orderings of the Eu^{3+}-doped Nanocrystalline SnO_2 Films at High Dopant Levels

In the present work, we use the spin-coating method, described within the fabrication systems (Chapter 2) to dope Eu^{3+} ion with different molar ratios into TO nanostructures by dissolving the Eu salt along with the Sn salt in isopropanol. This chapter presents a systematic study of the effects of varying the initial Eu^{3+} concentration up to 20 mol. % on the nature of nanocrystalline TO film and correlate their physical and compositional structures to their luminescence and magnetic properties.

5.1 Morphology, crystal structure and composition of Eu-doped films

Figure 5.1 compares the SEM image of the SnO_2 film with those obtained with different Eu concentrations (Eu 5%, Eu 10% and Eu 20%), all obtained with post-annealing at 700°C, and with those of the Eu 10% samples obtained with post-annealing at 500°C and 900°C. It should be noted that all the films remain highly conductive as illustrated by the SEM images obtained without any conductive layer coating. Evidently, the SnO_2 film exhibits a granular structure with a grain size of 10-20 nm (Figure 5.1a). The Eu 2% film (not shown) and and the Eu 5% film (Figure 5.1b) are found to have a similar granular structure, where the grains are less prominent and they tend to fuse into each other. For the Eu 10% (Figure 5.1c) and Eu 20% films (Figure 5.1d), a web-like structure is formed with some distinctly brighter grains (10-20 nm in size) on top of this layer. The presence of these grains suggests the formation of a new crystalline phase in these highly doped films. The Eu 10% films prepared with T_{Anneal} = 500°C (Figure 5.1e) and 900°C (Figure 5.1f) show a significantly different morphology than that prepared with T_{Anneal} = 700°C (Figure 5.1c). The Eu 10% film obtained with T_{Anneal} = 500°C shows a porous film-like morphology without any discernible grains (Figure 5.1e), while the Eu 10% film prepared with T_{Anneal} = 900°C exhibits a distinct granular morphology (Figure 5.1f) with the grains more separated and considerably larger (20-30 nm in size) than those observed in any of the films obtained with T_{Anneal} = 700°C (Figure 5.1c). These observations suggest that the Eu 10% film prepared with T_{Anneal} = 500°C is mainly amorphous, and crystallization has not occurred due to insufficient thermal energy On the other hand, the Eu 10%

film prepared with T_{Anneal} = 900°C is highly crystalline with homogeneous crystallization over the entire film, unlike that observed for the Eu 10% sample obtained with T_{Anneal} = 700°C.

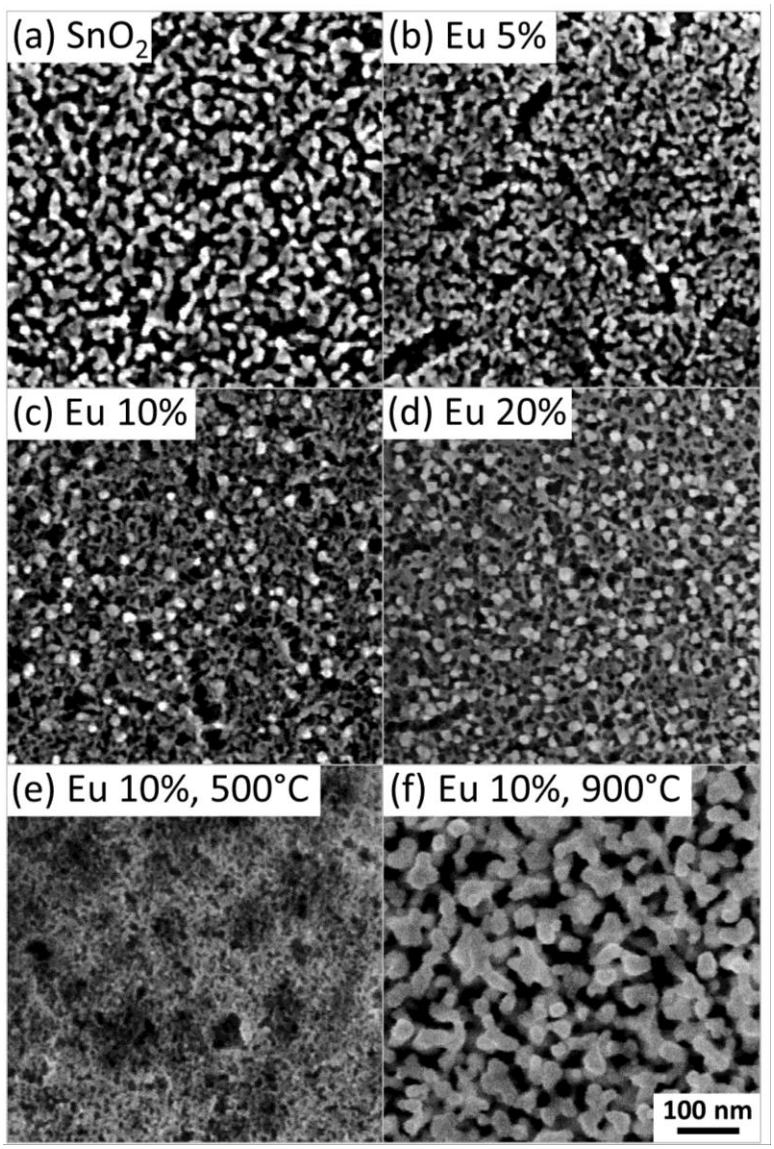

Figure 5.1 SEM images of (a) SnO_2 film (without Eu doping) and (b) Eu 5%, (c) Eu 10%, and (d) Eu 20% films, all obtained with T_{Anneal}=700°C, and SEM images of the Eu 10% films obtained with T_{Anneal} of (e) 500°C, and (f) 900°C.

In order to investigate the effect of Eu doping on the crystalline structure of the TO nanocrystalline film, we perform GIXRD on all the samples (Figure 5.2). The GIXRD pattern for the SnO_2 film

shows a single polycrystalline tetragonal SnO_2 phase (PDF2#00-041-1445), and the Debye-Scherrer analysis performed on the most prominent (110) peak at 26.62° (by assuming peak broadening due only to a size effect) gives a crystallite size of 8 nm. Upon doping, the intensities of all the peaks for the Eu 2% and Eu 5% samples are found to be greatly reduced, suggesting that the presence of Eu ions is suppressing the crystallization of the TO film, which is also consistent with the smaller estimated crystallite sizes (5 nm) than that of the undoped SnO_2 sample. Their corresponding (110) peak positions are also shifted to a lower angle by 0.08° for Eu 2% and by 0.05° for Eu 5%, which indicates an increase in the lattice constant of the TO nanocrystallites by 0.3%-0.2%, likely as a result of substitution of the Sn^{4+} ion (~0.71 Å [16]) by the bigger Eu^{3+} ion (~0.98 Å [16]) in the host lattice. For the Eu 10% and Eu 20% films, their crystallinity appears to be greatly suppressed, with the emergence of an intense broad peak near 30° and a weaker broad peak at 53°, while the (110), (101), and (211) TO peaks becoming barely detectable. The GIXRD pattern for the Eu 10% film prepared with T_{Anneal}=500°C is found to be similar to that of the Eu 20% film obtained with T_{Anneal}=700°C, with only the broad peaks at 30° and 53° remaining, and total disappearance of the TO crystalline peaks. According to the Scherrer analysis, the large fwhm (6.68°) of the feature at 30° corresponds to an unknown phase with ~1 nm crystallites, i.e. poor crystallinity. On the other hand, the GIXRD pattern for the Eu 10% obtained with T_{Anneal}=900°C reveals a new cubic pyrochlore $Eu_2Sn_2O_7$ phase (PDF2#00-013-0182), in addition to the tetragonal SnO_2 phase. The presence of the most intense (222) peak of the $Eu_2Sn_2O_7$ phase at 29.56° suggests that the broad peak at ~30° found for the Eu 10% and Eu 20% films could be due to emergence of this phase. The GIXRD results therefore show that Eu doping is suppressing the formation of TO nanocrystallites to a smaller size, leading to the formation of a poorly crystalline $Eu_2Sn_2O_7$ phase. This TO crystallization can also be greatly inhibited by decreasing T_{Anneal} to 500°C. Increasing T_{Anneal} to 900°C, however, leads to crystallization of both separated SnO_2 and $Eu_2Sn_2O_7$ phases with larger crystallite sizes (of 12 nm and 15 nm, respectively) than the samples prepared with T_{Anneal} =700°C, consistent with the SEM results (Figure 5.1).

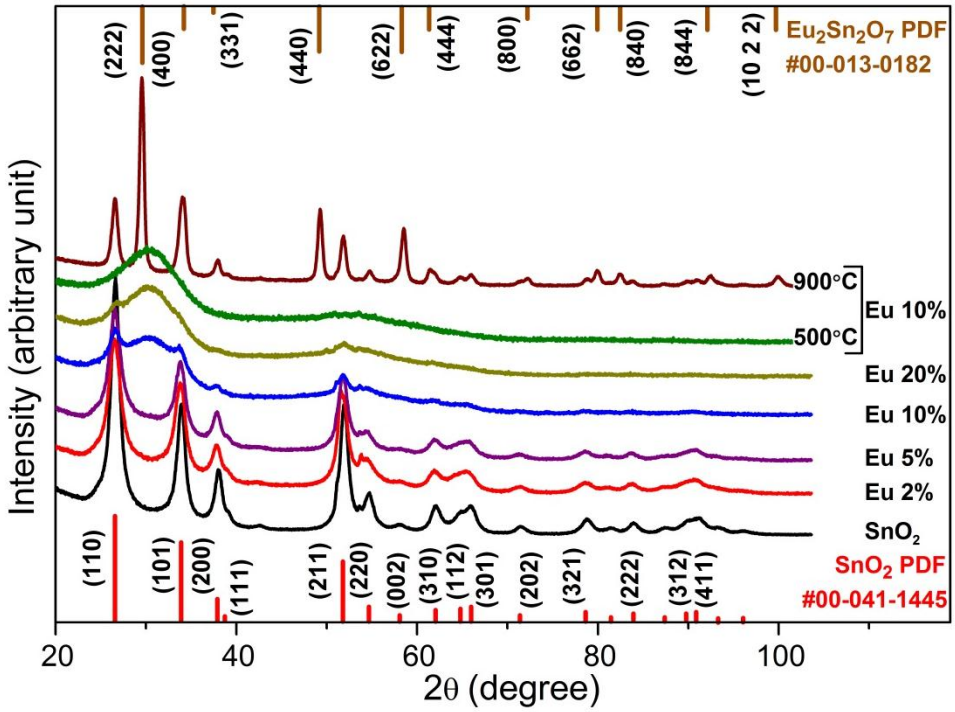

Figure 5.2 Glancing-incidence XRD patterns of the SnO_2 and Eu-doped films (Eu 2%, Eu 5%, Eu 10%, and Eu 20%), all obtained with post-annealing at 700°C, and of the Eu 10% films obtained with post-annealing at 500°C and 900°C.

To further investigate the nature of crystallinity of the nanocrystallites and the homogeneity of the Eu doping in these TO flms, we conduct TEM studies on selected Eu-doped TO films. The scanning TEM image of a thin cross-section of the Eu 2% film (prepared by focused ion beam microscopy) (Figure 5.3a) clearly shows the formation of TO nanocrystalline grains with an average size of 10 nm, which are present in the entire ~150 nm thickness of the film (Figure 5.1a). Closer examination of the voids inside the film shows an amorphous phase surrounding the nanocrystallites. The appearance of this amorphous matrix connecting the grains is consistent with the observation of fused grain morphology in the SEM images (Figure 5.1). Energy dispersive X-ray (EDX) analysis further reveals the presence of SiO_x layer on the chemically oxidized Si substrate. More importantly, EDX maps for the Sn, O, and Eu elements (Figure 5.3b) indicate a homogenous distribution of the Eu ions over both the crystalline and amorphous parts of the TO layer.

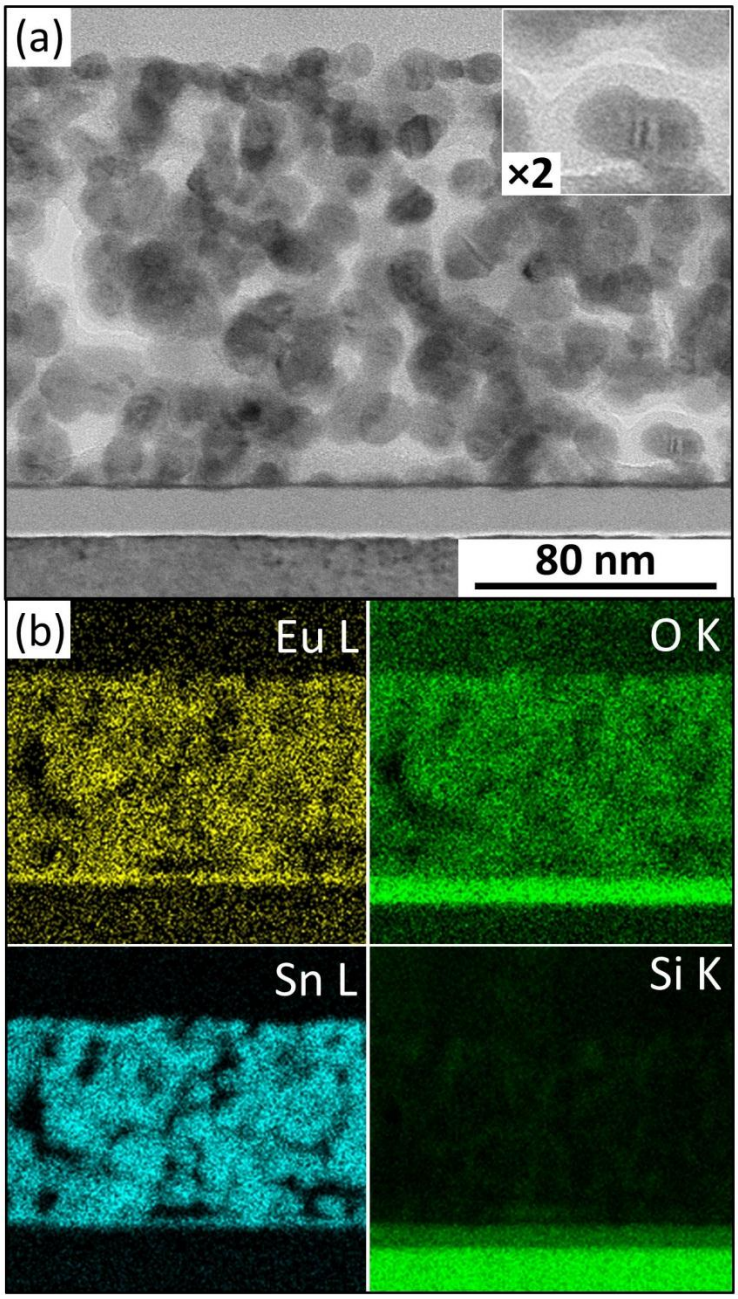

Figure 5.3 (a) Scanning TEM image, and (b) energy dispersive X-ray maps of Eu L, Sn L, O K, and Si K lines of a thin cross-section of the Eu 2% film prepared by focused ion beam microscopy. Inset shows a magnified view of nanocrystallites surrounded by an amorphous layer. [EDX maps are taken from the same region shown in (a), i.e. note the change in the scale].

Figure 5.4a shows the high-resolution TEM image of a thin cross section of the Eu 10% film obtained with T_{Anneal}=700°C (prepared by focused ion beam microscopy). In addition to the small (~6 nm) TO nanocrystallites (Figure 5.4a, yellow circle), other nanocrystallites of similar size (~3 nm) (Figure 5.4a, white oval) with a crystalline structure close to $Eu_2Sn_2O_7$ are also observed. The observed lattice spacings in this $Eu_2Sn_2O_7$ nanocrystallite is found to be 5.4 Å, in close agreement with the (111) interplane spacings (6.0 Å) for the reference pattern (PDF2#00-013-0182) given the poor crystallinity as observed in our GIXRD study (Figure 5.2). In particular, the observed minor difference could be due to distortions in the crystal structure as a result of stress exerted from the amorphous phase or of the small size of the nanocrystallites. Moreover, the corresponding EDX maps for the Sn, O and Eu elements (Figure 5.4b) also confirm that Eu is dispersed homogenously inside the TO grains. Furthermore, the Eu signal is found to extend in the small areas (marked by ovals) among the grains with a strong Sn signal, indicating the formation of a new phase with a relatively higher Eu concentration. This new phase could be assigned to $Eu_2Sn_2O_7$, as is observed in the smaller nanocrystallites (marked by oval) in the high-resolution TEM image (Figure 5.4a).

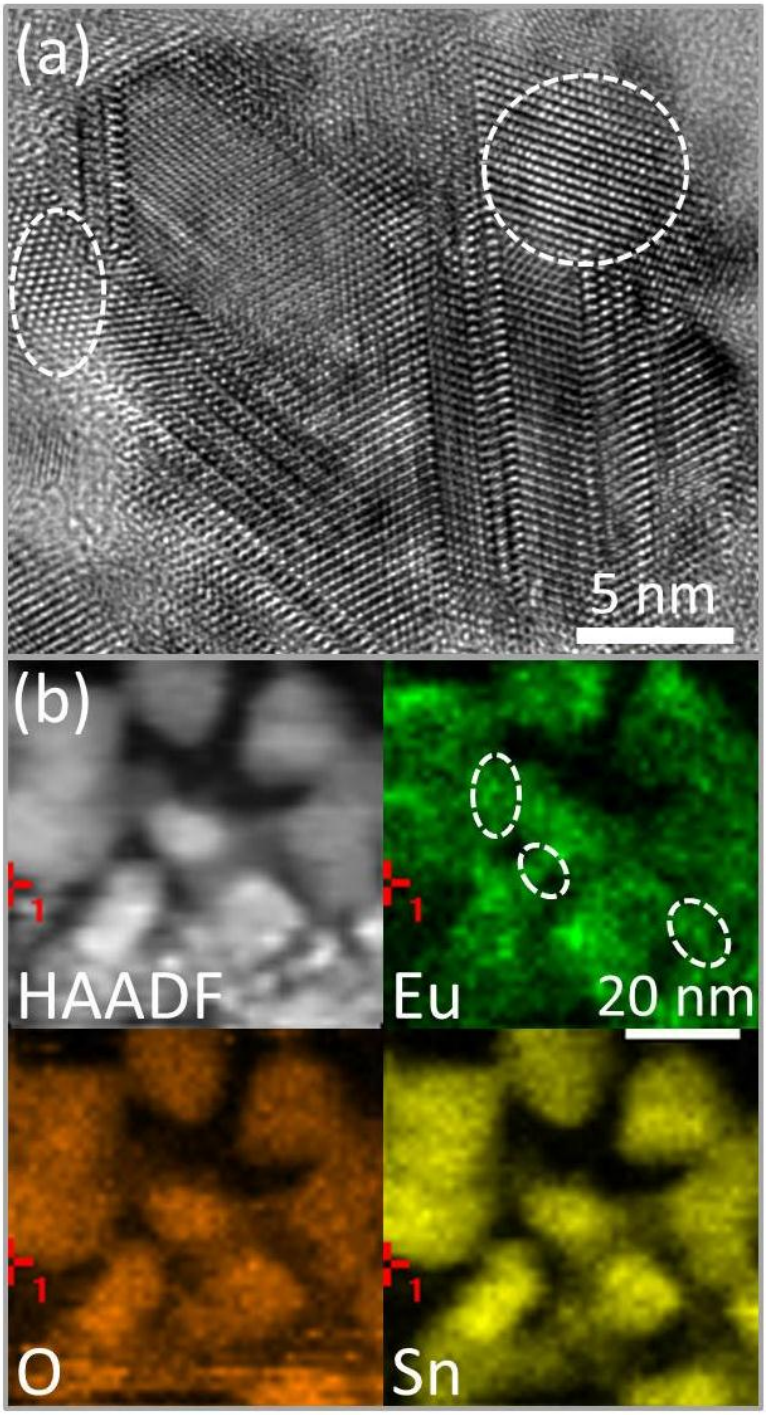

Figure 5.4 (a) High-resolution TEM image and (b) high angle annular dark field (HAADF) image and corresponding energy dispersive X-ray maps of Eu L, Sn L, O K lines of a thin cross section of the Eu 10% film (obtained with T_{Anneal}=700°C) prepared by focused ion beam microscopy. Circle and oval in (a) mark a SnO_2 and a $Eu_2Sn_2O_7$ nanocrystallite respectively, and ovals in (b) mark the presence of Eu between the Sn-rich grains.

Figure 5.5 shows the TEM image of the Eu 10% film prepared with T_{Anneal}=900°C , depicting the formation of considerably larger grains (20-25 nm) compared to those observed for the Eu 2% film (10 nm, Figure 5.3), in good accord with the GIXRD results (Figure 5.2). The corresponding EDX maps (Figure 5.5c) clearly reveal the phase separation between the Eu-deprived grains containing only Sn and O (marked as region 1, Figure 5.5a, inset) and the Eu-rich grains containing Sn, and O, as well as Eu (marked as region 2, Figure 5.5a, inset). Quantification results show 32 at. % Sn and 68 at. % O for region 1 and 20 at. % Eu, 20 at. % Sn, and 60 at. % O for region 2, confirming the respective stoichiometries of the SnO_2 and $Eu_2Sn_2O_7$ phases. Performing quantification on a stack of crystallites (region 3, Figure 5.5a, inset) give 5 at. % Eu, 28 at. % Sn, and 66 at. % O, which corresponds to a Eu-to-Sn mole ratio of 0.18, in comparison to that (0.11) for the 10% dopant concentration used for the precursor solution. especially considering the limited sampling size of a few grains. The high-resolution TEM image (Figure 5.5b) shows the atomic columns inside an Eu-rich crystallite with two sets of lattice spacings of 3.04 Å and 3.06 Å making a 70° angle, which can also be observed in the fourier transform of the grain (Figure 5.5b, inset). These observations are in good agreement with the cubic structure and the 3.01 Å lattice spacing of the (222) planes in the bulk $Eu_2Sn_2O_7$ phase (PDF2#00-013-0182). These results therefore definitively show that post-annealing at high T_{Anneal} (900°C) facilitates the formation of phase-segregated nanocrystallites (20-25 nm) of SnO_2 and $Eu_2Sn_2O_7$.

In summary, our TEM studies show that Eu is homogenously incorporated into both the crystalline and amorphous parts of the TO structure for Eu dopant concentration not greater 10% and T_{Anneal}=700°C. Increasing the Eu dopant concentration leads to the formation of a $Eu_2Sn_2O_7$ phase with poor crystallinity and small sizes (~3 nm). Phase separation of the $Eu_2Sn_2O_7$ phase from the SnO_2 phase is facilitated by increasing the T_{Anneal} to 900°C, leading to the formation of 20-25 nm nanocrystallites of SnO_2 and $Eu_2Sn_2O_7$.

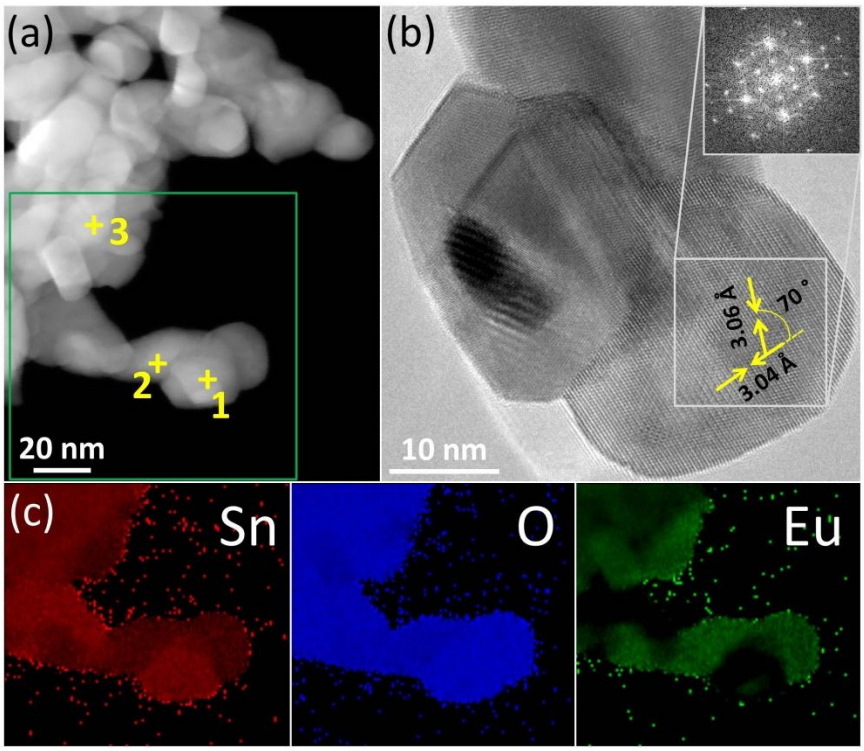

Figure 5.5 (a) Dark-field TEM image of the nanocrystallites scraped off from a Eu 10% film obtained with T_{Anneal}=900°C, and (c) the corresponding EDX maps of Sn L, O K, and Eu L lines over the region marked by the green box (inset) in (a) , and (b) high-resolution TEM image of the grains studied in the EDX mapping with the inset showing the Fourier transform of the box as marked in (b). Crosses in inset mark the EDX point quantification locations for the (1) Eu-deprived, (2) Eu-rich, and (3) stacked grain regions.

In order to investigate the chemical-state compositions of the doped TO films, we perform a comprehensive depth-profiling XPS study on the samples. Figure 5.6 shows typical XPS results for the Eu 2% film. The survey spectrum (Figure 5.6a) depicts that all the peaks are attributed to Sn, O and Eu, with no detectable impurity residual from the precursor solution. It should be noted that the minor carbonaceous layer observed on the as-prepared film due to sample handling in ambient conditions can be easily removed after mild Ar sputtering for 60 s. The Sn $3d_{5/2}$ peak at 487.4 eV for the as-prepared film is found to be shifted to 487.0 eV after 60 s sputtering and remains unchanged at 487.0 eV upon further sputtering (Figure 5.6e). The small shift (0.4 eV) observed upon sputtering the film for 60 s is due to the surface carbonaceous layer and the resulting change in the conductivity of the surface. The peak at 487.0 eV can be attributed to the Sn^{4+} state, in accord with our earlier study

and the reference spectra for SnO and SnO_2 powders.[97] The corresponding O 1s (Figure 5.6d) and Eu $3d_{5/2}$ peaks (Figure 5.6c) also exhibit a similar shift in the peak position after the first sputtering step, which can also be explained by the presence of carbonaceous layer. The O 1s peak for the as-prepared film is found to have two components with the intense peak at 531.3 eV and a weaker component at 532.9 eV. This higher binding energy component which is also observed for the undoped SnO_2 sample is attributed by Szuber et al.[89] to "chemisorbed oxygen" species on the surface of TO, as was also observed in our previous study.[97] After the first sputtering step (of 60 s), the O 1s peak is found to be at 530.9 eV and the higher binding energy component is removed (Figure 5.6d), confirming the surface-related nature of this component. Further sputtering for 240 s and 600 s does not affect the position and shape of the O 1s peak, indicating a homogenous oxide layer throughout the film (before reaching the Si interface).

The XPS spectrum of Eu is complicated due to the possible valence fluctuations between 2+ and 3+ oxidation states [115] and the resulting shake-down and shake-up satellite peaks.[116,117] For the as-prepared Eu 2% film, the intense Eu $3d_{5/2}$ peak at 1135.6 eV is observed along with a much weaker shake-up peak at 1144.3 eV[84] that persists upon sputtering. The lower binding energy Eu $3d_{5/2}$ peak at 1125.6 eV is only observed for the as-prepared film and is removed after sputtering for 60 s, suggesting a surface-related feature. This peak is assigned to the Eu^{2+} state, as is reported in earlier XPS studies of the trivalent compounds of Eu.[116,117] The presence of this 2+ state has been proposed to be the result of a spontaneous surface valence transition from the Eu^{3+} state due to change in the local density of states at the surface.[116,117] In the present work, however, we only observe this Eu^{2+} state for the as-prepared Eu 2% film, which is removed after just 60 s sputtering. The observed 2+ state is therefore likely not a final-state effect but a surface-related shake-down transition. . Furthermore, the intensities of the Eu $3d_{5/2}$ peaks at 1135.2 and 1144.3 eV are found to increase with increasing sputtering time (above 60 s), in contrast to that observed for Sn $3d_{5/2}$ and O 1s features. This could likely due to a lower preferential sputtering rate for the heavier Eu element than those of the lighter Sn and O elements.

The XPS spectra of Sn $3d_{5/2}$, O 1s, and Eu $3d_{5/2}$ regions for the other Eu-doped samples prepared with T_{Anneal}=700°C and 900°C are found to be similar to those of Eu 2% sample for both the as-prepared film and upon Ar sputtering. The relative intensities of the peaks are found to be different for different Eu-doped samples which will be discussed below. Using the fitted peak area as relative intensities and applying the appropriate relative sensitivity factors for Eu $4d_{5/2}$ (2.488), Sn $3d_{5/2}$

(4.725), and O 1s (0.711),[84] we estimate the relative chemical-state composition of Eu $4d_{5/2}$ for the four Eu-doped films prepared with T_{Anneal}=700°C for different sputtering steps. Because only the Eu $4d_{5/2}$ relative sensitivity factor is available, we estimate the corresponding Eu $4d_{5/2}$ intensity by applying an area ratio between the Eu $4d_{5/2}$ and Eu $3d_{5/2}$ peaks (1.45/1.84) to our fitted area for the Eu $3d_{5/2}$ peak (Figure 5.6a). Figure 5.6b shows the resulting depth profiles of Eu $4d_{5/2}$ and Sn $3d_{5/2}$ for all the Eu-doped films. Evidently, both the Eu $4d_{5/2}$ and Sn $3d_{5/2}$ profiles exhibit a sharp rise after 60 s and a plateau after 240 s of sputtering, as observed in our earlier work. This "plateau" value may be regarded as the actual dopant level of Eu in the TO film. Furthermore, the "plateau" values are found to be 2.7%, 3.6%, 5.3%, and 7.7 % for the Eu 2%, Eu 5%, Eu 10%, and Eu 20% samples, respectively, which shows a linear relation (R^2=0.9936, slope=0.28) to the initial concentration of Eu in the precursor solution. The latter relation will allow us to have a better control of the actual dopant level based on the Eu initial concentration. The obtained dopant levels for Eu in combination with the corresponding concentration of Sn (38.1 %, 36.9 %, 32.1 %, and 28.8 %) yield Eu-to-Sn ratio of 0.07, 0.10, 0.16, and 0.27 for the Eu 2%, Eu 5%, Eu 10%, and Eu 20% films respectively (Note the 0.16 ratio for Eu 10% sample is in good agreement with the obtained 0.18 ratio using EDX analysis above).

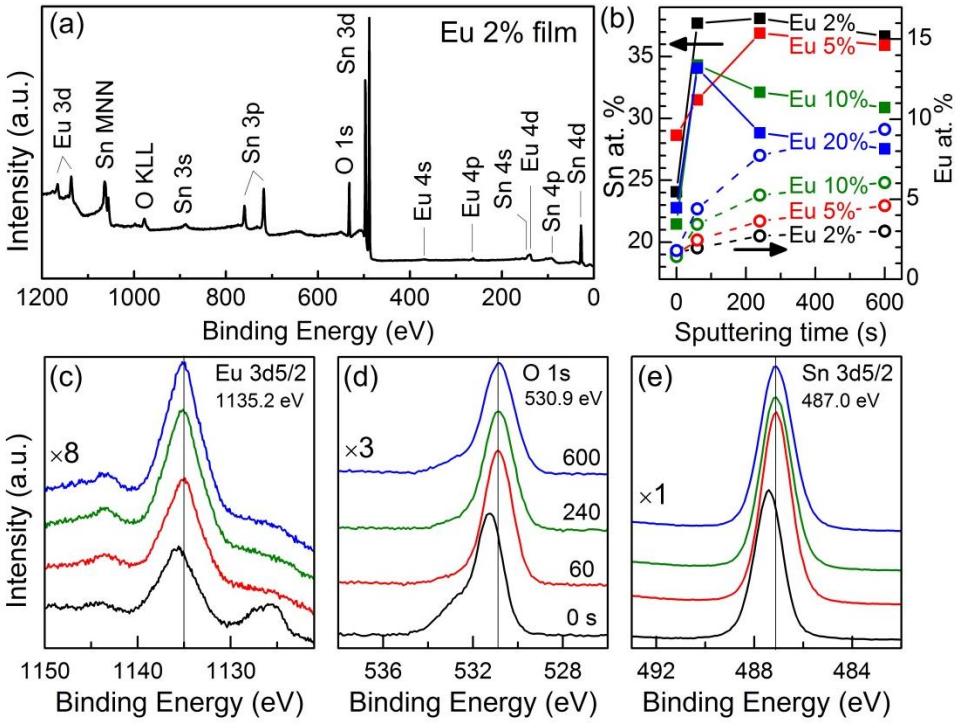

Figure 5.6 (a) Survey XPS spectrum after 240 s Ar sputtering, and XPS spectra of (c) Eu $3d_{5/2}$, (d) O 1s, and (e) Sn $3d_{5/2}$ regions for the Eu 2% film without and with 60 s, 240 s and 600 s of Ar sputtering. (b) Depth profiles of Sn $3d_{5/2}$ and Eu $4d_{5/2}$ for Eu 2%, Eu 5%, Eu 10% and Eu 20% films obtained with T_{Anneal}=700°C.

5.2 Photoluminescence Properties

The photoluminescence (PL) emission spectra of the Eu-doped SnO_2 films (Figure 5.7) exhibit two sets of features, including a broad emission band below 550 nm decorated with a number of peaks at 529 nm, 485 nm, 448 nm, 460 nm, and 422 nm, and two bands at 593 nm and 614 nm. By comparing these spectra with the PL spectrum of the SnO_2 film (i.e. without any Eu doping, Figure 5.7), which exhibits only the broad emission with weak peaks at 529 nm, 485 nm, 448 nm, and 422 nm, we assign the first set of features, except for the 460 nm peak, of the Eu-doped TO films to the nanocrystalline TO phase. The feature at 460 nm and the second set of peaks at 593 nm and 614 nm are only observed for Eu-doped films and are characteristic $^5D_2$-$^7F_0$, $^5D_0$-$^7F_1$ and $^5D_0$-$^7F_2$ emission bands of the Eu^{3+} ions.[16,68,118] Interestingly, the intensities of both the broad emission and the sharp peaks associated with the TO phase differ significantly for different dopant concentrations, and for the Eu

10% films obtained with different post-anneal temperatures (Figure 5.7). In particular, the intensities of the four sharp peaks observed below 550 nm appear to be higher for Eu 2% and Eu 5% films compared to those of SnO_2 film and they are very weak for the Eu 10% films (obtained with T_{Anneal}=700°C and 900°C). Remarkably, their intensities are greatly increased for the Eu 20% film and for the Eu 10% film obtained with T_{Anneal}=500°C (note the 1/40 change in scale for the latter in Figure 5.7). These results suggest that these four sharp peaks below 550 nm are related to disorder in the structure, which are expected to increase by increasing the Eu concentration and by reducing the post-anneal temperature. For the Eu 10% film obtained with T_{Anneal}=700°C, the intensities of these four peaks are discernibly reduced. The initial formation of the poorly crystalline Eu-rich phase in this film (Figure 5.2) therefore appears to quench the TO-related emission centres.

In general, the appearance and relative intensities of the two characteristic peaks of Eu reflect the symmetry of the lattice sites occupied by the Eu ions in the TO structure.[16,68,118] For the Eu 2% film, the 593 nm band is stronger than the 614 nm band, indicating that the majority of the Eu^{3+} ions occupy lattice sites with inversion symmetric, which correspond to the cationic site with C_{2h} symmetry of the TO structure (and not to, e.g., interstitial sites). On the other hand, for the Eu 5%, Eu 10% and Eu 20% films obtained with T_{Anneal}=700°C, the 614 nm band is stronger than the 593 nm band, indicating that Eu^{3+} is occupying substitutional sites with no inversion symmetry. These non-centrosymmetric sites could be found in interstitial sites, in the amorphous phase, or could be due to disturbance of the symmetric cationic sites by increase in the defect density. These defects are due to substitution of the bigger trivalent Eu^{3+} ion instead of quadravalent Sn^{4+} ion, which causes distortions in the lattice structure and also create oxygen vacancies.[16] The Eu 10% film obtained with T_{Anneal}=500°C also shows a stronger 614 nm band and with a higher absolute intensity than all the other films (note the 1/10 scaling factor), while the Eu 10% film obtained with T_{Anneal}=900°C exhibits much weaker Eu emission peaks, with a stronger 593 nm band. This intensity variation shows that the amorphous structure in the former film promotes luminescence of Eu ions while the $Eu_2Sn_2O_7$ nanocrystallites in the latter film greatly suppress Eu emission.

We also collect the corresponding excitation spectra for the characteristic Eu^{3+} emission bands at 593 nm and 614 nm for all the films. Figure 5.7b shows a strong broad band in the UV region (< 330 nm) for all the films, which could be attributed to the optical absorption of the TO phase,[67,119] consistent with the absorption edge observed between 3.9 eV (317 nm) and 3.7 eV (335 nm) for 4-12 nm pristine TO nanocrystallites.[120] Moreover, the intensity of this broad band appears to increase by

increasing the Eu concentration and decreasing T_{Anneal}, indicating that the energy transfer from TO structure to Eu is enhanced by the corresponding decrease in the nanocrystallite sizes and increase in the amounts of defects in the TO structure. For the Eu 20% film obtained with T_{anneal}=700°C and the Eu 10% film obtained with T_{Anneal}=500°C (Figure 5.7b), we also observe an additional peak at 470 nm and 455 nm for the emission bands at 614 and 593 nm, respectively. These sharp peaks at 470 nm and 455 nm are assigned to direct excitation of the f-f transitions in Eu^{3+} ions.[67,121] The nearly constant excitation spectra of Eu 10% film obtained with T_{Anneal}=900°C is suggesting that the energy transfer from TO to Eu^{3+} is disrupted due to the phase separation and the Eu^{3+} in the large nanocrystallites of $Eu_2Sn_2O_7$ does not show any fluorescence properties.

The energy transfer from TO structure to Eu^{3+} is observed to be greatly affected by two correlated factors: size of the crystallites and the defect density. Decreasing the size of nanocrystallites, i.e. increasing the defect density, improves the energy transfer from TO structure to Eu and increases the 614 nm emission intensity. This increased emission intensity at 614 nm is also accompanied with increase in the defect-related emissions below 550 nm, which are remarkably strong for Eu 20% film and Eu 10% film obtained with T_{Anneal}=500°C. These defect-related emissions are however, quenched for the Eu 10% film obtained with T_{Anneal}=700°C due to a structural transition where the poorly crystalline $Eu_2Sn_2O_7$ phase emerges. These results show that Eu 10% films obtained with T_{Anneal}=700°C and 500°C are of great interest, where the former has an intense pure characteristic Eu^{3+} emission band, 614 nm, and the latter has the most intense emissions for both characteristic Eu^{3+} band and defect-related bands below 550 nm.

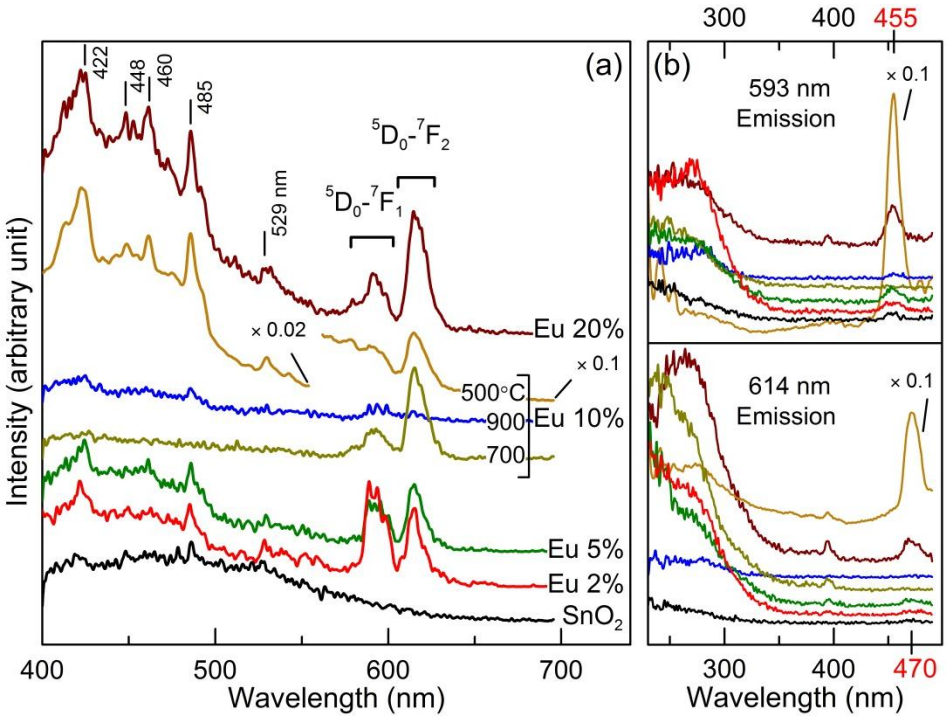

Figure 5.7 (a) Photoluminescence emission spectra of the pristine and Eu-doped TO samples obtained with excitation wavelength 300 nm. (b) The excitation spectra of the samples (with the same color coding of the emission spectra) for emission wavelengths of 614 nm (bottom), and 593 nm (top) corresponding to the magnetic dipole ($^5D_0$-$^7F_1$) and electric dipole ($^5D_0$-$^7F_2$) transitions of Eu^{3+} ions, respectively.

5.3 Magnetic Properties

Magnetization of the pristine and Eu-doped samples deposited on Si substrates are measured (with an applied magnetic field of 6kOe) as a function of temperature, and the results are shown in Figure 5.8. Due to the diamagnetic properties of Si and SnO_2, a negative magnetization is observed for all the samples at room temperature. For the SnO_2 and Eu 5% films, magnetization remains constant for the entire temperature range of 4-300 K, while the samples with higher Eu concentrations (Eu 10% and Eu 20% films) show a Curie-Weiss transition at 57 K and 65 K, respectively, leading to an increase in the magnetization of the sample. These ferromagnetic (FM) transitions are followed by antiferromagnetic (AFM) transitions at 47 K and 53 K, which lead to appearance of a weak peak for the Eu 10% film and a strong peak for the Eu 20% film (Figure 5.8). The observed peak due to these

consecutive transitions is followed by an increasing magnetization, where the Eu 10% film exhibits a steeper increase than that of the Eu 20 % film. In order to determine the source of this magnetic behavior, magnetization of the Eu 10% film obtained with T_{Anneal}=900°C, which contains highly crystalline phase-separated grains (Figure 5.5), is also measured. This film also shows a similar behavior with a Curie-Weiss transition at 57 K and a Neel transition at 46 K giving rise to a strong peak, which is followed by a slightly increasing magnetization similar to that observed for the Eu 20% film. The zero-field cooled (ZFC) and field cooled (FC) magnetization curves measured for the Eu 10% film obtained with T_{Anneal}=700°C (Figure 5.8, inset) show a higher magnetization for the ZFC curve, while both ZFC and FC curves follow a similar trend.

These magnetic transitions are caused by the $Eu_2Sn_2O_7$ phase, which starts to appear in the Eu 10% film (obtained with T_{Anneal}=700°C). The pronounced magnetic behavior for the Eu 20% film can be explained by increase in the amount of this phase for the Eu 20% film compared to the Eu 10% film, as shown by the increase in the intensity of the broad peak corresponding to this phase in our GIXRD results (Figure 5.2). The appearance of these transitions in the Eu 10% film obtained with T_{Anneal}=900°C) further confirms that not only the magnetic behavior is originating from the $Eu_2Sn_2O_7$ phase, but also it can be readily observed for the highly crystalline grains of this phase, where they are completely separated from the TO crystallites (Figure 5.5). Apparently, this behavior is not caused by the presence of numerous defects and vacancies in the structure. The $Eu_2Sn_2O_7$ phase with a cubic pyrochlore structure belongs to a family of geometrically frustrated magnetic materials, where the AFM ordering of the magnetic rare earth ion on their triangular (tetrahedral) sublattice units is "frustrated" due to geometry.[122] In the $Eu_2Sn_2O_7$ phase, however, Eu has an oxidation state of 3+, as dictated by the formula and observed in our XPS studies (Figure 5.6) and therefore it does not have any magnetic moment, where the spin and orbital angular momenta cancel each other and lead to a total angular momentum of zero. The observed magnetic ordering in this material, however, suggests that a net non-zero total angular momentum for Eu^{3+} exists in this phase. The presence of defects and vacancies in the structure is found to shift both magnetic transition temperatures. These shifts are likely due to the increased disorder and more importantly the variations in the carrier concentration of the material, which play a key role in magnetic couplings. Recovery of the FM ordering by decreasing the temperature could also be attributed to reduction in the carrier concentration upon decreasing the temperature, due to temperature dependence of the carrier activation from donors in the structure, which in turn affects the magnetic coupling of the system. The similar ZFC and FC behaviors with the higher magnetization observed for the ZFC curve also reveals that there is no "spin

glass" behavior and a better FM ordering is achieved upon magnetizing the phase with no AFM order.[122]

These magnetic studies show the formation of FM and AFM orderings in the nanocrystallites of $Eu_2Sn_2O_7$ phase for the first time. These interesting magnetic properties most likely occur due to ordering in the Eu^{3+} ions that have gained a non-zero total angular momentum. Further investigations are required to better understand the origin of these magnetic orderings.

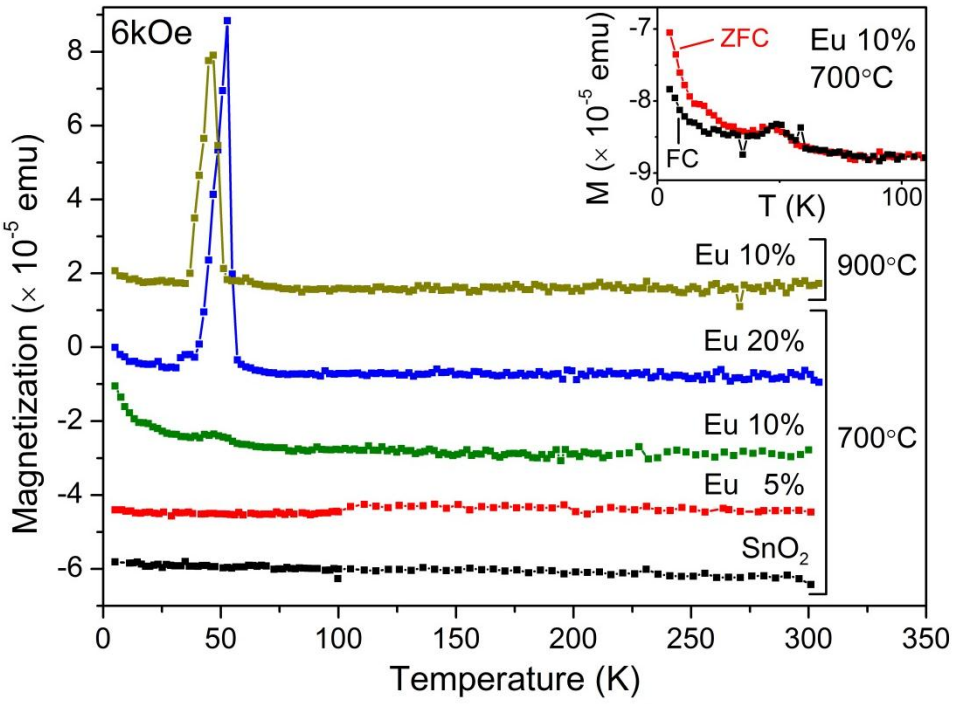

Figure 5.8 Magnetization measurement of the pristine and Eu-doped TO films deposited on Si in the 4-300 K temperature range. Inset shows the zero-field cooled (ZFC) and field cooled (FC) magnetization measurement results on the Eu 10% film obtained with T_{Anneal}=700°C.

5.4 Conclusions

Nanocrystallites of TO are doped homogenously with Eu^{3+} ions at 2.7-7.7 atomic percentages, as determined from XPS results. The incorporation of Eu^{3+} ions in the TO structure is found to suppress the growth of the nanocrystallites, which leads to decrease in the crystallite size and formation of amorphous TO phase for the low doping levels (as in the Eu 2% and Eu 5% films) and to formation

of a poorly crystalline $Eu_2Sn_2O_7$ phase for the high doping levels (as in the Eu 10% and Eu 20% films). The majority of Eu^{3+} ions occupy centrosymmetric cationic substitutional sites for the Eu 2% sample leading to an intense 593 nm emission, while for the Eu 5%, Eu 10%, and Eu 20% samples, non-symmetric site substitution dominates with the emission at 614 nm. Increasing the Eu concentration and decreasing the T_{Anneal}, decrease the size of nanocrystallites and increase the defect density, which result in an increase in the 614 nm emission and in the defect-related emission below 550 nm. The Eu 10% film obtained with T_{Anneal}=700°C shows a predominant characteristic Eu emission at 614 nm, and the defect-related emissions appear to be all quenched due to structural transition and the emergence of the $Eu_2Sn_2O_7$ phase. The Eu 10% film obtained with T_{Anneal}=500°C, on the other hand, has the strongest emission in both the Eu emission band at 614 nm and the defect-related band below 550 nm. The observed photo-induced emissions show great promises for UV-to-visible light conversion in the otherwise highly transparent Eu-doped TO films. Interestingly, in spite of the non-magnetic nature of Eu^{3+} ions, a ferromagnetic transition followed by an antiferromagnetic transition are observed in the Eu 10% films obtained with T_{Anneal}=700°C and 900°C and in the Eu 20% film obtained with T_{Anneal}=700°C upon formation of the $Eu_2Sn_2O_7$ phase. These magnetic orderings are reported for the first time in this cubic pyrochlore structure. The corresponding transition temperatures apparently depend on the doping concentration and T_{Anneal}, which can be attributed to the effect of defects and to carrier concentration in the magnetic couplings that cause these FM and AFM magnetic orderings. These results therefore illustrate the intricate luminescence and magnetic properties of Eu-doped nanocrystalline TO films upon structural changes induced by incorporating high Eu doping levels in the nanocrystalline TO films obtained by our simple spin-coating method.

Chapter 6

Catalyst-assisted Pulsed Laser Deposition of Tin (IV) Oxide single-crystalline nanostructures: VS or VLS growth of nanoparticles, nanobricks, nanowires, and nanobelts

In this chapter, we show the results of the deposition of TO nanostructures using PLD method, and we discuss the effect of deposition parameters on morphology, crystallization, and growth mechanism of TO nanostructures. We also show the effect of depositing Au, as a catalytic seed layer on the substrate, in obtaining 1D TO nanostructures by PLD. The deposition system and also details of the nanostructure fabrication using PLD method are described in Chapter 2 (fabrication systems).

6.1 Nanostructure Morphology

Figure 6.1a shows the HIM images of a typical TO film PLD-grown at 700°C for 60 min in 400 mtorr of Ar on a H-Si substrate without gold nanoislands (GNI's), hemispherical gold particles on the substrate. A closely packed granular morphology with a grain size of 50-70 nm is observed while faceted nanostructures only become evident with HIM imaging. Similar morphology with a discernibly larger grain size (50-100 nm) is also found for the film grown in 400 mtorr of O_2 on an ox-Si substrate without GNI's (Figure 6.1b). Furthermore, the granular film morphology remains unchanged for deposition on an ox-Si substrate in 400 mtorr of Ar (not shown). The generally larger grain size found for the ox-Si substrate suggests better TO adhesion on ox-Si during PLD growth.

Figure 6.1c and 6.1d show the SEM images of typical GNI templates supported on a H-Si and an ox-Si substrates, respectively, which are used to guide the growth evolution and to control the morphology of the TO nanostructures during the PLD growth. Evidently, GNI/H-Si appears to exhibit a broader Au nanoisland size distribution than GNI/ox-Si. The formation of Au silicide is expected to proceed more readily on a H-Si than an ox-Si substrate,[80] which causes the GNI's to adhere more strongly to and therefore less likely to be lifted off H-Si than ox-Si substrate. In order to investigate the effects of different processing gases, we deposit TO nanostructures on the two supported GNI templates in 400 mtorr of O_2 and of Ar. In particular, faceted nanostructures containing nanobricks with distorted tetragonal shapes and nanogravels, faceted nanostructures with no regular shape, with more tile-like shape are observed for the highly crystalline TO films PLD-grown in O_2 on both GNI/H-Si and GNI/ox-Si templates (Figure 6.1e, 6.1f). The observed

nanobricks (approximately 100×100×500 nm^3 in size) and nanogravels (200×200 nm^2 in area) are found to be considerably larger than the granular structures in the TO films PLD-grown on the substrates without GNI's (Figure 6.1a, 6.1b), suggesting that the GNI's function as an effective catalyst. In a slice-and-view study using a focused ion beam SEM system, we observe that the large faceted nanostructures grow on top of the GNI's, which remain in contact with the substrate (Appendix A.4). Although the growth begins with nucleation on the GNI sites, further evolution towards the faceted nanostructures appears to follow a vapor-solid growth mechanism, leading to almost total covering of the GNI's by the TO nanostructures on top. As reported for vapor-solid growth mechanism in earlier studies,[44] the presence of a catalyst can change the surface energy of crystalline planes of the nanostructures. This is in good accord with the present observation that the supported GNI templates act as a catalyst and promote the growth of single-crystalline, faceted TO nanobricks and nanogravels in the PLD process.

On the other hand, the nanostructured TO films PLD-grown in Ar on GNI/H-Si (Figure 6.1g) and GNI/ox-Si templates (Figure 6.1h) are found to be notably different from each other and from those PLD-grown in O_2 (Figure 6.1e, 6.1f). In particular, faceted cuboid nanostructures terminated with square pyramids are preferentially grown on the GNI sites and not on the bare areas of the H-Si substrate, leading to the formation of discrete nanoparticles instead of a continuous film (Figure 6.1g). The formation of these highly crystalline, faceted nanoparticles therefore follows a similar catalyst-assisted vapor-solid growth mechanism as observed for nanobricks. With the exception of those nanoparticles that grow into one another, the discrete nanoparticles appear to be quite uniform in size (with ~200 nm edge length). Remarkably, the film PLD-grown on GNI/ox-Si in Ar (Figure 6.1h) exhibits prominent nanospike structures with GNI on top. The nanospikes are found to be randomly oriented and have multiple facets along their 200-500 nm length. The presence of GNI's on top of the nanospikes is indicative of a different mechanism involving VLS growth, commonly found for 1D nanostructure growth in CVD-like processes. Furthermore, a limited number of faceted cuboid nanostructures similar to those obtained on GNI/H-Si in Ar (Figure 6.1g) are also observed, along with smaller grains among the nanospikes and cuboid nanoparticles. The coexistence of the vapour-solid growth mode operative for these latter nanostructures with the VLS growth mechanism found for the nanospikes highlights the complexity of this growth process.

Figure 6.2a and 6.2b show the SEM images of 1D TO nanostructures PLD-grown on a GNI/ox-Si template, with an average nanoisland size of 50 nm, in 400 mtorr of Ar for 90 min at lower substrate

temperatures of 600°C and 500°C, respectively. Unlike the case of nanoparticles (Figure 6.1g) and nanobricks (Figure 6.1e, 6.1f) but similar to that found for the nanospikes (Figure 6.1h) grown at 700°C, the GNI's are found to detach from the substrate and they stay on top of the growing nanostructures, as clearly illustrated in the SEM back-scattered electron images at a higher magnification (Figure 6.2c, 6.2d), revealing a VLS growth mechanism for these nanostructures. The nanowires PLD-grown in Ar at 600°C have a nearly square-shaped cross-section, the size of which reduces from 70-90 nm side length at the base to 15-50 nm side length at the tip along their typical 1-5 μm length (Figure 6.2c). It should be noted that the length of the nanowires can be easily extended with a longer deposition time. The corresponding high-magnification HIM image for the nanowires (Figure 6.2e) further reveals a layered structure on their side surfaces, suggesting layer-by-layer growth consistent with the VLS growth mechanism. The conversion from the dome-shaped Au nanoislands to more spherical nanodroplets with increasing deposition time reduces the active area for the VLS growth and causes reduction in the nanowire cross section, resulting in the observed smaller nanowire cross section at the tip than the diameter of the Au nanodroplet. The larger cross-section found at the base of nanowires in comparison to that at the GNI tip could also be due to vapor-solid growth occurring concurrently, as observed in the formation of nanobricks and nanoparticles. In particular, as the nanowires grow longer, more vapour-to-solid deposition occurs around the side surfaces of the nanowires, causing tapering from the base area with a longer exposure to the tip area with a shorter exposure. On the other hand, the nanobelts PLD-grown in Ar at 500°C, as clearly shown in the HIM image (Figure 6.2f), have a distinctly rectangular cross-section, with a typical thickness of 5-30 nm and width of 30-70 nm, giving an aspect ratio of 2-9. Unlike the 1-5 μm long nanowires, these nanobelts appear to grow to tens of micrometers in length. Like the nanowires, the cross sections of the nanobelts also reduce along the length gradually (which is most notable within 1 μm from the tip) and appear smaller than the Au droplet, which can also be explained by the aforementioned explanations offered for the nanowires. Since the nanobelts and nanowires have a general rectangular cross section and grow symmetrically perpendicular to this cross section, the deposition temperature (500°C for nanobelts, 600°C for nanowires) is therefore the key parameter that controls the growth rate leading to the observed differences in their shapes and lengths. The growth rate in the VLS mechanism is governed by the pseudo-binary phase diagram of TO and the Au catalyst, in which the temperature directly affects the eutectic phase transition of the supersaturated liquid leading to precipitation and growth of the nanostructure in the VLS growth mechanism.[56] The lower growth temperature also appears to affect the growth rates along different

planes, the difference of which creates the rectangular cross sectional shape for the nanobelts (This effect will be discussed more in the TEM section).

In addition to the effect of the deposition temperature, we also investigate the effects of the size of GNI catalysts on the PLD growth of these nanostructures. The average size of the GNI's formed on a Si substrate can be controlled by adjusting the thickness of the deposited Au film and the post-annealing temperature, as described in detail by Sohn et al..[80] Figure 6.3a and 6.3b show the HIM images of two GNI/ox-Si templates with near-Gaussian GNI size distributions and average GNI sizes of 50 nm and 10 nm , respectively, and the corresponding nanostructures PLD-grown in 400 mtorr of Ar for 90 min at 500°C on these GNI templates. In spite of the smaller dimensions of these nanostructures obtained on the 10 nm GNI template (Figure 6.3d) compared to those grown on the 50 nm GNI template (Figure 6.3c), high-resolution HIM is capable of revealing their distinct nanobelt morphology, with the characteristic rectangular cross sections. These nanobelts have a generally smaller cross section but still show a width-to-thickness ratio similar to the nanobelts PLD-grown using the 50 nm GNI template. The nanobelts deposited on the 10 nm GNI's (Figure 6.3d) are found to be shorter (1-2 μm in length) than those on the 50 nm GNI's (10-30 μm in length), and they exhibit a more vertical orientation with respect to the substrate. The 10 nm GNI template (Figure 6.3b) also has a higher GNI aerial density than the 50 nm GNI template (Figure 6.3a), which leads to a correspondingly higher density of and therefore smaller spacings among the nanobelts. The increase in the aerial density with the correspondingly smaller size of the GNI's reduces the overall amount of the TO vapour absorbed by each GNI, which therefore leads to a shorter nanobelt length. The present result therefore shows that the size and distribution of the GNI catalysts can effectively control the cross-sectional dimension (Note that only temperature controls the width-to-thickness ratio), longitudinal growth rate and the aerial density of the deposited 1D TO nanostructures prepared using this catalyst-assisted PLD method. This type of control is possible because of the VLS growth mechanism occurring at the catalyst location that is responsible for the growth of these 1D nanostructures.

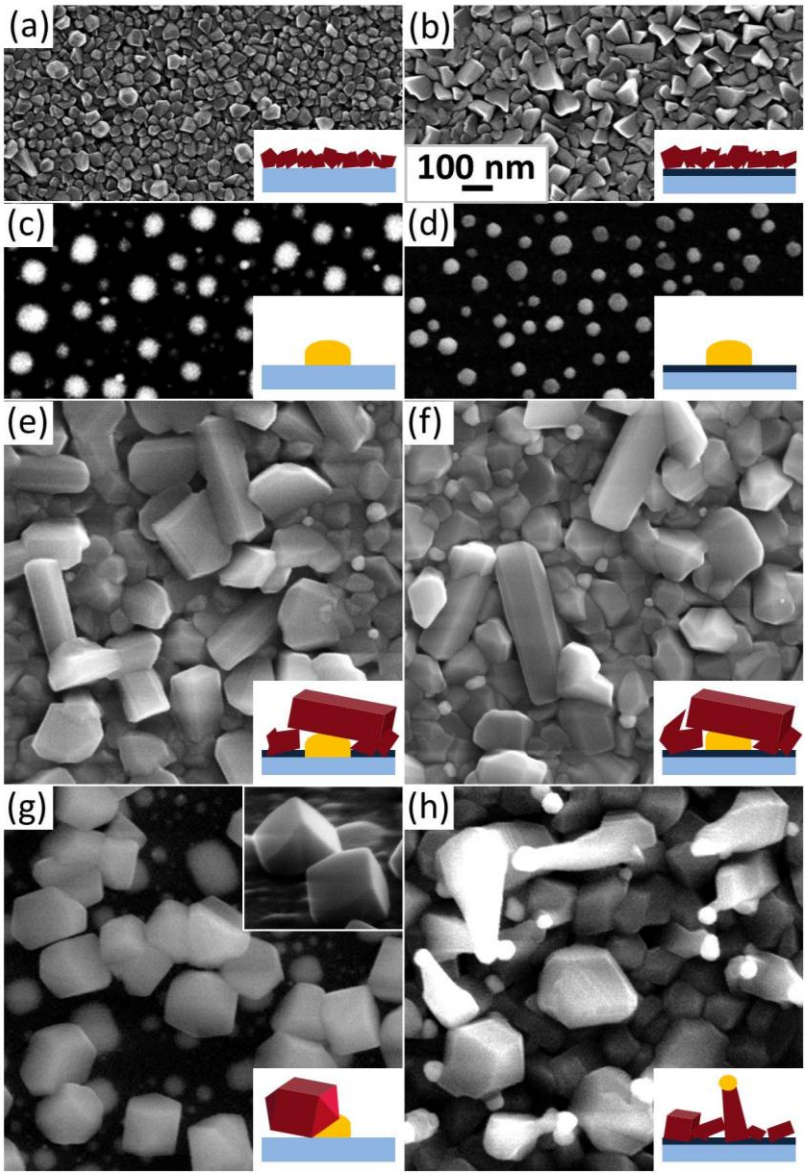

Figure 6.1 HIM images of typical TO films deposited on (a) a H-Si substrate in 400 mtorr of Ar and (b) an ox-Si substrate in 400 mtorr of O_2, all at 700°C and SEM images of gold nanoislands (GNI's) on (c) a H-Si substrate (GNI/H-Si) and (d) an ox-Si substrate (GNI/ox-Si), and of the TO nanostructures deposited on (e) a GNI/H-Si and (f) a GNI/ox-Si templates in 400 mtorr of O_2, and on (g) a GNI/H-Si and (h) a GNI/ox-Si templates in 400 mtorr of Ar, all at 700°C. Top inset in (g) corresponds to a SEM image collected at 70° tilt. Lower insets schematically show the GNI/H-Si and GNI/ox-Si templates and the PLD-grown TO nanostructures on the H-Si and ox-Si substrates with and without GNI's.

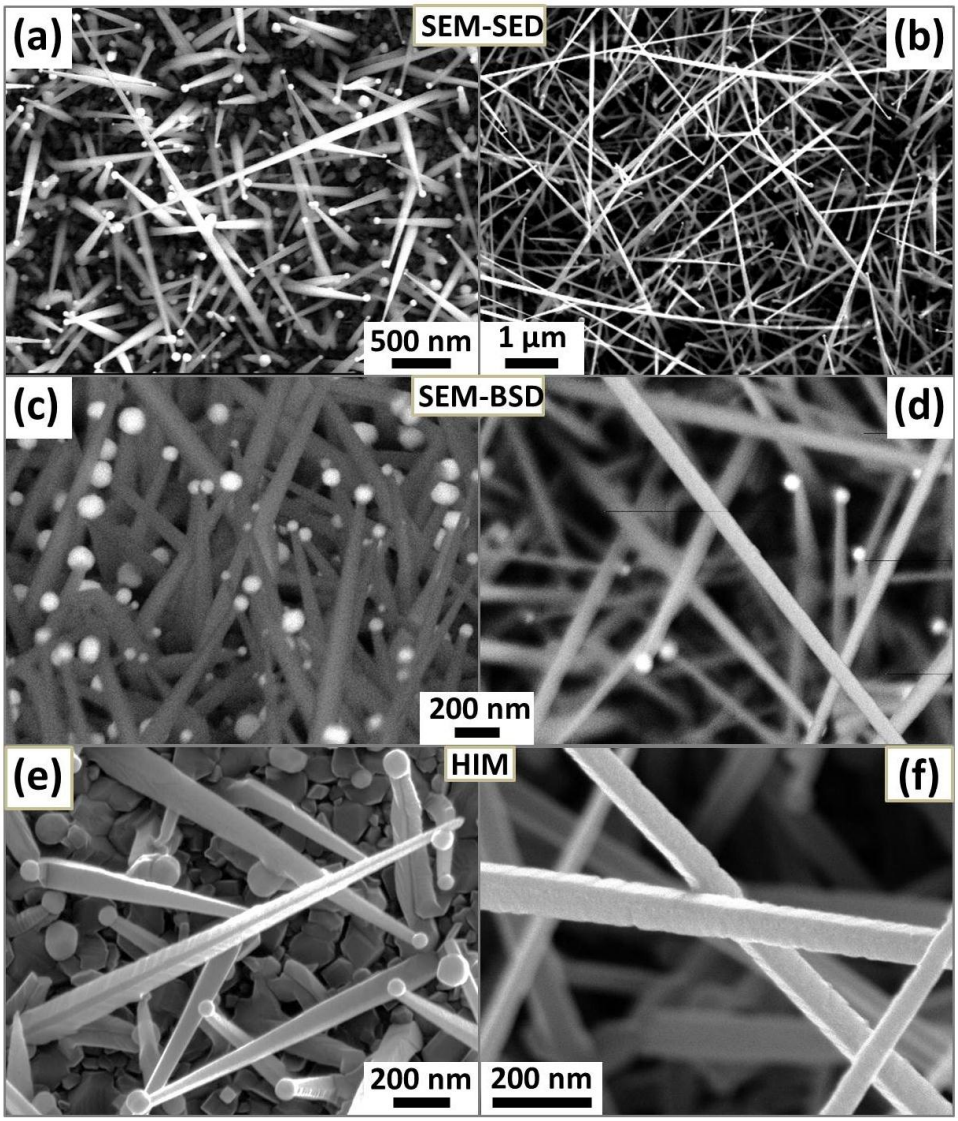

Figure 6.2 SEM images of (a) nanowires and (b) nanobelts, PLD-grown on an GNI/ox-Si template in 400 mtorr of Ar at 600°C and 500°C respectively, collected by using the in-lens secondary electron detector (SED), and by using the back-scattered electron detector (BSD) with a higher elemental contrast at a higher magnification for (c) nanowires with a 70° tilt and (d) nanobelts. HIM images collected at a higher magnification for (e) nanowires and (f) nanobelts.

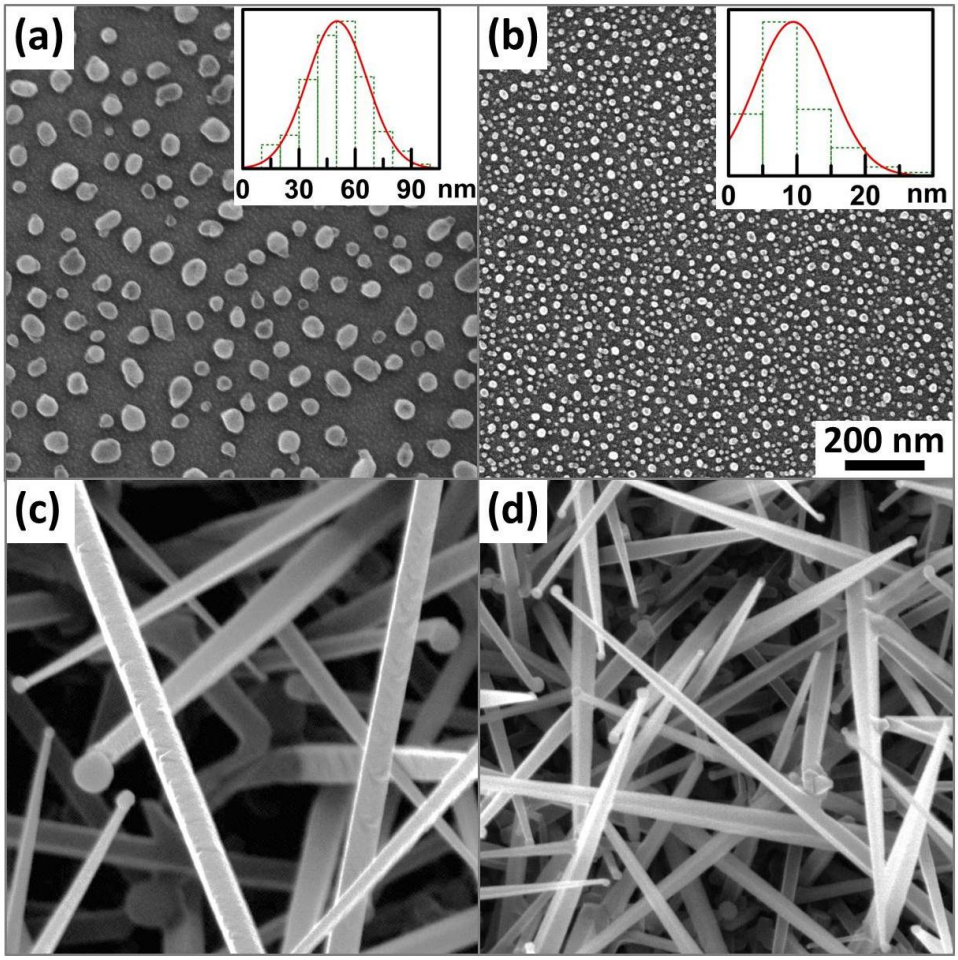

Figure 6.3 HIM images of the gold nanoislands (GNI's) prepared on ox-Si substrates with average diameters of (a) 50 nm, and (b) 10 nm, and Gaussian size distributions (insets), and the HIM images of the nanobelts (c) and (d) PLD-grown in 400 mtorr of Ar at 500°C on GNI/ox-Si templates shown in (a) and (b), respectively.

6.2 Crystal Structure Characterization Using X-ray Diffraction

Figure 6.4 shows the corresponding GIXRD patterns of the aforementioned TO nanostructured films with predominant nanobricks and nanogravels (Figure 6.1f), nanoparticles (Figure 6.1g), nanowires (Figure 6.2a), and nanobelts (Figure 6.2b). Evidently, in addition to the observed crystalline peaks of the fcc phase of Au (PDF2 #00-004-0784), a single tetragonal phase of SnO_2 (PDF2 #00-041-1445) is observed for all the nanostructures. These results show that the different growth conditions, particularly deposition in an Ar atmosphere, have not created a second crystalline

phase in these nanostructures, which verifies that the stoichiometry of the SnO_2 target is preserved in the PLD growth of all the deposited nanostructures. In spite of the nanometer size of these nanostructures, the observed peak widths are within the instrumental resolution, indicative of the high level of crystallinity with minimal strains in these nanostructures. Of particular interest are the remarkably different relative peak intensities, most notably for the prominent diffraction peaks, found for the different TO nanostructures shown in Figure 6.4. With respect to the reference pattern for SnO_2 powders (PDF2 #00-041-1445), the differences in the relative intensities for different PLD-grown nanostructures show that they all have a preferred growth orientation: (101) for nanoparticles and nanobricks, (200) for nanowires, and (200) and (101) for nanobelts (Figure 6.4). We summarize the intensities of (101) and (200) peaks relative to the (110) peak (the most intense peak in the reference pattern) for different nanostructures in Table 6.1. Evidently, the intensity ratios for (101) to (200) for the nanoparticles (7.9) and nanobricks (5.0) and for the nanowires (2.3) and nanobelts (2.2) are, respectively, larger and smaller than that of the reference (3.6). Moreover, nanobelts show a high intensity ratio (0.98) for the (101) peak relative to (110) peak, while the nanowires exhibit a smaller ratio (0.65) than that of the reference (0.75). These results show that the differences in the morphology of the nanostructures obtained by modifying the deposition parameters are caused by changes in the crystalline growth orientations of these nanostructures.

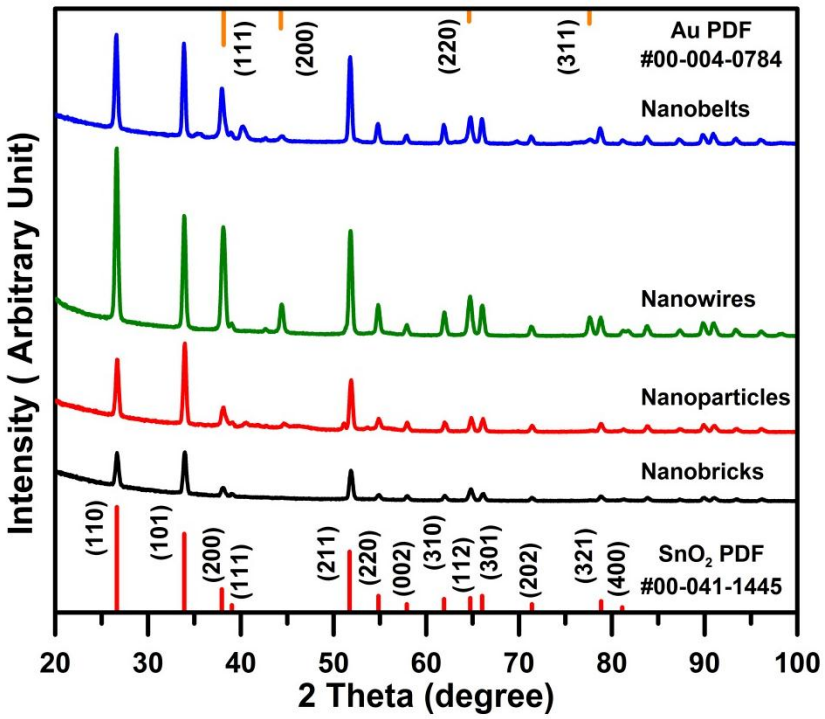

Figure 6.4 Glancing-incidence XRD patterns of different TO nanostructures obtained at an incidence angle of 0.3°. The PDF2 reference patterns of the tetragonal phase of SnO_2 powders (#00-041-1445) and fcc phase of Au (#00-004-0784) are shown as bottom and top bar graphs respectively.

Table 6-1 Comparison of the intensities of different peaks relative to (110) for the GIXRD patterns of different predominant TO nanostructures to those of the reference pattern for SnO_2 powders (PDF2 #00-041-1445).

SnO_2 Nanostructures	Peak Intensity Relative to (110)	
	(101)	(200)*
Reference Pattern PDF2 #00-041-1445	0.75	0.21
Nanoparticles	1.43	0.18
Nanobricks	1.31	0.26
Nanowires	0.65	0.28
Nanobelts	0.98	0.44

6.3 Transmission Electron Microscopy of 1D Nanostructures

Typical low-resolution TEM images, along with their selected area electron diffraction (SAED) patterns, obtained for nanowires and nanobelts are shown in Figure 6.5. For a straight section of the nanowire without any sign of mechanical bend or twist (Figure 6.5a), the corresponding SAED pattern reveals a growth direction perpendicular to the (200) plane, i.e. along the length of the nanowire in the [100] direction. The crystalline orientations in this nanowire inferred from the SAED pattern are also shown schematically using a ball-stick model of the SnO_2 unit cell in Figure 6.5a. Moreover, it is revealed that the nanowire has the (010) planes [equivalent to (100) plane due to symmetry of the tetragonal structure] as its side surfaces perpendicular to the zone axis and the (001) planes as the other side surfaces parallel to the zone axis. The measured lattice spacings (a,b = 4.74 Å and c = 3.19 Å) and the observed diffraction pattern are in excellent agreement with the tetragonal crystal structure of SnO_2. The high-resolution TEM images taken at the edge of the nanowire confirm the observed growth orientation of [100] (marked by long arrows in Figure 6.5a, right panel) with the measured lattice spacing of 4.74 Å. Other high-resolution images taken across the nanowires (not shown) show no discernible lattice defects with essentially identical lattice constants. Furthermore, high-resolution TEM images collected over a large scan area (not shown) do not show any fault line in the crystal structure of the nanowire. Minor variations (smaller than 2 nm) in the width of the nanowire are also observed (not shown), which affirm the layered surface structure observed on the surface of the nanowires in the HIM image (Figure 6.2e), and the general tapering shape of the nanowire (toward the tip).

Figure 6.5b and 6.5c show the TEM images obtained for two nanobelts, which are selected to illustrate the different possible growth orientations within a single PLD-grown nanobelt sample. The observed differences in contrast for different sections of the nanobelts (Figure 6.5b, 6.5c) are the result of mechanical twists and bends along the length (10-30 μm) of the nanobelts (Figure 6.2b). The corresponding SAED patterns reveal different growth orientations along their length perpendicular to the (010) (Figure 6.5b) and (101) planes (Figure 6.5c) in these nanobelts. The SAED patterns further show that the nanobelts have (101) planes as their narrow side surfaces parallel to the zone axes (Figures 6.5b and 6.5c), while they show differing planes perpendicular to [10–1] (Figure 6.5b) and [010] (Figure 6.5c) zone axes on their wide side surfaces. The plane perpendicular to [010] axis is (010) or equivalently (100) plane, while the closest plane perpendicular to [10–1] axis is (201) plane with a 87.3 ° angle. The corresponding high-resolution TEM images show the single-

crystalline nature of the nanobelt structures, and the measured lattice spacings of 2.38 Å and 2.64 Å correspond to the [010] (Figure 6.5b, right) and [101] directions (Figure 6.5c, right), respectively, which confirm the growth directions identified in their respective SAED patterns.

The different growth orientations found in these nanobelts leading to (101), (100), and (201) plane growth are in good agreement with our XRD results (Figure 6.4), which indicate a preferred growth orientation in comparison to the reference polycrystalline SnO_2 pattern for both the (200) and (101) planes. The observed preferred growth of the nanowires for the (200) peak in the GIXRD results (Figure 6.4) can also be explained by the observed growth planes of (100) and (001), where the former will cause the observed high intensity of (200) peak. The presence of different growth planes for nanowires and nanobelts can also account for the observed differences in the cross-sectional morphologies, where the growth rate of different planes will be affected by modifying the temperature. The formation of (001) side planes, which possess the highest surface energy among the low-index planes of TO,[7] for nanowires suggests that the higher deposition temperature of 600°C, in comparison to 500°C for nanobelts, provides enough energy for the growth of this plane. The higher growth rates expected for the high-energy surfaces can therefore explain the observed square cross-section of nanowires in oppose to the rectangular cross-section of nanobelts, where the other side planes have a lower growth rate than the (101) side plane. These results indicate that the catalyst-assisted PLD method provides sufficient energy for growth in different low-index directions and that the deposition parameters can be used to control these orientations leading to different morphologies.

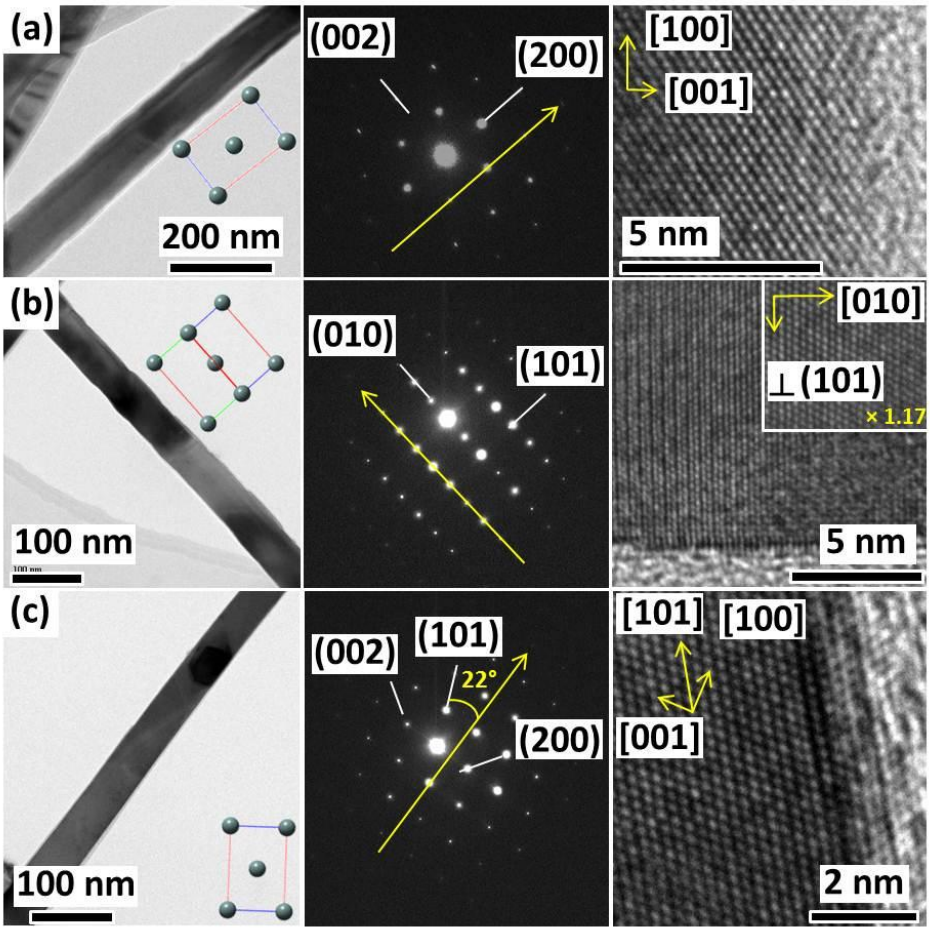

Figure 6.5 Low-resolution TEM images (left) with their corresponding SAED patterns (center), and high-resolution TEM images (right) with spacings corresponding to different crystalline planes for (a) nanowire, and (b, c) nanobelts with different growth orientations. The ball-stick models of the SnO_2 unit cell show the crystalline orientations of nanostructures, and the extracted crystal directions are indexed in the SAED patterns, with the growth directions marked by long arrows.

6.4 Conclusions

A variety of single-crystalline nanostructures of TO are synthesized using a new catalyst-assisted PLD technique. Deposition parameters, including the substrate temperature and the gas pressure of different process gases (O_2 or Ar), and the type of support for the GNI template (ox-Si or H-Si) are all found to have strong effects on the morphology of the resulting nanostructures. At 700°C, faceted nanobricks are obtained on a GNI/ox-Si template in O_2, while faceted nanoparticles are grown on a GNI/H-Si template in Ar, both through the catalytic vapour-solid growth mechanism. On the other

hand, nanospikes are obtained on a GNI/ox-Si template in Ar at 700°C, through the catalytic vapour-liquid-solid mechanism. Furthermore, reducing the deposition temperature leads to the growth of micron-long nanowires at 600°C and nanobelts at 500°C, all with remarkably small cross-sectional dimensions. We demonstrate for the first time that by creating a supported GNI template, it is possible to promote VLS growth (in preferred orientations) at a relatively low temperature by using PLD and to produce a variety of 1D TO nanostructures. Furthermore, not only the length of the nanobelts and nanowires can easily be controlled by the deposition time, their width and density on the surface can also be modified by varying the size and density of the GNI's on the substrate. In addition, X-ray diffraction data confirms the presence of a single, tetragonal SnO_2 crystalline phase, and a preferred growth orientation of (200) for nanowires, (200) and (101) for nanobelts and of (101) for nanobricks and nanoparticles. TEM results further show the single-crystalline nanostructures of the nanobelt and nanowire and reveal the different growth orientations of these 1D nanostructures in excellent accord with our XRD data. The present work therefore demonstrates the potential of catalyst-assisted PLD technique for creating single-crystalline 1D TO nanostructures, and introduces a new approach to synthesis of other oxide nanostructures with controllable morphologies and dimensions, as well as growth orientation and direction. With their high surface area and in a selected number of low-index surface planes, these 1D TO nanostructures offer a unique opportunity to exploit the selectivity and reactivity of their surface chemistry in a variety of applications, including chemical sensing. Moreover, this method can easily accommodate the introduction of dopants for developing new or optimizing existing properties of these TO nanostructures for opto/electronics applications.

Chapter 7

Growth evolution of Tin (IV) Oxide nanobelts on supported gold islands by Catalyst-Assisted Pulsed Laser Deposition: Promoting growth in selected surface planes through SnO_2–support crystalline correlation

In this chapter, we investigate the growth evolution of the nanobelts deposited using the catalyst-assisted PLD method, as we described in Chapter 6, at different stages of growth by using a mask-induced growth gradient on various GNI/substrate templates. Furthermore, the effects of different templates on the crystalline growth direction and the morphology of the nanobelts are also studied. The nanobelt deposition, the mask-induced method of investigating the growth mechanism, and the preparation of GNI templates are described in Chapter 2 in detail.

7.1 Morphology Evolution

Figure 7.1 shows the different stages of growth for the nanobelts PLD-grown at 500°C with 400 mtorr of Ar on a GNI/ox-Si template. The GNI's formed on the ox-Si (Figure 7.1a) exhibit a generally dome-shaped morphology with an average diameter of 50 nm and a near-Gaussian size distribution. In spite of the possible Au silicide formation[80] in the GNI/ox-Si interface, the GNI's are found to be easily dislodged during the deposition at 500°C. This is in contrast to the GNI/H-Si template where GNI's are strongly bound, possibly due to a larger number of Si sites for Au silicide formation. Figure 7.1b shows preferential growth of TO nanostructures almost exclusively at the GNI sites instead of the bare ox-Si areas (not covered by GNI's), which evidently prevent further growth initiation as observed below. In particular, the growth of TO nanostructure pushes up and dislodges the GNI, tilting the sharp Au-TO interface (e.g. marked by arrows in Figure 7.1b) and giving rise to a wedge-shaped TO stub. The observed growth evolution is indicative of a typical VLS growth mechanism,[57] in which most of the vapour undergoes dissolution in the GNI's preferentially instead of adsorption on the bare ox-Si surface as a result of the higher absorption rate for GNI near its melting point. The dissolved vapour subsequently precipitates to form the TO nanostructure at the Au and Si interface, leading to the detachment of the GNI. As deposition continues, the faceted TO stubs grow horizontally in length, filling up the open areas in between the GNI's. The Au-TO interfaces of the resulting nanorod remain sharp and become more vertical (Figure 7.1c, with arrows

marking the interfaces). As the nanostructure growth continues, these horizontal nanostructures start to run into one another and cause abrupt changes in their growth direction (e.g. marked by arrows), creating a planar, interconnecting "nanoroot" network, as clearly illustrated in the HIM image of Figure 7.1d. Moreover, some of these interceptions deflect the growth fronts vertically away from the substrate base (e.g. marked by open squares), lifting the GNI up from the substrate while causing the GNI to become more spherical. Without the obstacles at the base, further growth in the vertical direction initiates the formation of the nanobelts with their characteristic rectangular cross sections, with some of the nanobelts undergoing further deflection near the base before launching into more vertical growth (Figure 7.1d, 7.1e; e.g. marked by open circles). Further deposition results in an increase in the number and length of the nanobelts, leading to a dense mat of nanobelts. These nanobelts are found to have a characteristic rectangular cross-section of 30×5 nm^2 to 70×30 nm^2 (Figure 7.1f, inset), and they grow to 10-30 μm long after 90 min of deposition (Figure 7.1f). The GNI's appear to be settling on the wide side of the nanobelts at the tip. Furthermore, unlike nanoribbons, these nanobelts appear straight and stiff with considerable rigidity and they grow to an extended length before notable bending occurs. It is of interest to note that the nanobelts with a bigger GNI catalyst and a smaller cross-section are always found to be long, which is consistent with the VLS growth mechanism in which a larger TO vapour absorption provided by a larger catalyst on a smaller cross-sectional footprint would lead to a longer nanostructure.

The presence of amorphous oxide layer over the entire GNI/ox-Si template, i.e. including the open area not covered by GNI's, prevents any potential crystalline correlation between the substrate and the growing TO nanobelts. However, as shown in our earlier work[123] and in Figure 7.1, the presence of this oxide layer is crucial for the detachment of GNI's and initiation of the VLS growth mechanism. In order to investigate the effect of substrate surface crystallinity on the TO nanostructure growth, we remove the oxide in the area not covered by GNI's on the GNI/ox-Si template by a mild 2% HF (aq.) etch for 12 min. At a deposition temperature of 500°C, the H atoms on the resulting H-terminated Si area are expected to undergo recombinative H_2 desorption,[124] leaving a pristine Si(100) surface. Figure 7.2 shows the HIM images of the nanobelts at different stages of the PLD growth at 400 mtorr Ar and 500°C on this HF-treated GNI/ox-Si template. Evidently, at the early stage of growth, only a small number of GNI's lead to TO nanostructure growth (Figure 7.2a, marked by arrows) following the VLS growth mechanism, similar to that observed for the untreated GNI/ox-Si template (Figure 7.1b). A closer examination of the features on the open area not covered by GNI's (Figure 7.2b) reveals a holey TO layer blanketing the entire template, which also covers the

GNI's not active in the VLS growth. This observation suggests that most of the GNI's could migrate from the original nucleation site at the deposition temperature of 500°C, and they appear to interact strongly with the bare Si surface before TO deposition, preventing detachment of the GNI's and initiation of VLS growth. Continuing the ablation leads to further growth of the nanorods (Figure 7.2c, 7.2d) with their increasing length becoming more likely to intercept other nanorods or GNI's on the surface. Kinks (marked by arrows in Figure 7.2c, 7.2d) appear to be formed with sharp angles in changing the growth direction due to interception, which indicates that the growing nanorods are highly crystalline and the kinks are likely occurring along their preferred crystalline directions. These interceptions could also deflect the nanorods upward, lifting off the GNI's and leading to the more vertical growth of the nanobelts (Figure 7.2d). After the GNI liftoff, short nanobelts with well-defined rectangular cross sections begin to emerge, marking the initial stage of nanobelt growth (Figure 7.2e). Small TO nanocrystallites with irregular shapes (nanogravels) cover both the inactive GNI's and the open area of the Si substrate not covered by GNI's. Further ablation leads to increased coverage of the nanobelts with increasing lengths and uniform rectangular cross section (30×5 nm^2 to 70×30 nm^2, Figure 7.2f, upper inset) over an extended length (up to 50 μm, Figure 7.2f). On the other hand, the nanogravels do not exhibit an appreciable change in size (Figure 7.2f, lower inset) and appear to grow considerably slower than the nanobelts, which is likely due to a greater absorption rate of TO vapour in the GNI's (than the adsorption rate on the rest of substrate) leading to faster VLS growth of the nanobelts. It is of interest to note that the maximum length of the nanobelts grown on the HF-etched GNI/ox-Si template (~ 50 μm) appears to be larger than the nanobelts grown on GNI/ox-Si template (i.e. without the HF etch) (~ 30 μm), for the same amount of deposition time (90 min). The HF-etched template is therefore more favourable in inducing growth in a fast growth direction than the un-etched template, as discussed below in our XRD data.

In earlier studies, epitaxial growth of TO thin films in the (100) direction has been found to occur on the Al_2O_3(0001) surface.[125] In order to investigate whether the presence of a substrate with a good epitaxial relation to TO could affect the crystalline growth direction of 1D TO nanostructure, we prepare nanobelts PLD-grown in 400 mtorr of Ar at 500°C on a GNI/Al_2O_3(0001) template. Evidently, the HIM image in Figure 7.3a shows that the majority of the GNI's are active in promoting VLS growth of TO nanobelts, which suggests that unlike the bare Si(100) substrate, there appears to be little interaction between the GNI and the Al_2O_3 substrate. This difference between the Si and Al_2O_3 substrates has also led to the formation of bigger GNI's on Al_2O_3 compared to those on Si for a similar layer thickness of deposited gold. Deposition leads to growth of irregularly shaped TO

nanostructures planar to the surface in areas between the GNI's (e.g. marked by arrows, Figure 7.3a), indicative of onset of a plausible epitaxial film growth. The presence of these nanostructures also appears to restrict the VLS growth in the planar direction and leads to the early liftoff of GNI's (Figure 7.3a). Further deposition leads to initiation of the nanobelt growth on top of the as-formed planar nanostructures (e.g. marked by arrows, Figure 7.3b) with upward growth direction. There appears also to be essentially no change in the growth direction for the nanobelts within the limited travel of the GNI after liftoff (Figure 7.3c). As for the other GNI/ox-Si template where most of the GNI's are active in the VLS growth, the TO nanobelts obtained on the present GNI/Al_2O_3 template are found to have similar length (Figure 7.3d, inset) and cross-sectional dimensions (Figure 7.3d). The epitaxial relation of the Al_2O_3(0001) surface with SnO_2 (to be supported by XRD data discussed below) has therefore restricted the extent of nanostructure travel before liftoff in the early stage, without significantly affecting the morphologies from that of the nanobelts obtained on the GNI/ox-Si template. It should also be noted that the planar nanostructures eventually fill in the gaps between the GNI's and form a continuous layer on the Al_2O_3 substrate (Figure 7.3d).

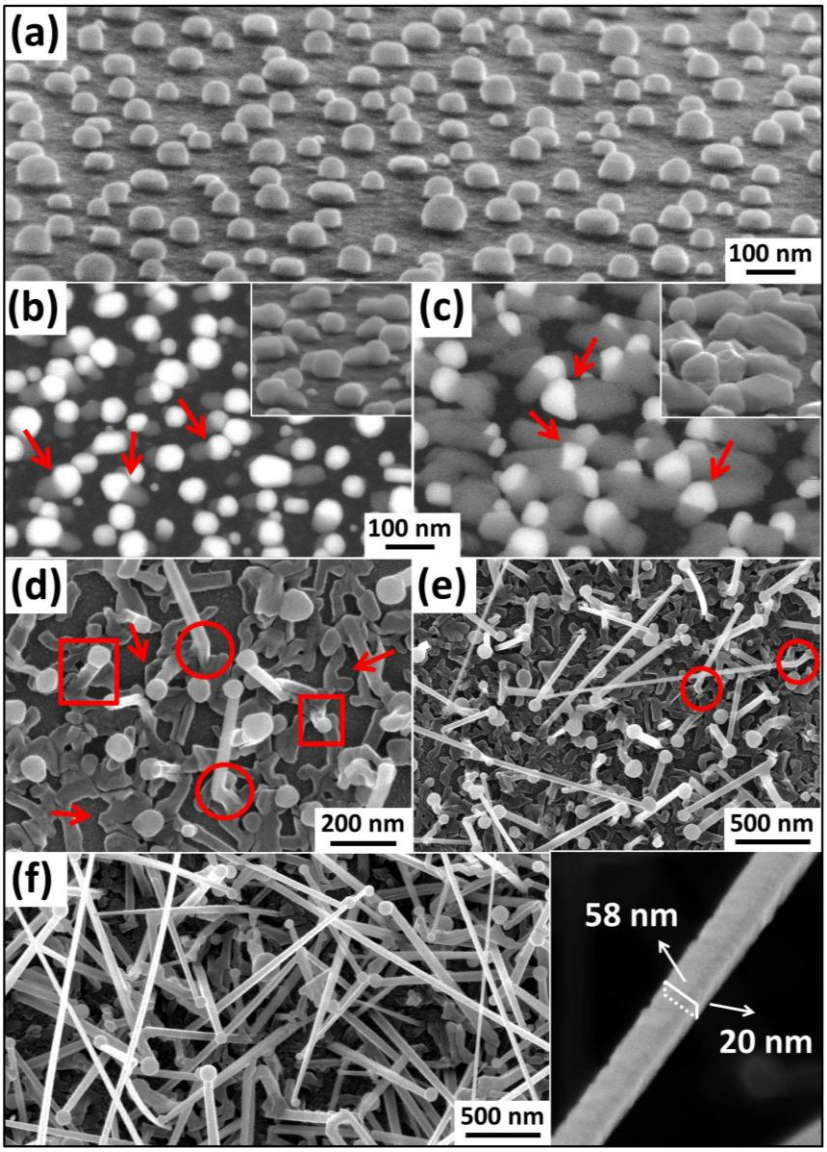

Figure 7.1 Secondary-electron SEM image collected at 70° tilt of (a) a gold nanoisland/oxidized-Si template, and backscattered-electron SEM images of the corresponding gold/SnO_2 nanostructures at (b) the growth initiation and (c) nanorod growth stages (insets show secondary-electron SEM images) with arrows marking the Au/SnO_2 interfaces. HIM images of (d) nanorods in the deflection stage, and of nanobelts (e) in the initial and (f) final growth stages of PLD growth in 400 mtorr Ar at 500°C. The arrows, open squares, and open circles in (d, e) mark the planar deflections, vertical deflections, and kinks, respectively. The inset in (f) shows the rectangular cross section of a typical nanobelt.

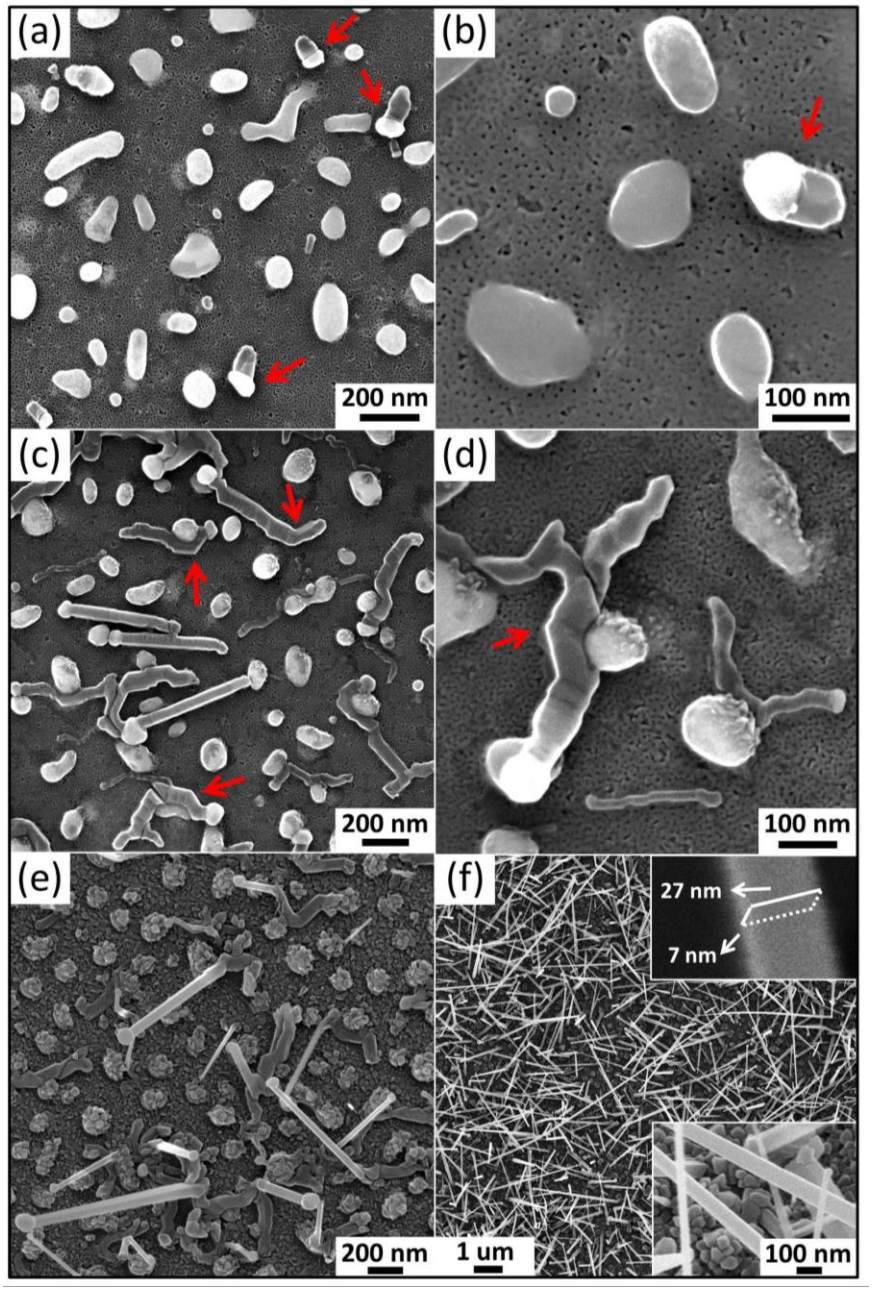

Figure 7.2 HIM images of the nanobelts PLD-grown on a HF etched GNI/ox-Si template in 400 mtorr Ar at 500°C (a) and (b) at the growth initiation stage (with active GNI's marked with arrows), (c) at the planar nanorod growth stage leading to (d) vertical deflections and lift-off (with planar kinks marked by arrows), (e) at the initial and (f) final stages of nanobelt growth for a 90 min deposition. In (f), the upper and lower insets show one of the typical ultrathin nanobelts, and the final growth stage of nanogravels on the substrate, respectively.

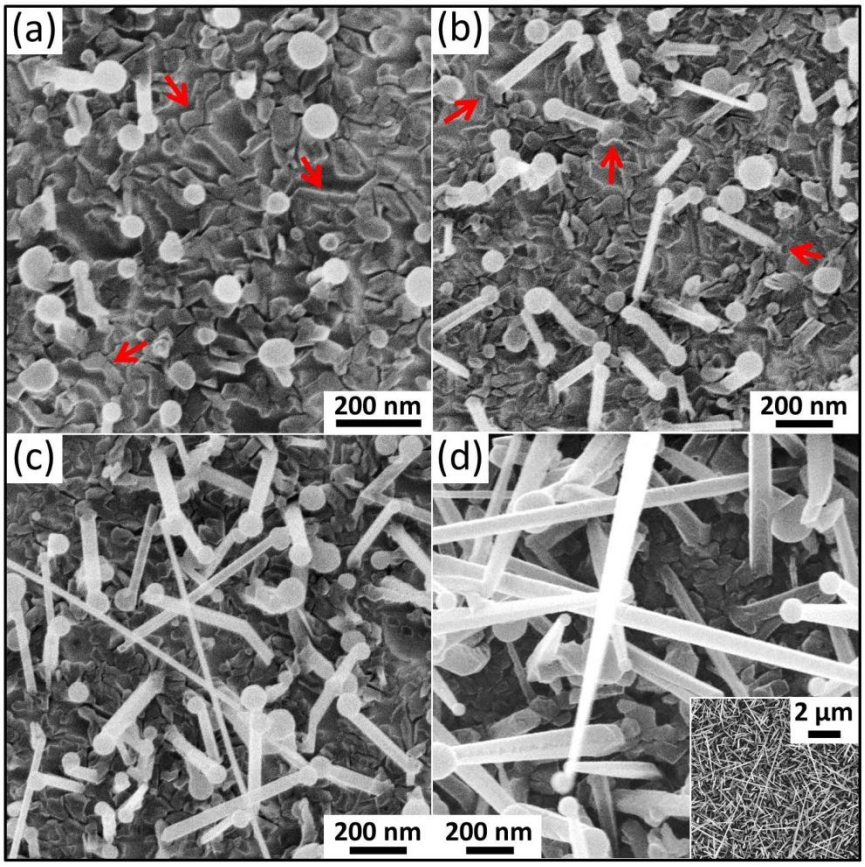

Figure 7.3 HIM images of the nanobelts at different stages of PLD growth on a GNI/Al_2O_3 template at 400 mtorr Ar and 500°C, including (a) planar nanostructure growth; (b) initiation of nanobelt growth; (c) liftoff of nanobelts; and (d) final growth.

7.2 Transmission Electron Microscope Studies on the Growth Evolution

TEM studies are performed on the nanobelts PLD-grown in 400 mtorr Ar at 500°C on the GNI/ox-Si, HF-etched GNI/ox-Siand GNI/Al_2O_3 templates. These nanobelts grown on the three templates are found to exhibit similar crystallinity, with examples of typical features shown in Figure 7.4. Evidently, selected area electron diffraction (SAED, Figure 7.4a, 7.4d) shows the single-crystallinity of the nanobelts obtained on the different templates by using the catalyst-assisted PLD method. Furthermore, the growth axes (shown as arrows in the SAED patterns) are found to be either [101] (Figure 7.4a), or [010] (also equivalent to [100], Figures 7.4d), which correspond to the crystalline orientations shown schematically with the ball-and-stick unit-cell model of the tetragonal SnO_2

structure (Figure 7.4a, 7.4d,insets). These orientations are also in good agreement with the observed atomic arrangements and spacings in their corresponding high-resolution TEM images (Figure 7.4c, 7.4f). The high-resolution TEM images taken across the width of the nanobelt near the edge and at the middle show near-perfect crystallinity, which is indicative of a very uniform and small thickness. Of the 15 different nanobelts examined by TEM in the present work, the nanobelts with the [101] growth direction are found to be generally short (1-5 μm in length), while the nanobelts with significantly longer lengths of 10-30 μm all have the [010] growth direction, as shown in the insets of low-resolution images (Figure 7.4b, 7.4e). Earlier studies on TO nanoribbons and nanowires grown by thermal evaporation,[26,126] however, have reported only the [101] growth direction. Our present observation of nanobelt growth with two different growth directions and rates therefore suggests different growth thermodynamics and kinetics, respectively, for the catalyst-assisted PLD method from the thermal evaporation synthesis. The resolved crystalline structures for the nanobelts (Figures 7.4a) further show that the nanobelts with the [101] growth axis have the (101) plane as their narrow-side surface and the (010) plane [also equivalent to (100)] as their wide-side surface, similar to what has been reported for the nanowires and nanoribbons grown by thermal evaporation.[26,126] The nanobelts with the [010] growth axis (Figure 7.4b) have the same (101) plane on their narrow sides, but their wide sides are perpendicular to the [–101] (equivalent to [101]) direction and do not correspond to any crystalline plane, which has not been observed in the thermal evaporation[28] and laser ablation studies.[29] The (201) plane, which makes a 87.3° angle with the [–101] direction, represents the closest plane for the wide sides. Alternatively, the wide sides could be considered to be a (201) plane with a 2.7° miscut, which corresponds to a heavily stepped surface with high reactivity. Further investigations using surface science methods including low-energy electron diffraction or scanning tunneling microscopy are required to elucidate the crystalline structure of this "stepped" surface.

In our surface morphology studies of the nanobelts growth (Figures 7.1 and 7.2), we observe that the nanobelts generally start to grow in a planar fashion until the growth front is deflected into a different direction by other objects on the substrate. Figure 7.5a shows an example of one such growth route of a nanobelt PLD-grown in 400 mtorr Ar at 500°C on a GNI/Al_2O_3 template, in which a ~400 nm long straight section is deflected, causing the growth to be redirected into the final ~2 μm long straight section of the nanobelt. The SAED patterns collected before (Figure 7.5d) and after the deflection (Figure 7.5c) and near the Au tip (Figure 7.5b) reveal the same single-crystalline orientation at all three locations of the nanobelt, marked as 1, 2, 3 in Figure 7.5a. The growth axis

before the deflection (marked by arrow in Figure 7.5d) is found to be along the [10–1] direction. The [10–1] direction is assigned based on the 22±1° angle observed between the growth axis and the (10–1) diffraction plane (Figure 7.5d) and on the atomic arrangement as shown in the ball-and-stick model (Figure 7.5a). After deflection by 113±1°, the growth axis has evidently changed to the [101] direction (Figure 7.5c) and remains unchanged along the length of the nanobelt (Figure 7.5b). It should be noted that the [10–1] growth axis is equivalent to the [101] direction due to the symmetry of the tetragonal structure. The high-resolution TEM images taken after the deflection (Figure 7.5f) and near the tip (Figure 7.5e) show well-resolved crystalline planes along the length of the nanobelt, i.e. parallel to the growth axis. Moreover, the interplane spacing is found to be 2.6 ± 0.1 Å for both locations, which corresponds to the lattice spacing of the (101) planes, in good accord with the SAED results.

Figure 7.6 shows the TEM results obtained near the base of a nanobelt PLD-grown in 400 mtorr Ar at 500°C on a GNI/ox-Si template. Of particular interest is the kink observed in the low-resolution TEM image (Figure 7.6a), which shows a change in the growth direction at the initial growth stage of the nanobelt. The high-resolution images taken at different locations before (Figure 7.6b), at (Figure 7.6c) and after the kink at the edge of the nanobelts (Figure 7.6d, 7.6e) show well-resolved lattice planes all with the same spacing of 3.4 ± 0.1 Å, corresponding to that of the (110) plane in bulk SnO_2 (PDF2#00-041-1445). Moreover, the lattice planes observed in all the high-resolution images have the same orientation, indicating a single-crystalline structure for the entire nanobelt in spite of the change in the growth direction in the kink region. The SAED patterns (Figures 7.6f and 7.6g) taken before and after the change in the growth direction in the kink region (labeled as 1 and 2 in Figure 7.6a) also show a single-crystalline structure with the same crystalline orientation. The growth axis of the nanobelt before the kink (Figure 7.6f) makes a 22±1° angle with the (–110) diffraction plane, which does not correspond to any low-index growth direction of the nanobelt, as depicted by the ball-and-stick model. This indicates a high index growth direction corresponding to a high-energy growth axis before the kink. On the other hand, the growth axis after the kink makes a 54±1° angle with the (–110) diffraction plane, which matches the [101] growth direction. This assignment is also in good agreement with the observed complementary 36±1° angle of the (110) plane with respect to the [101] growth axis, as observed in the high-resolution TEM images in Figures 7.6d and 7.6e.

The present TEM study therefore shows that the entire nanobelt has remarkably maintained its single-crystalline structure, despite the change in the growth direction during the growth evolution,

from the initial planar growth on the substrate with various straight sections and deflections, to lift-off of the Au catalyst, and finally to nanobelt growth. If growth occurs along a low-index (i.e., low energy) axis, the growth will continue along the same direction until obstruction is encountered (Figure 7.5). If, on the other hand, the growth direction happens to be not along a low-index axis, e.g. at the kink region in Figure 7.6 or when an obstacle is encountered, the growth will not continue in that direction and a change in the growth axis back to a low-index direction will occur.

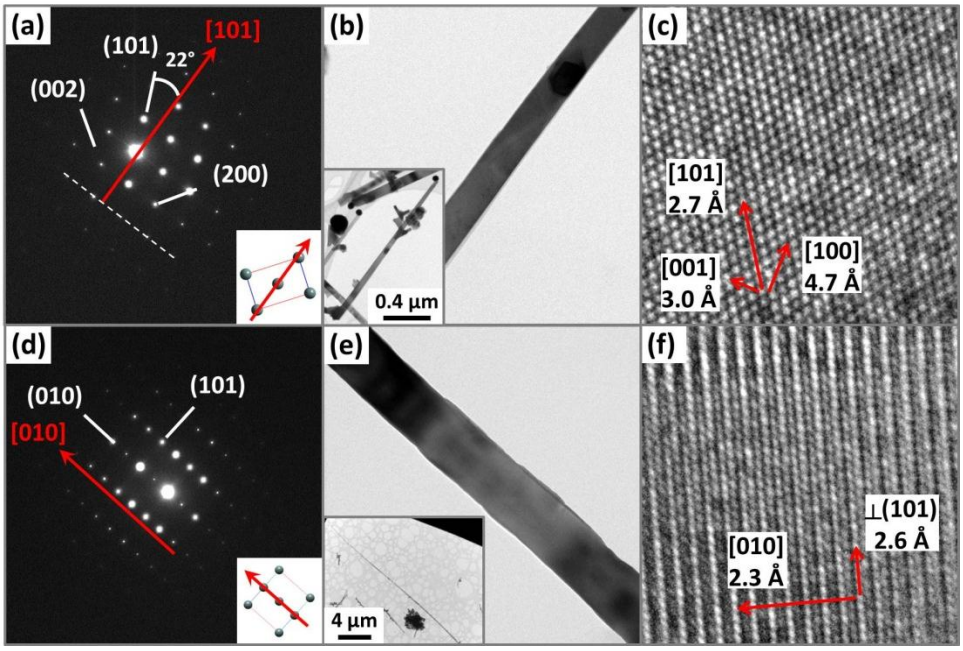

Figure 7.4 (a, d) Selected-area electron diffraction (SAED) patterns , (b, e) low-resolution, and (c, f) high-resolution TEM images of nanobelts PLD-grown on (a-c) GNI/ox-Si, and (d-f) HF-etched GNI/ox-Si templates. A ball-and-stick model for the SnO_2 unit cell shows the extracted crystal orientation, with the long arrow indicating the growth axis of the nanobelts. The low magnification images (b, e insets) show the extended lengths of the nanobelts.

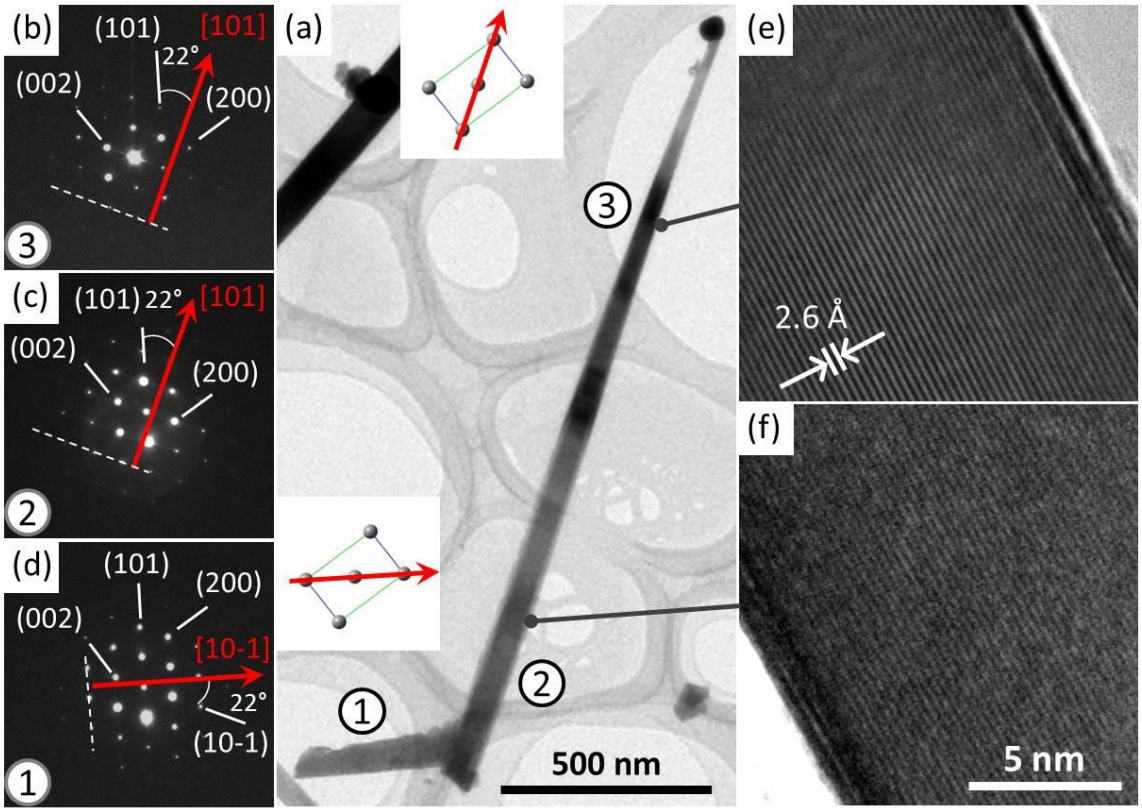

Figure 7.5 (a) Low-resolution TEM image of a nanobelt with an initial nanorod growth followed by a change in the direction, and SAED patterns obtained at locations (d) 1, (c) 2, and (b) 3. High-resolution TEM images are also collected (e,f) at two points marked by lines on (a). The arrows in the ball-and-stick unit cell models and on SAED patterns show the growth axis of the nanobelt at their corresponding location.

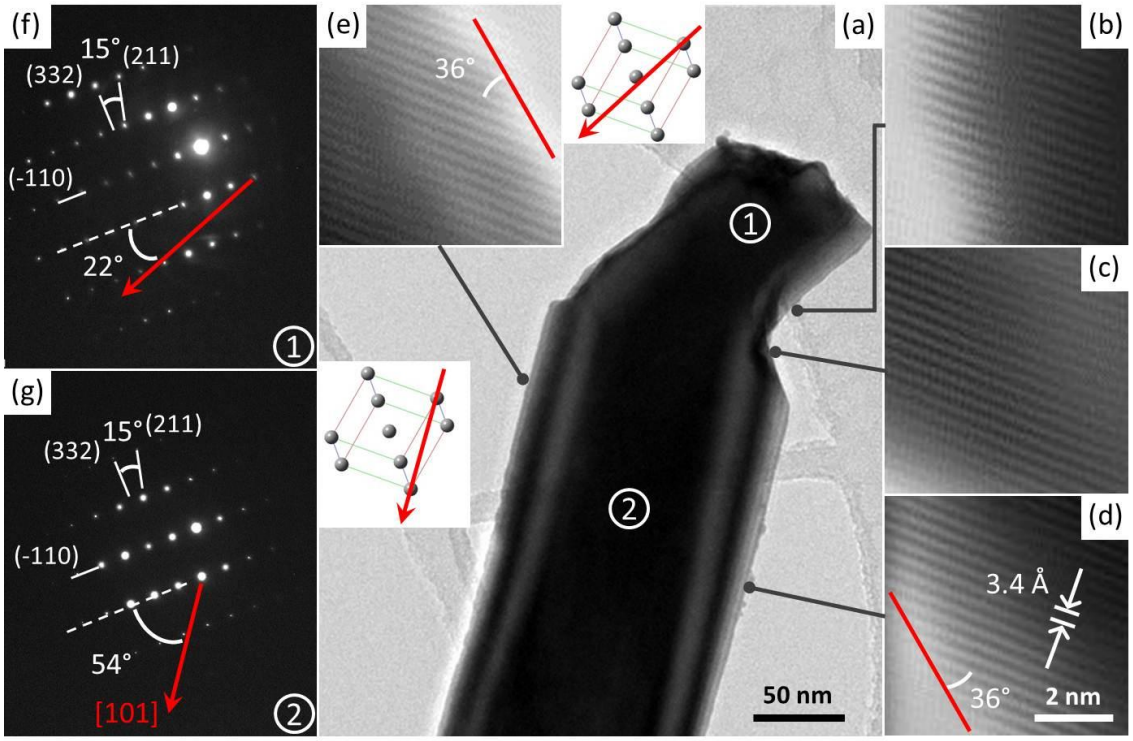

Figure 7.6 (a) Low-resolution TEM image of a nanobelt with a kink near its base, and (b-e) high-resolution TEM images collected at selected locations marked by lines, and (f, g) SAED patterns for locations 1 and 2, respectively. Arrows in the SAED patterns and the ball-and-stick unit cell models show the growth directions of the nanobelt at their corresponding locations.

7.3 Average Crystalline Structure of Nanobelts

The crystalline structures of the TO films deposited on H-Si and ox-Si substrates, i.e. without the GNIs, and of the nanobelts PLD-grown on GNI/ox-Si, HF-etched GNI/ox-Si, and GNI/Al_2O_3 templates, all in 400 mtorr Ar at 500°C are examined by GIXRD at an incidence angle of 0.3°. The GIXRD patterns observed for all the samples (Figure 7.7a) are in good agreement with the tetragonal phase of polycrystalline SnO_2 (PDF2#00-041-1445). Weaker features corresponding to fcc Au (PDF2#00-004-0784) are also detected for the nanobelt samples PLD-grown on supported GNI templates. In comparison with the reference pattern of polycrystalline SnO_2 (PDF2#00-041-1445), the TO films deposited on the H-Si and ox-Si substrates (without the GNI's) show higher relative intensities for the (101) and (110) peaks, respectively, indicating preferential growth in these

respective planes. On the other hand, the nanobelts PLD-grown on GNI/ox-Si and HF-etched GNI/ox-Si exhibit discernibly higher relative intensities for both the (101) and (200) peaks, while the nanobelts PLD-grown on GNI/Al_2O_3 show a higher relative intensity only for the (200) peak with the weaker signal and a more pronounced background due to the smaller substrate size (5×5 mm^2 for Al_2O_3 vs 10×10 mm^2 for ox-Si).

In order to investigate the crystal orientation of the growth with respect to that of the Si(100) or Al_2O_3(0001) substrate, we perform a symmetrical ω-2θ XRD study on the TO films and nanobelt samples. The strong (101) and (110) peaks for the TO films grown, respectively, on the H-Si and ox-Si substrates (Figure 7.7b) indicate preferred growth in these respective planes. Because the ox-Si substrate is covered by an amorphous oxide layer, the observed (110) preferred growth plane for the TO film could be attributed to the lower surface energy of the (110) plane in an Ar environment (instead of an oxygen)[7] and/or a self-sputtering effect caused by the energetic ions in the plasma. On the other hand, the observed (101) growth plane for the TO film on the H-Si substrate suggests possible epitaxial relations with the Si(100) substrate.

The nanobelts PLD-grown on the GNI supported templates all exhibit generally more intense XRD features than the TO films on ox-Si and H-Si, in the order of HF-etched ox-Si < ox-Si < Al_2O_3 (Figure 7.7b). The increase in the intensities is consistent with the observed increase in the numbers of active GNI's promoting VLS growth on the three supports (Figures 7.1-7.3), leading to increased absorption of the TO vapour and consequently the deposited amount. Furthermore, the XRD patterns for the nanobelts PLD-grown on GNI/ox-Si and on HF-etched GNI/ox-Si are found to be very similar to each other. Both nanobelt samples are markedly different from that for the TO film PLD-grown on ox-Si, with the (101) peak being considerably stronger than the (110) peak in the nanobelts relative to that in the TO film. The observed intensity ratios for both (101)/(110) (=1.01) and (200)/(110) (=0.39) [after correcting the SnO_2(200) intensity for the close-lying Au(111) peak by fitting two peaks with FWHMs consistent with the other SnO_2 and Au peaks at 37.95° and 38.20°, respectively] for the nanobelt sample grown on GNI/ox-Si template are considerably larger than the reference powder pattern (0.75 and 0.21, respectively), which confirms the observed preferred growth planes of the nanobelts, as indicated in the GIXRD (Figure 7.7a) and TEM results (Figure 7.4). For the nanobelts grown on HF-etched GNI/ox-Si template, the expected growth plane of TO nanostructures grown in the open areas of the Si(100) substrate is (101), as observed for the TO film grown on H-Si (Figure 7.7b). The observed (101)/(110) intensity ratio (0.85), however, is notably smaller than that

(1.01) observed for the nanobelts grown on the GNI/ox-Si template. Moreover, the (200)/(110) intensity ratio has dropped to the polycrystalline ratio level. The overall decrease in the intensity ratios is due to the decrease in the amountof nanobelts grown on the HF-etched GNI/ox-Si template. The disappearance of the preferential (200) growth can also be explained by assuming pinning of the nanoroot section of the nanorod with the (101) plane on the Si(100) substrate (as observed for TO growth on the H-Si substrate). This pinning leads to the preferential growth of nanobelts in the [100] direction after the lift-off stage, as a result of the single-crystallinity of the entire nanobelt. Growth of the nanobelt in the [100] direction with the (101) and (201) side surfaces gives rise to an intense (101) peak, as opposed to the growth in the [101] direction with the (101) and (200) side surfaces, which leads to increases in intensities of both (101) and (200) peaks. The extremely long nanobelts characteristic of the growth in the (200) direction found on the HF-etched GNI/ox-Si also support this explanation (consistent with our TEM results shown in Figure 7.4).

In marked contrast to the nanobelts grown on GNI/ox-Si and on HF-etched GNI/ox-Si templates, where the (101)/(110) intensity ratio is larger than the corresponding (200)/(110) ratio, the nanobelts grown on GNI/Al_2O_3 template exhibit the reverse trend (Figure 7.7b). Indeed, the latter nanobelts sample shows a remarkably large (200)/(110) intensity ratio (6.48), indicating a strong epitaxial relation of the (100) plane of SnO_2 with the Al_2O_3(0001) substrate, as previously reported for the growth of TO thin films.[125] This larger (200)/(110) intensity ratio found for the nanobelts on the GNI/Al_2O_3 template can therefore be attributed to the planar TO nanostructures grown in the open areas not originally covered by GNI's on the Al_2O_3 substrate (Figure 7.3). Furthermore, a larger (101)/(110) intensity ratio (1.49) for the nanobelts grown on GNI/Al_2O_3, relative to the nanobelts grown on GNI/ox-Si (0.98), is also observed and can be attributed to the nanobelt growth with dominant (101) surfaces. The epitaxial relation of TO with the Al_2O_3(0001) surface therefore leads to the spatial restriction of the planar nanorod growth stage on the substrate due to the formation of the planar epitaxial nanostructures in the open areas (Figure 7.3). The restricted planar growth causes the growth to continue in the pinned epitaxial growth direction and leads to the preferential growth of the nanobelts in the initial [100] direction with the (101) and (201) side surfaces, which therefore gives rise to the observed intense (101) peak.

The epitaxial relation between the TO nanostructures and the substrate could therefore affect the [101] or [200] growth orientation of the nanobelts in different ways. This control of the growth direction generally occurs by epitaxial pinning in the initial planar nanorod growth stage on the

substrate, which subsequently affects the final nanobelt growth direction because of the single-crystalline nature of the entire TO nanobelt including the root.

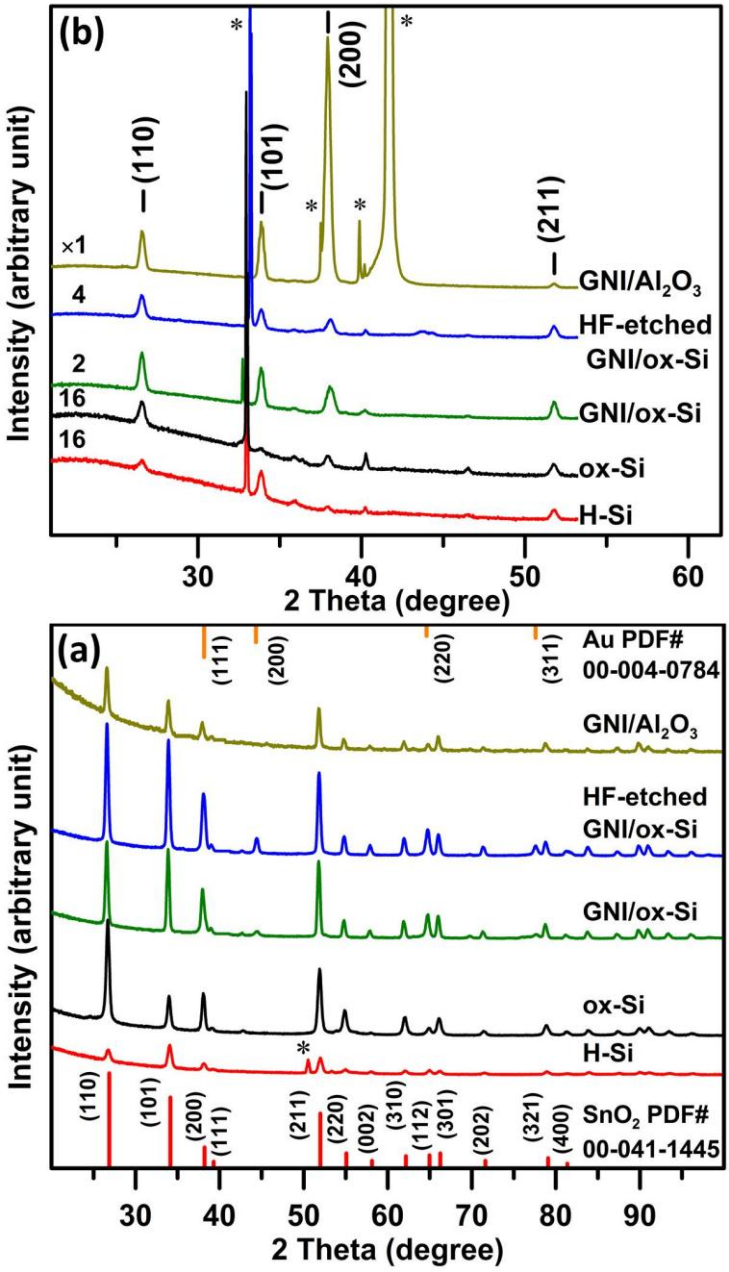

Figure 7.7 (a) Glancing-incidence XRD patterns of the SnO_2 films and nanobelts measured at an incidence angle of 0.3°, compared with the reference patterns of fcc gold (PDF2#00-004-0784) and tetragonal SnO_2 (PDF2#00-041-1445). (b) Symmetrical ω-2θ XRD scan of the SnO_2 films and nanobelts with the asterisks (*) marking the peaks associated with the Si(100) and Al_2O_3(0001) substrates.

7.4 Conclusions

Using a recently developed catalyst-assisted PLD method, we synthesize, for the first time, single-crystalline TO nanobelts by controlling VLS growth driven by gold catalysts with predefined nanometer size (<50 nm). These micron-long TO nanobelts are found to have an ultrasmall, rectangular cross section (30×5 nm^2 - 70×30 nm^2) and they tend to grow straight over an extended length. We investigate the growth evolution of the nanobelts on a GNI/ox-Si template by following a mask-induced growth gradient on the GNI template. Growth begins with detachment of the Au catalysts and proceeds with planar nanoroot formation. The former is an essential step for the VLS growth mechanism and can proceed on most oxide supports including ox-Si and Al_2O_3. Development of kinks and deflections in the nanoroots leads to Au nanocatalyst liftoff, which triggers the nanobelt growth. TEM study further shows the remarkable single-crystalline nature of the entire TO nanostructure, beginning with the nanoroot with a low-index growth direction and evolving to the nanobelt with the [101] or [010] directions upon kinks and deflections. Interestingly, the shorter nanobelts (1-5 μm) have the [101] growth direction while the longer ones (10-30 μm) have the [010] direction, indicating different growth kinetics for these directions. The shorter nanobelts are also found to have the (101) plane as their narrow-side surfaces and the (100) plane as their wide-side surfaces, while the longer nanobelts with the same (101) plane as their narrow-side surfaces have the (201) plane as their wide-side surfaces. Since the nanobelt preserves its single-crystallinity throughout the growth process, it may therefore be possible to generate a predominant (201) or (100) TO surface for appropriate applications, e.g. by establishing an epitaxial relation with an appropriate substrate to control the initial growth direction. By performing a short HF etch on the GNI/ox-Si substrate, we demonstrate that the bare Si(100) surface promotes longer nanobelt growth in the [100] direction by pinning nanoroot growth in the (101) plane. Furthermore, the GNI/Al_2O_3(0001) template provides an epitaxial relation with the TO (200) plane, which promotes nanobelt growth in the predominant [100] direction. The control of predominant side surfaces of the nanobelts offers potential applications, including chemical sensors, (opto)transistors and photonic components, that make use of their surface selectivity and reactivity and their differing electronic and defect structures.

Chapter 8
Concluding Remarks and Outlook for Future Work

This thesis presents the successful synthesis of nanocrystalline films and highly crystalline, faceted nanostructures of TO using spin coating and pulsed laser deposition methods. The growth mechanism of crystalline grains in the nanocrystalline TO film and the catalytic growth of TO nanostructures are investigated by performing extensive characterizations on these nanostructures. The results of these studies show promises in controlling the size of the TO nanostructures, while the effects of the size and crystallinity on the electronic transport and the luminescence properties of Eu-doped nanostructures are also studied systematically. The present study provides new findings on the synthesis and physical properties of pristine and Eu-doped nanocrystalline TO films, and on the growth of single-crystalline nanowires, nanobelts and other highly crystalline nanostructures of TO using the catalyst-assisted PLD method. Nanocrystalline TO thin films are obtained using the spin coating method with control on the average size of nanocrystallites in the 4-25 nm range. The electronic properties of the pristine nanocrystalline TO films and the optical and magnetic properties of Eu-doped nanocrystalline films are found to be greatly affected by the defect concentration and the crystallite size. Strong luminescence peaks are observed upon formation of $Eu_2Sn_2O_7$ in the highly doped TO films, and magnetic orderings are observed for the first time in this pyrochlore phase. Moreover, using the catalyst-assisted PLD method, we are able to grow a variety of highly crystalline nanostructures of TO, including nanobricks, cuboid nanoparticles, nanowires and nanobelts, each having a preferred crystalline growth orientation. The use of gold nanocatalysts leads to the formation of single-crystalline nanowires and naonbelts with different growth axis and side-surface planes at considerably lower temperatures of 500-600°C. Two crystalline growth axes with different side-surface planes are found for the nanobelts, further demonstrating that by using appropriate crystalline substrates, it is possible to promote growth preferentially along a specific axis.

8.1 Summary

In particular, by using a simple spin-coating method followed by post annealing in flowing O_2, nanocrystalline TO thin films are obtained, where the size of the crystallites can be easily controlled by manipulating T_{Anneal} in the 4-25 nm range. The onset of crystallization is found to occur at T_{Anneal}=350°C while another onset for the Arrhenius growth regime of the nanocrystallites at T_{Anneal}=500°C is also observed. The heterogeneous nucleation mechanism of the growth below the

onset of the Arrhenius growth regime, T_{Anneal}=500°C, along with the observed strain-limited growth mechanism, leads to the size stability of the crystallites obtained with postannealing at temperature below 500°C. The size stability upon prolonged heating is of great importance for gas sensing applications of TO nanostructures as discussed in the Introduction (Chapter 1). This fabrication method can therefore be of great value to the gas sensing applications.

Conductivity and bandgap measurements show that the nanocrystalline TO films obtained with $T_{Anneal} \geq 350$°C are conductive with a high carrier concentration, which causes bandgap broadening in these films. Our temperature-dependent measurements further reveal the presence of two different media involved in the electronic transport, i.e. the crystalline grains and the charge-depletion layer. Charge-depletion layer is highly resistive due to lowered carrier density in this medium, while there is an energy barrier of 48.0-60.5 meV for carrier transport across the grain boundaries. Transport in each medium is best described by the 3D-variable range hopping model and the fitting results reveal a decrease in the carrier density as crystallinity improves, while the localization length of carriers increases for samples obtained above the onset of exponential growth at T_{Anneal}=500°C.

We also show that homogenous Eu^{3+} doping in these nanocrystalline TO films obtained with T_{Anneal}=700°C can be achieved for doping concentrations up to ~ 8 at. %. These Eu-doped films show prominent characteristic Eu emissions at 593 nm and 614 nm, along with defect-related TO emissions below 550 nm. There is an effective energy transfer from TO structure to emission centres, and the relative intensities of these bands are linked to the symmetry of the Eu substitutional site, defect density and crystallite sizes, and the crystalline phase separation. At high concentrations of Eu, a new $Eu_2Sn_2O_7$ phase emerges, which further promotes the photoluminescence emissions depending on the nanocrystallite size and defect densities. Magnetic orderings are also observed in this pyrochlore phase at ~ 50 K. It should be noted that no previous report of magnetic ordering in this material is available in the literature. Furthermore, we also observe that the transition temperature is affected by the change in the crystallinity of the material.

By employing a catalyst-assisted PLD method for the first time, various highly crystalline TO nanostructures are fabricated. Deposition of a catalytic gold layer with controlled nanoisland sizes (10-50 nm) prior to TO deposition is the key to reducing the required process temperature that enables the catalytic growth of nanobricks, cuboid nanoparticles, nanowires (with a square cross-section), and nanobelts (with a rectangular cross-section). The resulting one-dimensional TO nanostructures, nanowires and nanobelts, are single-crystalline with the controllable cross-sectional

sizes. The catalyst-assisted PLD is demonstrated to be a powerful new method with the following capabilities for the fabrication of TO nanostructures:

- The cross-sections of the nanowires and nanobelts can be further reduced by controlling the size of the gold nanoislands (GNI's).
- Starting with a desired stoichiometry, different gas compositions can be used during the deposition to promote specific growth mechanisms: vapour-solid vs. vapour-liquid-solid (VLS).
- The substrate temperature is another important factor that can be used to control the formation of different surfaces, e.g. formation of the high-energy (001) side-surface planes for nanowires at a higher deposition temperature (600°C) in comparison to that of the low-energy (100) side-surface planes for nanobelts at a lower deposition temperature (500°C).

Of special interest is the observation of growth along two different axes of [200] and [101] in the nanobelts, where the former leads to the formation of (101) and (201) side surfaces, which have not been observed using other fabrication techniques, including the thermal evaporation method.

The growth evolution of nanobelts is also investigated in a greater detail using a mask-induced growth gradient on the perimeters of the Al_2O_3(0001) and chemically treated Si(100) substrates. The following summarizes the main features of nanobelt growth on these substrates:

- The crucial step that initiates the VLS growth mechanism is the detachment of GNI's as the result of TO deposition at the gold/substrate interface, which requires a weak bonding between the GNI's and the substrate.
- Horizontal "nanoroot" growth follows the detachment of GNI's on the Si substrates, while the upward deflections in the planar nanoroot growth lead to out-of-plane growth of nanobelts. Remarkably, the entire nanostructure, nanoroot plus nanobelt, keeps its single-crystalline structure.
- Nanobelts are found to grow along two axes of [100] and [101], each with different side-surface planes and longitudinal growth rate.
- In spite of all the deflections and kinks during the growth of nanobelts, single-crystallinity of the whole structure is found to allow for the control of the growth axis and consequently the side-surface planes by pinning the nanoroots along the suitable crystalline plane.

Direct out-of-plane growth of nanobelts on a substrate having an epitaxial relation with TO is also observed, which provides direct control of the growth axis.

8.2 Conclusions

Overall, the studies performed throughout this thesis elaborate on the mechanism behind the crystallization and growth of TO nanocrystallites. A heterogeneous nucleation with limited growth of crystallites due to the strain-limited growth is observed for annealing temperature of up to 500°C. Annealing the nanocrystallites beyond the onset of Arrhenius growth regime, 500°C, provides enough thermal energy to overcome the strain barrier and leads to the further growth of crystallites, while fusion of the grains also helps to the increase in the crystallite size. According to these observations, by keeping the annealing temperature below 500°C, crystallite growth can be effectively inhibited, which is an advantage of this method in comparison with the other sol-gel and solution phase methods mentioned in the introduction. It is also shown that the substrate temperature has a great impact on the formation of nanostructures of TO in the PLD method. Low index planes of TO with lower surface energies are found on the side-surface planes of the deposited nanostructures to minimize the formation and surface energy of the system. By modifying the available thermal energy however, different surface planes with different surface energies will form, as higher energy surface planes are observed for nanowires grown at 600°C compared to nanobelts, which were grown at 500°C. These observations show that the growth temperature is one of the key growth parameters in the synthesis of TO nanostructures.

The catalyst-assisted PLD method is shown to lead to the successful deposition of highly crystalline TO nanostructures including 1D nanowires and nanobelts at relatively low temperatures of 500-600°C. PLD is a high-vacuum (HV) deposition technique and provides a great control on deposition of various materials, including oxides. In contrast, most of the techniques used for depositing 1D nanostructures involve quartz or alumina tubes with poor vacuum in comparison to PLD systems, and deposition often is conducted in atmospheric pressures with the flow of a carrier gas. Due to the high deposition temperatures required in these growth processes, all these techniques involve a tube furnace that can reach temperatures above 1000°C. By using the gold nanoislands with average sizes of 10-50 nm, growth temperature can be decreased to 500-600°C and a local heating in the PLD chamber can also be applied to achieve these temperatures. By enabling the use of HV systems for deposition of 1D nanostructures, the wide range of facilities provided in these systems can be used to manipulate the growth process of these nanostructures. Some of the

possibilities offered by a HV PLD system include the control on the target-to-substrate distance and on the deposition pressure from the 10^{-8} to 1 Torr, the ability to deposit different wetting layers on the appropriate substrates, or to deposit an epitaxial layer prior to the growth of nanostructures, and even the option of growing heterostructures in a single 1D structure. Therefore, in addition to the successful synthesis of 1D and other nanostructures using this catalyst-assisted PLD method, the more important achievement of the present project is the demonstration of the possibility of 1D growth in HV PLD systems. The epitaxial growth study on the Au template with H-Si and on alumina substrate was made possible using the PLD method, and the results show that change in the preferred growth axis of nanobelts is observed due to the change in the surface chemistry of the substrate. In contrast, in thermal and other evaporation methods, the non-reacted surface of Si at high temperature in the low-vacuum tube furnace cannot be maintained. In addition to Si, there are other substrates that will undergo surface reactions and modifications in the high temperature and low vacuum conditions of the tube furnace, and therefore cannot be effectively used for deposition.

Doping TO, and oxide materials in general, is one of the most important approaches to modifying the physical and chemical properties of TO nanostructures. One of the advantages of the laser ablation methods is the ease of conducting doping studies by preparing different doped targets. The laser ablation along with the appropriate deposition conditions keeps the stoichiometry of the target and transfers it to the substrate. On the other hand, solution-based methods offer a potential advantage over these vapor phase deposition techniques, in providing high doping percentages. Eu-doping study of TO nanostructures is a good example of this capability, and in spite of the suppression of the crystallinity of the films, homogeneous Eu doping is achieved for doping levels as high as ~ 8%. These extreme doping studies beyond the solubility limit of TO provide valuable information on the transition from one phase to another, and as observed in the case of Eu-doping in TO, a new phase might also form in the transition region. The new $Eu_2Sn_2O_7$ phase formed in these doping studies shows interesting luminescence and magnetic properties. Given that there is only a limited number of reports on this material in literature, the present work opens a great opportunity to further explore the interesting properties of this material, following up on the results observed in our experiments.

Electrical characterization of TO nanostructures is also another important aspect in the TO nanostructure research since carrier concentration and transport have a great impact not only on the transparent conducting, gas sensing, and catalytic properties, but also on the operation of FET's and

other devices fabricated using TO nanostructures. Although post-annealing in gases with different oxygen compositions can be used to modify the carrier concentration and band bending in the grain boundary of TO nanostructures, the main control of the electronic properties of TO nanostructures can be achieved during the growth process. Electronic transport in nanostructured TO films is a especially complex phenomenon, due to the effects of grain boundaries and the adsorbed gases, and the presence of bulk and surface defects. Most of the reports on the electronic transport of TO nanostructures in the literature have focused on transport properties of these nanostructures at temperatures above the room temperature, because of the interest in their gas sensing properties. The fundamental knowledge on the carrier transport and the conduction channels can however be only obtained by performing temperature dependent studies at low temperatures as well as high temperatures. The results of our study on the electronic transport properties of TO nanocrystallites show that energy barriers with nearly constant heights form at the grain boundaries for all the grain sizes studied from 4 nm up to 12 nm, and the charge depletion layer on the surface of crystallites can also act as an important channel at low temperatures (below 90 K). This information on the conduction channels is obtained by fitting a two-medium model to the resistivity curve, which successfully accounted for the observed change in the slope of the resistivity.

8.3 Suggestions for Future Work

In the synthesis of nanocrystalline TO films using the spin-coating method, we demonstrated the ability to control the crystallite size and conductivity of these nanostructured films and have shown the stability of nanocrystallite sizes upon prolonged annealing. As a next step, the gas-sensing properties of these layers can be measured using a test gas, e.g. CO, to study the differences in the sensitivity of the TO films deposited using this method upon changes in the nanocrystallite size. Indeed, we have already performed preliminary experiments using a home-built gas flow setup, confirming the gas-sensing property of the films however further improvements in the gas exposure system are required, to be able to better control the “gas on” and “gas off” steps and achieve a steady flow in the system. In addition, as shown for the Eu doping study (Chapter 5), the ease of doping these TO films using this method is a great advantage that can be exploited to increase the conductivity of the films. It is of particular interest to investigate the effects of doping on the conductivity of the amorphous TO films, to determine whether the observed conductivity for amorphous Eu-doped film at a high dopant concentration and a low post-anneal temperature could be generalized to other dopants. Overlapping valence band of the cations has been proposed to be the

origin of conductivity in amorphous phases of TCO materials, where the mobility of carriers is expected to be significantly higher.[127] The latter is of great interest for applications of transparent conductors in thin-film transistors.

In the Eu-doping study, the photoluminescence properties of the films are investigated. We observe not only the characteristic 593 nm and 614 nm emissions of Eu^{3+}, but also strong emissions in the visible range in the SnO_2 structure, the latter of which promises new applications in backlighting and displays. The emission properties of these films can be further investigated by cathodoluminescence, in order to study the luminescence properties of the samples upon cathode-ray excitation. The exotic magnetic transitions of the $Eu_2Sn_2O_7$ phase can also be further explored by measuring the magnetization at lower temperatures (down to mK range), where the persistent spin dynamics has been reported to appear for other pyrochlores with similar antiferromagnetic ordering.[122] Performing specific heat, muon spin relaxation, and neutron diffraction measurements can also help to elucidate the nature of the observed magnetic ordering and phase transitions.

The results obtained for growing TO nanostructures by using the catalyst-assisted PLD method have opened up new prospects for growing other nanostructures by fully exploiting the deposition parameters. This technique is not limited to the fabrication of just TO nanostructures, and can indeed be used for synthesizing various nanostructures of different materials and oxides in particular. Based on the results on the Al_2O_3(0001) substrate, growing vertically aligned nanobelts may be possible by establishing an epitaxial relation. However, direct deposition on dissimilar substrate will still cause distortions. For this reason, pre-depositing an epitaxial layer of SnO_2 (or the desired oxide) and preparing the GNI template on this layer might greatly increase the likelihood of obtaining vertically aligned nanobelts or nanowires, depending on the deposition temperature. The other exciting opportunity that emerged from this catalyst-assisted PLD approach is doping the target with the desired carrier donor/acceptor, magnetic or optically active dopants, which can then be used as a means to introduce different properties in these one-dimensional nanostructures. Iron, cobalt, and manganese are among the magnetic dopants that have been reported to result in magnetic orderings in TO films and are suitable candidates for doping in nanobelts for magnetic studies. Another important project is the fabrication of hetero-structures using this method with switching between multiple targets during the deposition. The lattice matching considerations and the possibility of VLS growth of that phase using Au or other catalysts should obviously be considered. Fabrication of p-n junctions in a single nanobelt is one of these exciting possibilities regarding the synthesis of heterostructures.

Radial in addition to longitudinal heterostructures can be deposited using this method. Oxides with intrinsic or p-type doped carriers will be of special interest for the synthesis of p-n junctions in combination with the variety of available n-type oxides. Among the p-type oxide semiconductors, SnO will be especially interesting because of the compositional similarities between the SnO_2 and SnO, where other p-type oxides including Cu_2O or ternary oxides can also be considered. Finally, the effects of different catalysts, including inert silver and platinum for oxides and iron, cobalt, cupper, and nickel for non-oxides, in synthesizing nanostructures and in depositing different oxides can also be studied, which may open additional new opportunities for depositing one-dimensional nanostructures of an even wider range of materials.

Appendix A

The figures shown in Appendix A.1-A.3 are the supporting information for the data presented in Chapter 3: Appendix A.1 shows the effect of prolonged annealing on the size of crystallites, Appendix A.2 shows the survey XPS spectra for different Ar sputtering times, and Appendix A.3 shows the XPS spectra of reference powder samples used for peak position assignment in TO films. The figure shown in Appendix A.4 is also the supporting information for the data presented in Chapter 6, showing the cross-sectional view of the nanobrick TO sample.

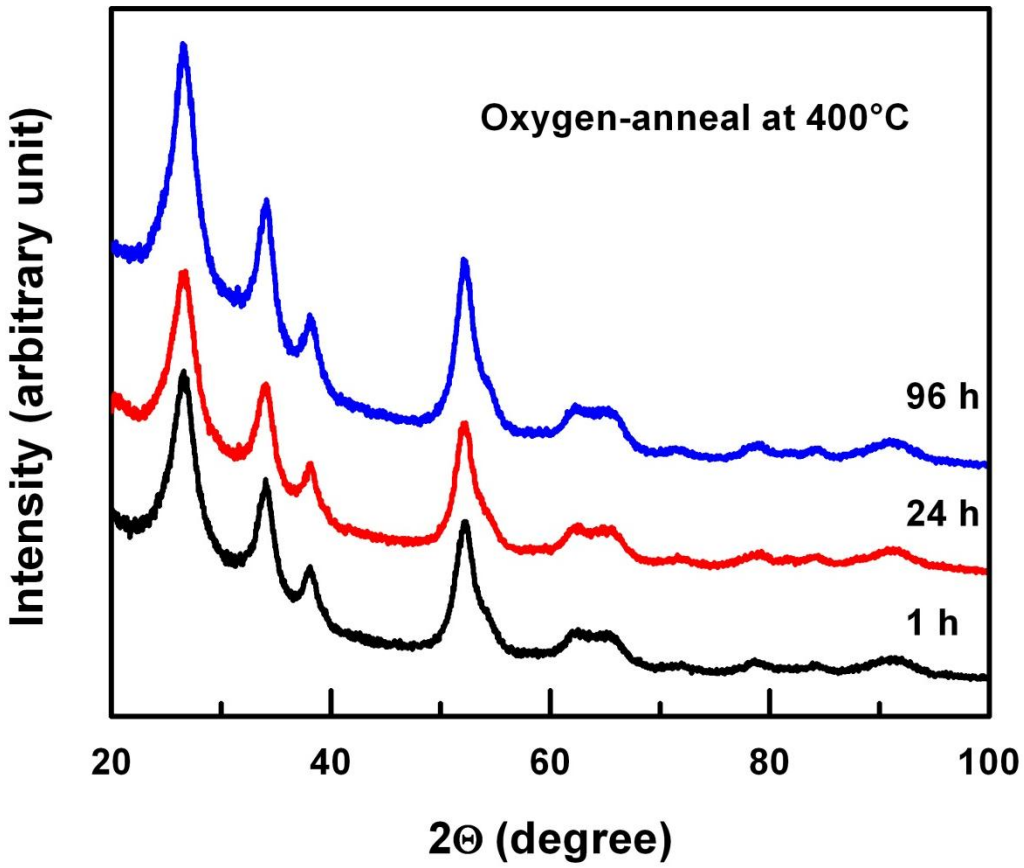

Appendix A.1 Glancing-incidence XRD patterns of a tin oxide film prepared on a glass substrate by post-oxygen-anneal at 400°C successively for 1 h, 24 h, and 96 h

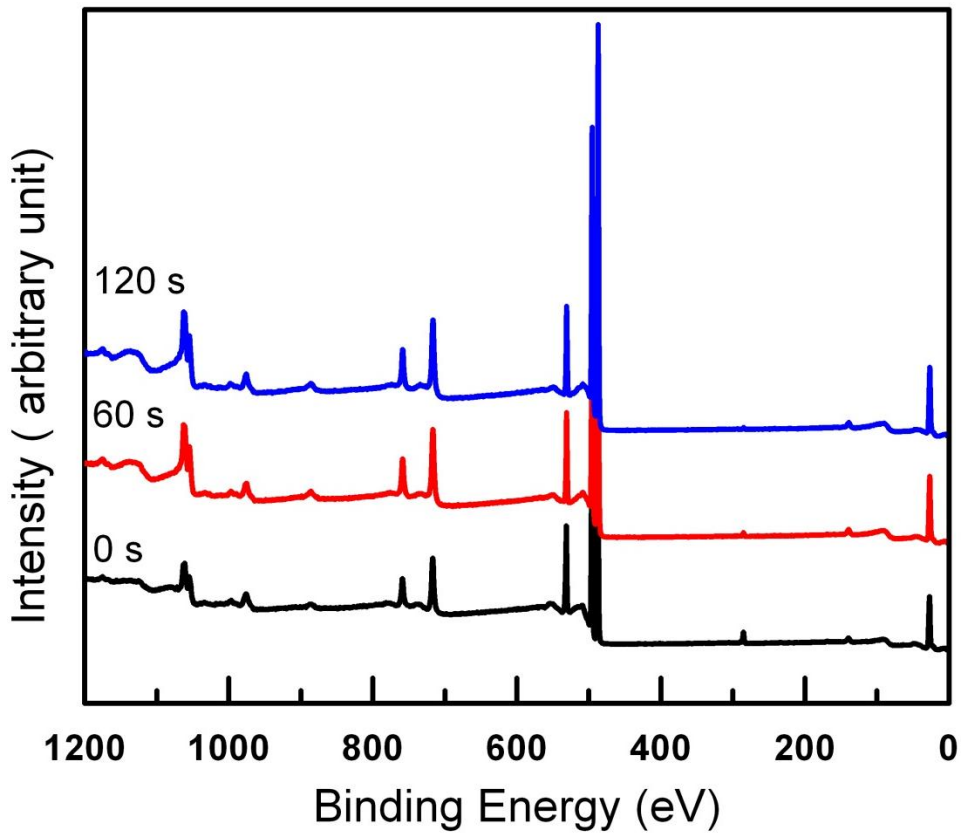

Appendix A.2 XPS survey spectra of tin oxide films prepared on a glass substrate by post-oxygen-anneal at 400°C as a function of sputtering time.

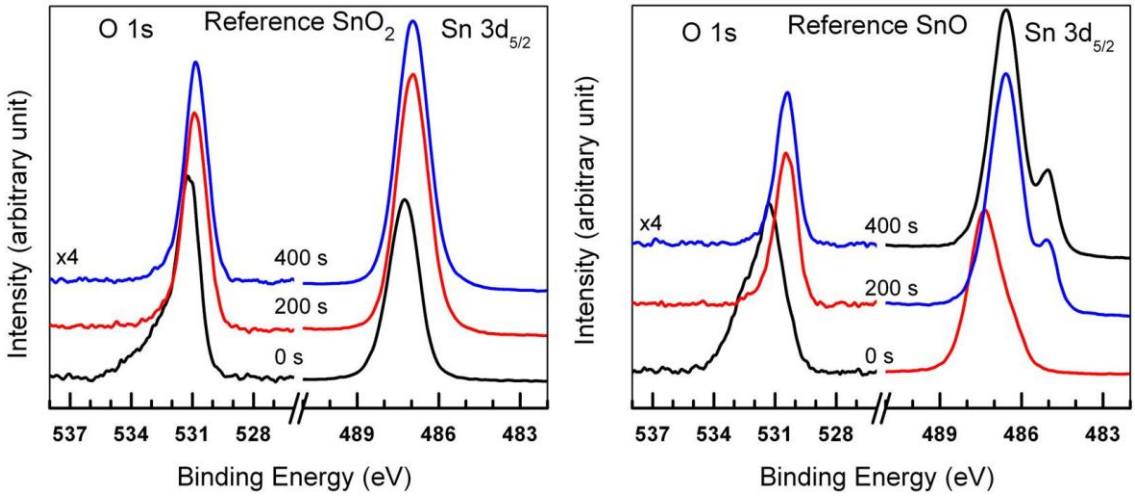

Appendix A.3 Sn $3d_{5/2}$ and O 1s reference spectra of SnO_2 (left) and SnO powders (right) as a function of sputtering time.

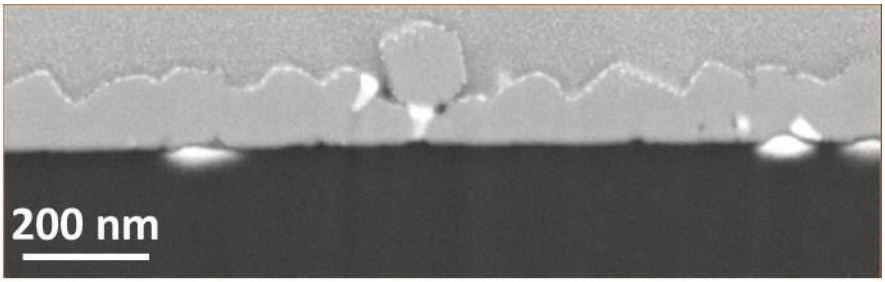

Appendix A.4 The backscattered electron SEM image of the nanobrick sample PLD-grown at 400 mtorr O_2 and 700°C obtained from the cross-section of the sample using a Focused Ion Beam SEM.

Bibliography

[1] Ç. Kılıç and A. Zunger, Physical Review Letters **88**, 095501 (2002).

[2] D.M. Ginsberg, *Physical Properties of High Temperature Superconductors V. I* (World Scientific, Singapore, 1989), p. 516.

[3] T. Minami, Semiconductor Science and Technology **20**, S35-S44 (2005).

[4] A.K. Singh, A. Janotti, M. Scheffler, and C.G. Van de Walle, Physical Review Letters **101**, 1-4 (2008).

[5] R.G. Gordon, MRS Bulletin 52-57 (2000).

[6] L. Wang, M.-H. Yoon, G. Lu, Y. Yang, A. Facchetti, and T.J. Marks, Nature Materials **5**, 893-900 (2006).

[7] M Batzill and U Diebold, Progress in Surface Science **79**, 47-154 (2005).

[8] R. Dolbec and M.A. El Khakani, Applied Physics Letters **90**, 173114 (2007).

[9] S Shukla, S. Patil, S.C. Kuiry, Z. Rahman, T. Du, L. Ludwig, C. Parish, and S. Seal, Sensors and Actuators B: Chemical **96**, 343-353 (2003).

[10] L. Luxmann and R. Dobner, Metall (Berlin) **34**, 821 (1980).

[11] V.T. Agekyan, Physica Status Solidi (a) **43**, 11-42 (1977).

[12] K.B. Sundaram and G.K. Bhagavat, Journal of Physics D: Applied Physics **16**, 69-76 (1983).

[13] B. Stjerna, C.G. Granqvist, A. Seidel, and L. Häggström, Journal of Applied Physics **68**, 6241 (1990).

[14] S. Seal and S. Shukla, JOM- J Min. Met. M. S. **54**, 35-38 (2002).

[15] A. Chowdhuri, V. Gupta, K. Sreenivas, R. Kumar, S. Mozumdar, and P.K. Patanjali, Applied Physics Letters **84**, 1180 (2004).

[16] D F Crabtree, Journal of Physics D: Applied Physics **11**, 1543-1551 (1978).

[17] C. Fitzgerald, M. Venkatesan, L. Dorneles, R. Gunning, P. Stamenov, J. Coey, P. Stampe, R. Kennedy, E. Moreira, and U. Sias, Physical Review B **74**, 1-10 (2006).

[18] T. W. Kim, D. U. Lee, and Y. S. Yoon, Journal of Applied Physics **88**, 3759 (2000).

[19] N.-l. Wu, S.-Y. Wang, and I.A. Rusakova, Science **285**, 1375-1377 (1999).

[20] Z Jin, H.-J. Zhou, Z-.L. Jin, R.F. Savinell, and C.-C. Liu, Sensors and Actuators B: Chemical **52**, 188-194 (1998).

[21] G Sakai, N.S. Baik, N. Miura, and N. Yamazoe, Sensors and Actuators B: Chemical **77**, 116-121 (2001).

[22] Arik Kar and Amitava Patra, Journal of Physical Chemistry C **113**, 4375-4380 (2009).

[23] T. Moon, S.-T. Hwang, D.-R. Jung, D. Son, C. Kim, J. Kim, M. Kang, and B. Park, Journal of Physical Chemistry C **111**, 4164-4167 (2007).

[24] O. Lupan, L. Chow, G. Chai, H. Heinrich, S. Park, and a. Schulte, Physica E: Low-dimensional Systems and Nanostructures **41**, 533-536 (2009).

[25] S. T. Chang, I. C. Leu, and M. H. Hon, Electrochemical and Solid-State Letters **5**, C71 (2002).

[26] Z.R. Dai, Z.W. Pan, and Z.L. Wang, Solid State Communications **118**, 351-354 (2001).

[27] S Shukla, V Venkatachalapathy, and S Seal, The Journal of Physical Chemistry. B **110**, 11210-6 (2006).

[28] Z. R. Dai, J. L. Gole, J. D. Stout, and Z. L. Wang, The Journal of Physical Chemistry B **106**, 1274-1279 (2002).

[29] J.Q. Hu, Y. Bando, Q.L. Liu, and D. Golberg, Advanced Functional Materials **13**, 493-496 (2003).

[30] N. Yamazoe, Sensors and Actuators B: Chemical **5**, 7-19 (1991).

[31] Z. Liu, D. Zhang, S. Han, C. Li, T. Tang, W. Jin, X. Liu, B. Lei, and C. Zhou, Advanced Materials **15**, 1754-1757 (2003).

[32] Yi Cheng, P Xiong, C Steven Yun, G F Strouse, J P Zheng, R S Yang, and Z L Wang, Nano Letters **8**, 4179-84 (2008).

[33] Matt Law, Donald J Sirbuly, Justin C Johnson, Josh Goldberger, Richard J Saykally, and Peidong Yang, Science (New York, N.Y.) **305**, 1269-73 (2004).

[34] S Shukla, S. Patil, S.C. Kuiry, Z. Rahman, T. Du, L. Ludwig, C. Parish, and S. Seal, Sensors and Actuators B: Chemical **96**, 343-353 (2003).

[35] a Ryzhikov, R Vasiliev, M Rumyantseva, L Ryabova, G Dosovitsky, a Gilmutdinov, V Kozlovsky, and a Gaskov, Materials Science and Engineering B **96**, 268-274 (2002).

[36] V Brinzari, Thin Solid Films **391**, 167-175 (2001).

[37] Brinda B. Lakshmi, Peter K. Dorhout, and Charles R. Martin, Chemistry of Materials **9**, 857-862 (1997).

[38] C. Terrier, J.P. Chatelon, J.A. Roger, R. Berjoan, and C. Dubois, Journal of Sol-Gel Science and Technology **10**, 75-81 (1997).

[39] G Guzman, B Dahmani, J Puetz, and M Aegerter, Thin Solid Films **502**, 281-285 (2006).

[40] A N Banerjee, S Kundoo, P Saha, and K K Chattopadhyay, Journal of Sol-Gel Science and Technology **28**, 105-110 (2003).

[41] D. Pradhan and K.T. Leung, Langmuir **24**, 9707-16 (2008).

[42] Sophie Peulon and D. Lincot, Advanced Materials **8**, 166-170 (1996).

[43] S Chang, I Leu, and M Hon, Journal of Alloys and Compounds **403**, 335-340 (2005).

[44] Z.R. Dai, Z.W. Pan, and Z.L. Wang, Advanced Functional Materials **13**, 9-24 (2003).

[45] Zu Rong Dai, Zheng Wei Pan, and Zhong L Wang, Journal of the American Chemical Society **124**, 8673-80 (2002).

[46] J.Q. Hu, Y. Bando, and D. Golberg, Chemical Physics Letters **372**, 758-762 (2003).

[47] Y. Liu, J. Dong, and M. Liu, Advanced Materials **16**, 353-356 (2004).

[48] Chun-Fang Wang, Su-Yuan Xie, Shui-Chao Lin, Xuan Cheng, Xian-Hua Zhang, Rong-Bin Huang, and Lan-Sun Zheng, Chemical Communications (Cambridge, England) 1766-7 (2004).

[49] Hui Huang, O K Tan, Y C Lee, M S Tse, J Guo, and T White, Nanotechnology **17**, 3668-3672 (2006).

[50] Hui Huang, Y C Lee, O K Tan, W Zhou, N Peng, and Q Zhang, Nanotechnology **20**, 115501 (2009).

[51] E. Comini, G. Faglia, G. Sberveglieri, Zhengwei Pan, and Zhong L. Wang, Applied Physics Letters **81**, 1869 (2002).

[52] F Paraguay-Delgado, W Antúnez-Flores, M Miki-Yoshida, A Aguilar-Elguezabal, P Santiago, R Diaz, and J A Ascencio, Nanotechnology **16**, 688-694 (2005).

[53] Lipeng Qin, Jiaqiang Xu, Xiaowen Dong, Qingyi Pan, Zhixuan Cheng, Qun Xiang, and Feng Li, Nanotechnology **19**, 185705 (2008).

[54] Bin Cheng, Joette M Russell, Wensheng Shi, Lei Zhang, and Edward T Samulski, J. Am. Chem. Soc. **126**, 5972-5973 (2004).

[55] A. M. Morales and Charles M Lieber, Science **279**, 208-211 (1998).

[56] X. Duan and C. M. Lieber, Advanced Materials **12**, 298-302 (2000).

[57] R S Wagner and W C Ellis, Applied Physics Letters **4**, 89-90 (1964).

[58] N Yamazoe, Y Kurokawa, and T Seiyama, Sensors And Actuators **4**, 283 - 289 (1983).

[59] N Barsan and U Weimar, Journal of Electroceramics **7**, 143-167 (2001).

[60] Hisahito Ogawa, Masahlro Nishikawa, and Atsushi Abe, Journal of Applied Physics **53**, 4448-4455 (1982).

[61] T.J. Marks, J.G.C. Veinot, J. Cui, H. Yan, A. Wang, N.L. Edleman, J. Ni, Q. Huang, P. Lee, and N.R. Armstrong, Synthetic Metals **127**, 29-35 (2002).

[62] Henk J. Bolink, Eugenio Coronado, Diego Repetto, and Michele Sessolo, Applied Physics Letters **91**, 223501 (2007).

[63] N. Barsan and U. Weimar, Journal of Electroceramics **7**, 143-167 (2001).

[64] S. Zhang, S.-H. Wei, and Alex Zunger, Physical Review B **63**, 1-7 (2001).

[65] Aleksandra B Djurisić and Yu Hang Leung, Small (Weinheim an Der Bergstrasse, Germany) **2**, 944-61 (2006).

[66] R.N. Bhargava, D. Gallagher, X. Hong, and A. Nurmikko, Physical Review Letters **72**, 416-419 (1994).

[67] M. Nogami, E. Takehiro, and H. Tomokatsu, Journal of Luminescence **97**, 147-152 (2002).

[68] G. Blasse, A. Bril, and W.C. Nieuwpoort, Journal of Physics and Chemistry of Solids **27**, 1587-1592 (1966).

[69] S Dabboussi, H Elhouichet, H Ajlani, A Moadhen, M. Oueslati, and J.A. Roger, Journal of Luminescence **121**, 507-516 (2006).

[70] Tomokatsu Hayakawa and Masayuki Nogami, Science and Technology of Advanced Materials **6**, 66-70 (2005).

[71] S Chang and M Jo, Ceramics International **33**, 511-514 (2007).

[72] I Weber, A. Valentini, L.F.D. Probst, E. Longo, and E.R. Leite, Materials Letters **62**, 1677-1680 (2008).

[73] Xiaoyan Fu, Hongwu Zhang, Shuyun Niu, and Qin Xin, Journal of Solid State Chemistry **178**, 603-607 (2005).

[74] Z.L. Wang, Annual Review of Physical Chemistry **55**, 159-96 (2004).

[75] L.C. Tien, S.J. Pearton, D.P. Norton, and F. Ren, Applied Physics A **91**, 29-32 (2008).

[76] C Czekalla, J Guinard, C Hanisch, B Q Cao, E M Kaidashev, N Boukos, a Travlos, J Renard, B Gayral, D Le Si Dang, M Lorenz, and M Grundmann, Nanotechnology **19**, 115202 (2008).

[77] M Lorenz, E M Kaidashev, A Rahm, Th Nobis, J Lenzner, G Wagner, D Spemann, H Hochmuth, and M Grundmann, Applied Physics Letters **86**, 143113 (2005).

[78] C.M Lieber and Z.L. Wang, MRS Bulletin **32**, 99-108 (2007).

[79] W. Kern, *Handbook of Semiconductor Wafer Cleaning Technology* (William Andrew Publishing/Noyes, 1993).

[80] Youngku Sohn, Debabrata Pradhan, Abdullah Radi, and K T Leung, Langmuir **25**, 9557-63 (2009).

[81] Carl Zeiss SMT Inc., *Instruction Manual: Orion Plus Helium Ion Microscope* (2009).

[82] I. D.-cernatescu, *PANalytical Presentation on XRD Techniques and Instrumentation for Nano-materials Characterization* (2006).

[83] M Kimura, The Rigaku Journal **16**, 25-31 (1999).

[84] J.F. Moulder, W.F. Stickle, P.E. Sobol, and K.D. Bomben, *Handbook of X-ray Photoelectron Spectroscopy* (Perkin-Elmer Corporation Physical Electronics Division, Eden Prairie, 1992).

[85] V Kissine, V. V. Sysoev, and Voroshilov S. A., Sensors and Actuators B: Chemical **79**, 163-170 (2001).

[86] X Q Pan and L Fu, Journal of Electroceramics **7**, 35-46 (2001).

[87] N. Sankara Subramanian, B. Santhi, S. Sundareswaran, and K. Venkatakrishnan, Synthesis and Reactivity in Inorganic, Metal-Organic, and Nano-Metal Chemistry **36**, 131-135 (2006).

[88] Z.W. Chen, J.K.L. Lai, C.H. Shek, and H.D. Chen, Applied Physics A **81**, 1073-1076 (2005).

[89] J Szuber, G Czempik, R Larciprete, D Koziej, and B Adamowicz, Thin Solid Films **391pp**, 198-203 (2001).

[90] J.-M. Themlin, M. Chatin, L. Henrard, P. Lambin, J. Darville, and J.-M. Gilles, Physical Review B **46**, 2460-2466 (1992).

[91] M. Batzill, J. Kim, D.E. Beck, and B.E. Koel, Physical Review B **69**, 1-11 (2004).

[92] V.M. Jimenez, J.A. Mejias, J.P. Espinos, and A.R. Gonzalez-Elipe, Surface Science **366**, 545-555 (1996).

[93] D.F. Cox, T.B. Fryberger, and S. Semancik, Physical Review B **38**, 2072-2082 (1988).

[94] J.-M. Themlin, J.-M. Gilles, and R.L. Johnson, Journal De Physique IV **4**, 183-186 (1994).

[95] M Kwoka, L Ottaviano, M Passacantando, S Santucci, and J Szuber, Applied Srface Science **252**, 7730-7733 (2006).

[96] A. Dieguez, A Romano-Rodriguez, A. Vila, and J.R. Morante, Journal of Applied Physics **90**, 1550-1557 (2001).

[97] Samad Bazargan, Nina F. Heinig, Debabrata Pradhan, and K. T. Leung, Crystal Growth & Design **11**, 247-255 (2011).

[98] Feng Gu, Shufen Wang, Meng Kai Lu, Xiu Feng Cheng, Su Wen Liu, Guang Jun Zhou, Dong Xu, and Duo Rong Yuan, Journal of Crystal Growth **262**, 182-185 (2004).

[99] E.R. Leite, M.I.B. Bernardi, E. Longo, J.A. Varela, and C.A. Paskocimas, Thin Solid Films **449**, 67-72 (2004).

[100] K Ellmer, Journal of Physics D: Applied Physics **34**, 3097-3108 (2001).

[101] Z. Q. Li, Y. L. Yin, X. D. Liu, L. Y. Li, H. Liu, and Q. G. Song, Journal of Applied Physics **106**, 083701 (2009).

[102] T. S. Moss, *Optical Properties of Semi-conductors*, 2nd ed. (Butterworths, London, 1960).

[103] E Shanthi, A Banerjee, V Dutta, and K Chopra, Thin Solid Films **71**, 237-244 (1980).

[104] K L Chopra, S Major, and D K Pandya, Thin Solid Films **102**, 1-46 (1983).

[105] Dong Yu, Congjun Wang, Brian Wehrenberg, and Philippe Guyot-Sionnest, Physical Review Letters **92**, 1-4 (2004).

[106] Alexandre J. C. Lanfredi, Renan R. Geraldes, Olivia M. Berengue, Edson R. Leite, and Adenilson J. Chiquito, Journal of Applied Physics **105**, 023708 (2009).

[107] Y.J. Ma, F. Zhou, L. Lu, and Z. Zhang, Solid State Communications **130**, 313-316 (2004).

[108] R Rosenbaum, Physical Review. B **44**, 3599-3603 (1991).

[109] Heng Liu, Alexandre Pourret, and Philippe Guyot-sionnest, ACS Nano **4**, 5211-5216 (2010).

[110] B.I. Shklovskii and A.L. Efros, Springer Series in Solid-State Sciences **45**, (1984).

[111] A Ivashchenko, I Kerner, G Kiosse, and I Maronchuk, Thin Solid Films **303**, 292-294 (1997).

[112] J. E. Dominguez, L. Fu, and X. Q. Pan, Applied Physics Letters **81**, 5168-5170 (2002).

[113] J.W. Orton and M.J. Powell, Reports on Progress in Physics **43**, 1263-1307 (1980).

[114] K. Subba Ramaiah and V. Sundara Raja, Applied Surface Science **253**, 1451-1458 (2006).

[115] J.M. Lawrence, P.S. Riseborough, and R.D. Parks, Reports on Progress in Physics **44**, (1981).

[116] C. Laubschat, B. Perscheid, and W.D. Schneider, Physical Review B **28**, 4342-4348 (1983).

[117] W.D. Schneider, C. Laubschat, I. Nowik, and G. Kaindl, Physical Review B **24**, 5422-5425 (1981).

[118] M. Dejneka, E. Snitzer, and R.E. Riman, Journal of Luminescence **65**, 227-245 (1995).

[119] D. Lahiri, R.S. Ningthoujam, D. Bhattacharyya, and S.M. Sharma, Journal of Applied Physics **107**, 054316 (2010).

[120] S. Bazargan, N.F. Heinig, F. Rios, and K.T. Leung, (n.d.).

[121] J. Chen, J. Wang, F. Zhang, D. Yan, G. Zhang, R. Zhuo, and P. Yan, Journal of Physics D: Applied Physics **41**, 105306 (2008).

[122] J.S. Gardner, M.J.P. Gingras, and J.E. Greedan, Review of Modern Physics **82**, 53-107 (2010).

[123] S. Bazargan and K.T. Leung, In-Press (n.d.).

[124] John J Boland, Physical Review Letters **67**, 1539-1542 (1991).

[125] S Semancik and R Cavicchi, Thin Solid Films **206**, 81-87 (1991).

[126] Z W Pan, Z R Dai, and Z L Wang, Science (New York, N.Y.) **291**, 1947-9 (2001).

[127] H. Hosono, M. Yasukawa, and H. Kawazoe, Journal of Non-Crystalline Solids **203**, 334-344 (1996).